Analysis and modeling of long-term shoreline changes and alongshore sediment characteristics on the Nile Delta Coast
(ナイル川河口周辺部における長期汀線変化および砂粒子特性の分析)

Mostafa Tawfik Taha Ahmed
モスタファ タウィフィク タハ アメッド

Analysis and modeling of long-term shoreline changes and alongshore sediment characteristics on the Nile Delta Coast
(ナイル川河口周辺部における長期汀線変化および砂粒子特性の分析)

by

Mostafa Tawfik Taha Ahmed
モスタファ タウィフィク タハ アメッド
M.Sc. (Cairo University)
B.Sc. (Cairo University)

A dissertation submitted to the Department of Civil Engineering
in partial fulfillment of the requirements for the degree of

Doctor of Philosophy in Civil Engineering

at the

The University of Tokyo

September 2012

Examination Committee

Assoc. Prof.	**Yoshimitsu Tajima (Supervisor)**
Prof.	**Shinji Sato**
Assoc. Prof.	**Suzuki Takayuki**
Assoc. Prof.	**Takeyoshi Chibana**
Assoc. Prof.	**Haijiang Liu**

Abstract

Coastal morphology changes are commonly experienced phenomena. While several coastal countermeasures are applied along the coasts to control the morphological changes, the interference of these human activities upon the coasts might make it hard to achieve its perceived goals. In order to prepare an overall and sustainable strategy for the coastal management, reliable long-term shoreline change data and forecasting of the future changes are required. Investigations of historical coastal changes are essential to understand the physical mechanisms of the changes and to predict the future shoreline evolutions. It is thus crucial and worthwhile to quantitatively estimate the areas of erosion and accretion, sediment sources, sediment transport rates, and sediment characteristics along the coast.

The general aim of this research is to study the long-term shoreline changes through the analysis of shoreline locations, investigations of sand materials, and application of numerical models. As a case study site, this research focuses on the Nile Delta, which is suffering from large scale and long term coastal erosion. The study site has 250 km stretch of the coast line from Iduku lake in the west end to Port-Said in the east and faces to the Egyptian Mediterranean Sea. To fully capture the physical characteristics of the coastal dynamics, this study applied multiple different methodologies: analysis of the land-sat images, investigations of sampled sand grains around the swash zone, and the numerical analysis based on the shoreline model.

First, the past coastal line changes were quantitatively monitored around the study site. The coastal lines were automatically extracted based on the local XY-coordinates from Land-sat satellite images over 37 years from 1973 to 2010 with unequal time intervals. The extracted coastal lines were quantitatively investigated based on the linear regression technique as well as the empirical orthogonal function analysis.

Second, a field survey was conducted in February 2011. Sand samples were collected at more than 60 various locations along the shoreline. Samples were collected from the layer at 5-10 cm under the ground surface in the inter-tidal zone. These samples were used for the thermo-luminescence (TL) test. This study measured TL intensity of the feldspar extracted from the sand samples. Consistency between the results of this

method with the interpretations based on the analysis of land-sat images was achieved. Using the same samples, sand characteristics were further investigated. The grain size distribution; the median sand size, D_{50} was measured using the laser diffraction particle size distribution measuring apparatus. The color of sand grains was also identified by naked eyes and the mineral composition based on color was interpreted using the automated analysis of images captured by a digital microscope.

Last, shoreline change model was applied to reasonably explain physical procedures of the observed shoreline changes, accounting for sediment size distributions. The calibrated model is then used for predictions of the future shoreline changes accounting for different climate scenarios. The present model accounted for the quantitative characteristics of coastal structures and river mouth. The improved numerical model simulates the wave transformation, regional sediment transport, sediment size, and shoreline changes. The model composed of two parts, Energy Balance Equation model and One-line model. Due to the high curvature of the shoreline along the study site, the One-line model was formulated in terms of local coordinates normal to and tangential to the actual shoreline. Alongshore distributions of the sediment grain sizes were also computed and compared with the observed results.

The analysis of the Land-sat images showed that approximately 46% of the Nile Delta Coast (NDC) experienced erosion while 52% undergo some accretion. The general features along the NDC are erosional at the three headlands of Rosetta, Burullus and Damietta, and the accretion for the embayment, near the structures, and the sand spit (Eastward Damietta).

As a result of the TL test, it was found that the sand grains near the Rosetta and Damietta branches present a higher TL signal and TL intensity gradually decreases with increasing distance from the two river mouths, which indicates sediment alongshore transport features. The small difference of TL intensities between the sand grains near the river mouth and the ones on the natural coast indicates that the sediment supply from the river is limited. The estimated sediment transport directions based on the TL analysis are consistent with the interpretations based on the analysis of land-sat images around Rosetta promontory while these two estimations were

contrary to each other on the west side of Damietta promontory. Observed inconsistency may be due to fluctuating errors of TL measurements.

Through the analysis of sand characteristics, clear difference was noticed by the naked eyes in the sand color, and size between different areas. Around Rosetta promontory the sand color is light and average size is 0.28 mm, while in the middle part of the Delta the color is lighter and grain sizes are coarser with average size of 0.6mm, and from Damietta to Port Said the color is darker and average grain size is 0.23mm. The sediment comes from the river contains blackish sand with small size and other colors with bigger size. The dark sand is dominant in the sand dunes. The sand samples near the large traps i.e., Idku jetty, El Burullus jetty, and Damietta breakwater are characterized by dark color. This illuminates that the dark grains is smaller than other grains which moves easily and accumulated near the coastal structure.

The improved model was calibrated and validated against the data from Land-Sat images along the NDC in Egypt. The model successfully simulates the general features along the NDC. The model exhibits its ability in the prediction of the shoreline around Rosetta promontory before and after placing the countermeasure structures. The correlation between the numerical model simulation and the Land-Sat image data was more than 90%. The model was used to check the importance of placing the current coastal structures around Rosetta mouth by simulating the shoreline changes with and without structures. Severe erosion was estimated in the case if there are no structures around the Rosetta mouth. By comparing the grain size distribution around Rosetta mouth in 1988 with the size in 2012, it is noted that the grain size become coarser due to the erosion. The model succeeded to qualitatively simulate such change of the grain size around the Rosetta mouth.

Author's Declaration

I hereby declare that I am the sole author of this thesis. All materials are obtained and presented in accordance with academic rules and code of conduct of the University of Tokyo. I have fully cited and referenced all material and results that are not originally mine.

I authorize the University of Tokyo to lend this thesis to other institutions or individuals for the purpose of scholarly research.

I further authorize the University of Tokyo to reproduce this thesis by photocopying or by other means, in total or in part, at the request of other institutions or individuals for the purpose of scholarly research.

Signature
Mostafa Tawfik Taha Ahmed

Acknowledgements

All prays are due to Allah who supports me in every simple aspect in my life. This research would not have been possible without the support of many people. My supervisor is a key person among those people. I would like to express my deepest thanks to my advisor, Assoc. Professor **Yoshimtsu Tajima**, for his constant encouragement and invaluable and technical guidance, kind support, careful review, suggestions, beneficial comments, and professional touch, during my doctoral course.

Sincere thanks are due to this dissertation committee; Assoc. Prof. **Yoshimtsu Tajima**, Prof. **Shinji Sato**, Assoc. Prof. **Suzuki Takayuki**, Assoc. Prof. **Takeyoshi, Chibana**, and Assoc. Prof. **Haijiang Liu**. The careful review; suggestions; constructive comments; and professional on this work are highly appreciated.

I would like to express my deepest gratitude to my parents, and my wife for their permanent inspiration and encouragement in my life. I would like also to express my gratitude to all my friends in Egypt and Japan who supported me to complete this work.

Last but not the least; I would like to thank all my colleagues in the coastal engineering lab - Tokyo University for providing me a good environment to complete my research. Also, I would like to express my sincere gratitude to the Irrigation and Hydraulics Department - Cairo University for giving me a study leave to proceed in my doctoral study in Japan. Sincere gratitude goes to MEXT for the financial support of my study.

Contents

List of Figures

List of Tables

List of Notations

$y(x,t)$	The original time series of the shoreline
y_k	The k-th combined eignfunction pair (spatial and temporal)
n	The number of modes, the lesser number of the temporal (n_t) or spatial (n_x) samples
$e_k(x)$	The spatial eigenfunction
$c_k(t)$	The temporal eigenfunction
$a_k(t)$	The eigen value
$N(f,\theta,x,y,t)$	Directional spectrum
$N(f)$	Frequency spectrum
$G(f,\theta)$	Directional spreading function
E	Wave energy
E_r	Recovery wave energy
f *or* σ	Wave frequency
f_p	Peak frequency
θ	Angle of wave approach
x, y	Horizontal coordinates
m, n	Coordinates normal and parallel to shoreline
dx, dy	Horizontal grid size
dm, dn	Normal and parallel the shoreline grid size
t	Time
dt	Time increment
N_{in}	Source term representing wind energy input
N_{nl}	Source term representing input energy from non-linear interaction between different wave frequencies
N_{ds}	Source term representing energy loss in dissipation.
C	Phase velocity
C_g	Group celerity
k	Empirical coefficient in Mase's model.
k	Wave number
c_x, c_y, c_θ	Propagation velocities in the energy balance equation
ε_b	Wave energy dissipation term in Tajima & Madsen's (2006) model.
H_{rms}	Root-mean-square wave height
$H_s, H_{1/3}$	Significant wave height
$H_{s,12}$	Maximum wave height of non breaking waves that occur more than 12 hours per year (0.137 %)
H_{brms}	Root mean square breaker height
H_b	Breaking wave height
T	Wave period
δ	Standard deviation of the annual wave height.

β	Bed slope
h	Water depth
L_o	Deep water wave length
Q	Longshore sediment transport rate
D_c	Depth of closure
D_B	Average berm elevation
q	Source or sink of sand
K_1, K_2	Empirical coefficients in sediment transport equation
α_0	Deep water wave approach angle
α_b	Wave breaking angle
α_{b_s}	Effective wave breaking angle
D_{50}	Mean diameter of sand grain size
g	Acceleration of gravity
w_s	Fall velocity
p	Porosity of sand on the bed
m_b	Beach slope near the breaking point
$\overline{V}$	Mean alongshore current velocity over the surf zone
V_{ex}	External surf-zone average alongshore current velocity generated by tide or/and wind
ε	Transport coefficient
A	Shape parameter
x	Breaker index
ζ	Surf similarity
C_f	Bottom friction coefficient
B	The mixing width
ΔD_s	The exchange depth
μ	Percentage of each grain size at the current time step
μ_B	Initial percentage of each grain size
b	Indicate the breaking

Chapter1 Introduction

1.1 Background of research

The coastal zone has a great importance in human life. Studies have shown that the bulk of humanity is concentrated along or near coasts on just 10% of the earth's land surface. As of 1998, over half the population of the planet Earth (about 3.2 billion people) lives and works in a coastal strip with width of just 200 kilometers (Hinrichsen, 1999). Figure 1.1 presents the location of permanent lights on the Earth (NASA) which indicates that great portion of people living near the coastal areas. This is a typical case of Egypt. Over 90% of the Egyptian lives on 6% of the total area of Egypt, in particular along the narrow valley on the Nile banks and in the Nile Delta as shown in Figure 1.1. The Delta is facing the Mediterranean Sea and the entire stretch of the coast line exceeds 300 km from Alexandria in the west end to Port Said in the east. The Nile Delta is densely populated (200 to 400 Inh/km^2), and has full of industry, agriculture and tourism activities. The Protection of the Delta has significant and critical impact on the Egyptian economy. Unfortunately the Nile delta is characterized by low-lying coastal areas at different locations. These areas are protected by different features including manmade structures, elevated coastal sand dunes, and narrow sandy strip belt varying from 1 km to 10 km wide. Figure 1.2 presents the elevation level of the Nile Delta Coast.

Figure 1.1. Map of the location of permanent lights on Earth's. (NASA).

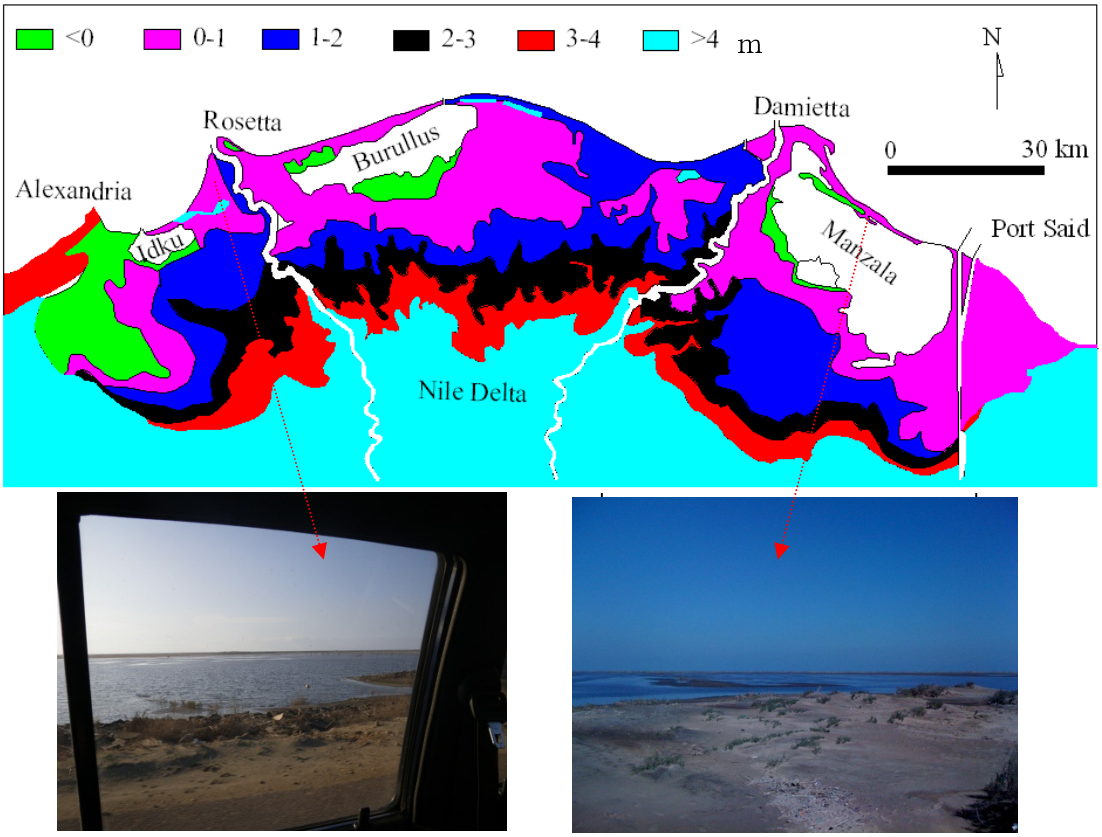

Figure 1.2.The main topographic features of the Nile Delta Coast below and above mean sea level (Frihy, 2003). Two different images were taken after strong waves in February 2012 showing that the water behind the shoreline.

While this sandy belt is protecting the low land from flooding, it has experienced erosion at different locations. Thus the Nile delta is vulnerable to strong waves and sea level rise. Erosion problem is of great importance in coastal zone management of the Nile Delta Coast. The last statement is manifested by that Erosion affects the populations, transportation routes, investments, communities, ecosystems, and lower land areas. The accretion is also a problem in some location since accretion causes blocking of the waterways, such as El-Burullus inlet.

The Nile Delta coast is highly dynamic and subjected to severe morphological changes especially around the two branches of the River Nile; Rosetta and Damietta. Figure 1.3, shows the historical shoreline changes around the two branches of the Nile River. The main known reasons for the erosion around the Nile promontories are generally the cessation of sediments supply from the Nile river due to: (i)construction of dams (Aswan reservoir, Aswan high dam,1964) about 1100 km south from the river mouth; (ii) constructions of barrages (seven main

barrages) across the Nile path and (iii) natural reduction of Nile floods due to climatic changes. The White Nile, the Blue Nile and Atbara River are the major tributaries of water to the main channel of the River Nile as shown in Figure 1.4. In the past floods used to occur from August to October before the construction of the Aswan High Dam. While 84 % of the water comes from Ethiopian plateau, the rest water comes from central and east African lake plateau.

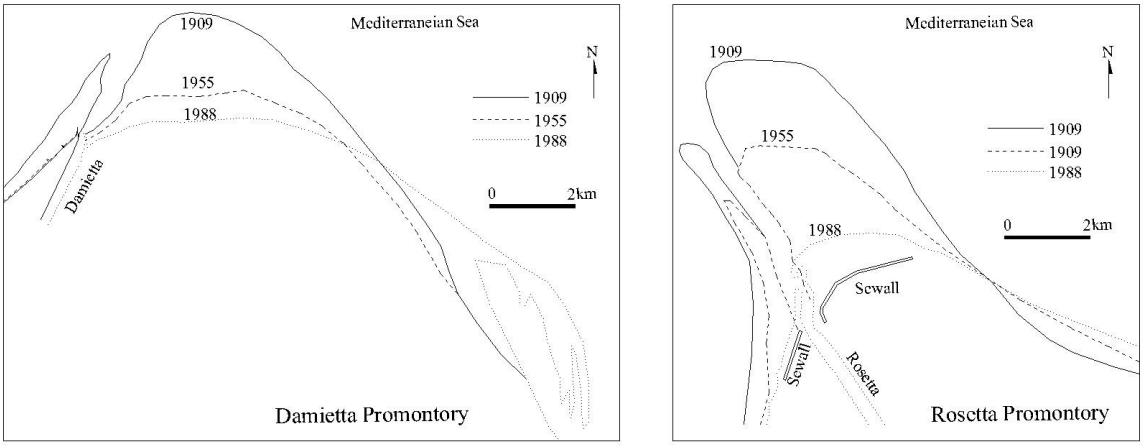

Figure 1.3. Historical shoreline changes around Rosetta, and Damietta river mouths (modified after , Fanos 1995).

Figure 1.5, presents the water discharge upstream and release from Aswan High Dam as well as the water discharge from Rosetta and Damietta branches and the corresponding suspended sediment load. The construction of the Dam and the barrages control the water flood and affect the sediment discharge to the coast. The locations of the Dam and the irrigation barrages constructed along the River route are demonstrated in Figure 1.6.

Several coastal countermeasures, i.e. seawalls, groins, dikes, jetties, and breakwaters were placed along the coast to decrease the erosion, and accretion and sustain the coast in a stable state. The shore protection Agency has invested $10,000,000 / year in past 10 years. However, many of the structural measures, especially protective solid structure are subject to direct impact from the coastal erosion (CORI, 2010). The interference of those structures upon the coasts might shift the problem to adjacent areas which can cause failure of the management of the entire coast. The long term stability and sustainability of those structures has a great concern.

In order to prepare an overall sustainable strategy for the coastal management of the Nile Delta Coast and to develop an efficient countermeasure, it is essential to have reliable shoreline

changes data, to understand factors and causes of shoreline changes and to have an ability to predict the future morphology changes around the Nile river delta.

Figure 1.4. River Nile and its main tributes.

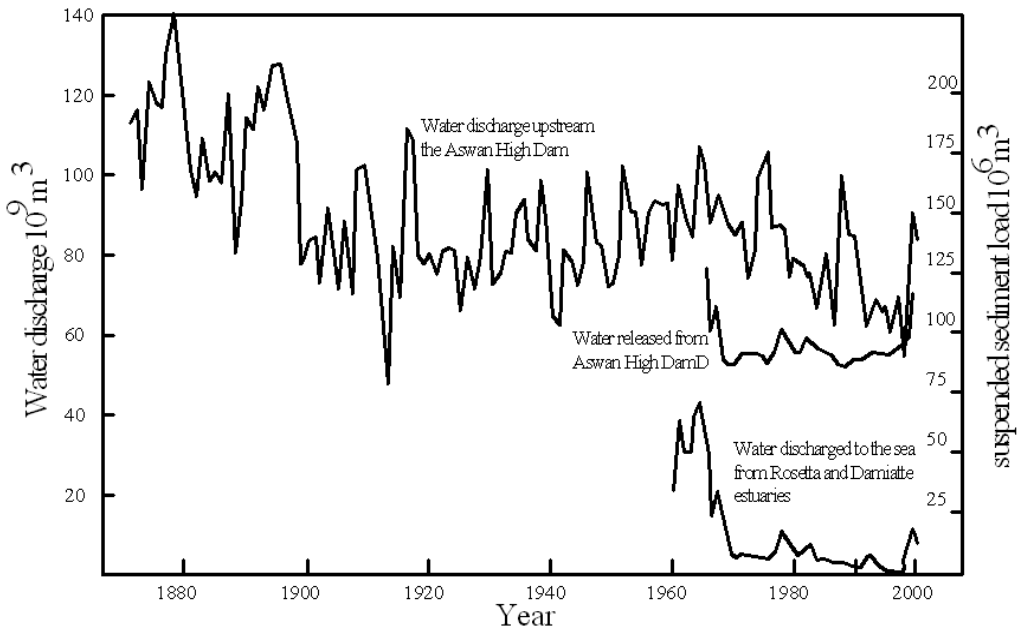

Figure 1.5. Long-term variations in water discharge recorded upstream of the High Aswan Dam and their corresponding suspended sediment load between 1871 and 2000(Frihy and Lawrence, 2004).

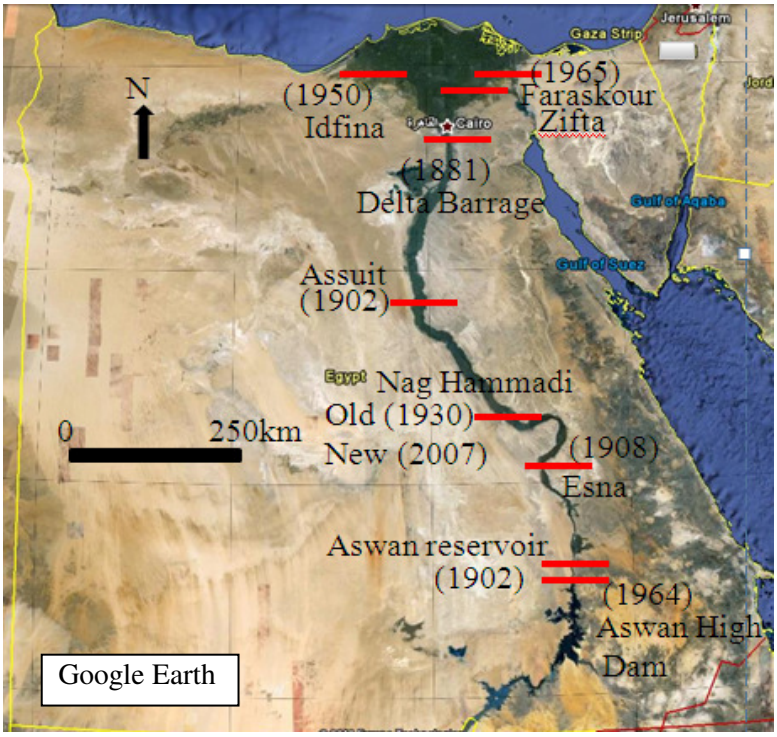

Figure 1.6. The locations and the construction dates of the irrigation structures constructed along the Nile River.

This calls for long-term monitoring of the shoreline changes along the entire Delta Coast. The continuous monitoring of the shoreline movement is essential to understand the large-scale long shore sediment budget, which significantly affects on the long-term morphological changes. These morphological changes have significant impacts on the coastal management and risk assessment. Thus the physical characteristics of such morphology changes must be fully understood, particularly over long timescales along the entire coast line of the Nile Delta. This understanding should cover the past, present and prediction of the future. Identifying the areas subjected to short and long-term changes, and understanding the causes of these changes are important. Assess the long-term changes deemed more important than focusing on the short-term fluctuations. In other word, the long-term behavior plays a significant role in the prediction of the future compared to that of short-term behavior.

1.2 Scope of the study

The present research attempts to investigate an overall and sustainable strategy for the coastal management through studying the time variation of the shoreline changes, sediment drift rates, and grain size distribution along the Nile Delta Coast. The scope of the research is summarized in the following points.

1- Evaluate the past coastal morphology changes along the Nile Delta and their possible causes.
2- Estimate the areas of erosion and accretion along the coast.
3- Determine the sediment characteristics and sediment transport rates.
4- Check the efficiency of the current countermeasures located along the coast and proposes alternative countermeasures to stabilize the morphological changes.
5- Predict the shoreline changes and sediment distribution along the study site in the future.

1.3 Methodology

In order to accomplish the objectives mentioned in the above section, this study developed a predictive tool, which integrates different techniques for better understanding of the shoreline changes and the effects of the coastal structures located along the NDC.

This study consists of following three sections.

1- Analysis of shoreline changes using Land-Sat images.

The past coastal line changes were quantitatively monitored around the study site. The coastal lines were automatically extracted based on the local XY-coordinates from Land-sat satellite images over 37 years from 1973 to 2010 with unequal time intervals.

2- Analysis of the sediment characteristics and sediment transport using sand samples extracted along the Nile Delta Coast.

Field sand samples were collected at 60 various locations along the study site and sediment characteristics (Color, size, and composition) of these sand samples were investigated. Finally, Thermo-luminescence of these sampled sands were measured and compared.

3- Numerical analysis

Improved numerical model simulates the wave transformation, regional sediment transport, sediment grain size, and coastal shoreline changes. The model composed of two associated parts, Energy Balance Equation model, and One-line model. The improved model was calibrated and validated against the results acquired from the analysis of Land-sat images along the Nile Delta Coast in Egypt.

The land-sat images were used to determine the shoreline changes and to estimate the eroded and accreted areas, which eventually determine alongshore sediment transport rates and directions. Sand samples were used to investigate the sediment characteristics along the coast. The Thermo-luminescence test was performed on the same samples. This test was conducted for two purposes: the first is to verify the application of this test through the comparison of its results with the results from the Land-sat; since the TL characteristics of the sediment sources is different from those of the sediment along the coast; the second aim is to define the sediment sources along the coast. Based on all the collected data and information, finally, a numerical model was introduced, calibrated, and applied to the prediction of the future changes. The results and the recognized information from the different approaches show an integration and compatibility with each others.

1.4 Thesis structure

In Chapter 2, the study site information and the employed data were summarized. The waves, tide data, sea level rise were recognized. The features along the Nile Delta Coast, the geomorphologic structure, and land subsidence were presented. The locations and details of the coastal countermeasures (around Idku lake, Idku marine, Rosetta mouth, El Burullus inlet, Baltim resort, Damietta port, Ras El Bar resort, Damietta mouth, El Gamil inlet 1&2,and Port Said) were also illustrated at the end of this chapter.

Chapter 3 " Analysis of Land-sat images" starts by a literature review of the remote sensing technique and its advantages followed by a review of the previous studies which used the satellite images for detecting the coastal changes of the Nile delta coast. Also description of the methodology of shoreline extraction (Data collection, and Image processing) from the Land-sat images and statistical analysis of the extracted shoreline were discussed. Further investigation of the shoreline data set based on the Empirical Orthogonal Function was performed. At the end of this Chapter, detailed analysis of the results of the shoreline changes, erosion and accretion areas and sediment transport directions around both Rosetta and Damietta promontory were summrized.

Chapter 4 starts with a review of the sediment transport detection methods and review of the Thermoluminscience technique. Advantages and disadvantages of using this method were discussed. The idea of using this method was reviewed. The locations of the sand samples were marked along the Nile Delta Coast. The method and precautions of taking samples from the site were presented then the pretreatment sequence was illustrated. Details of the protocol and sequence of the test were discussed. The method of measuring the grain size distribution, and the procedure of taking the images under the microscope were shown as well as the method of classifying and analyzing the images. In closing of Chapter 4, the results of the TL test, grain size distribution, and the sediment transport analysis were discussed and comparison were made between the evidence concluded from this method with the Land-sat image analysis.

Chapter 5 reviewed the relevant previous studies on numerical models for wave transformation particularly those based on phase average model. The objective of the present wave model was illustrated. The governing equations and boundary condition for the Energy Balance equation

and the breaking model were described. The procedure of how the breaking term is included in the model were investigated .The results of different wave condition scenarios were shown, and the breaking wave data used in the shoreline change model were presented .

Chapter 6 starts with comprehensive literature review of shoreline change models. The boundary conditions followed by the objectives of the One-Line model, the details of its governing equation, and boundary conditions. The adaption of the sediment size in the one line model was discussed and the results were presented. In closing of Chapter 6, sensitivity analysis of various calibration parameters (wave direction, and wave height) is examined.

In Chapter 7, a summary of the present study is exhibited. Research conclusions were demonstrated along with recommendations for future research.

Chapter2 Study site and employed data (Nile Delta Coast)

2.1 General Features of the Nile Delta Coast

The Egyptian Mediterranean coastal zone suffers high rate of population growth, land subsidence in the Delta region, excessive erosion rates, saltwater intrusion, soil salinization, land use interference, ecosystem pollution and degradation, and lack of appropriate institutional management systems (El Raey, 2010). The northern coast of Egypt is extended over 3000km from Rafah in the east to ELsallum in the west, and could be classified into three parts; the west coast, the Nile Delta coast, and Sinai coast. The main Dynamic portion of this coastline of the Egyptian Mediterranean Sea is the middle part, particularly around the two river mouths, because of significant decrease of the sand supply from the land caused by construction of the Aswan High Dam. The Nile Delta Coast is one of the earliest recognized deltaic systems in the world. It extends in Egypt for more than 300 km from Alexandria to Port Said as shown in Figure 2.1. The Nile Delta was formed from the sediment discharged from historical branches of the Nile River. Figure 2.2 shows the present and historical branches of the Nile River.

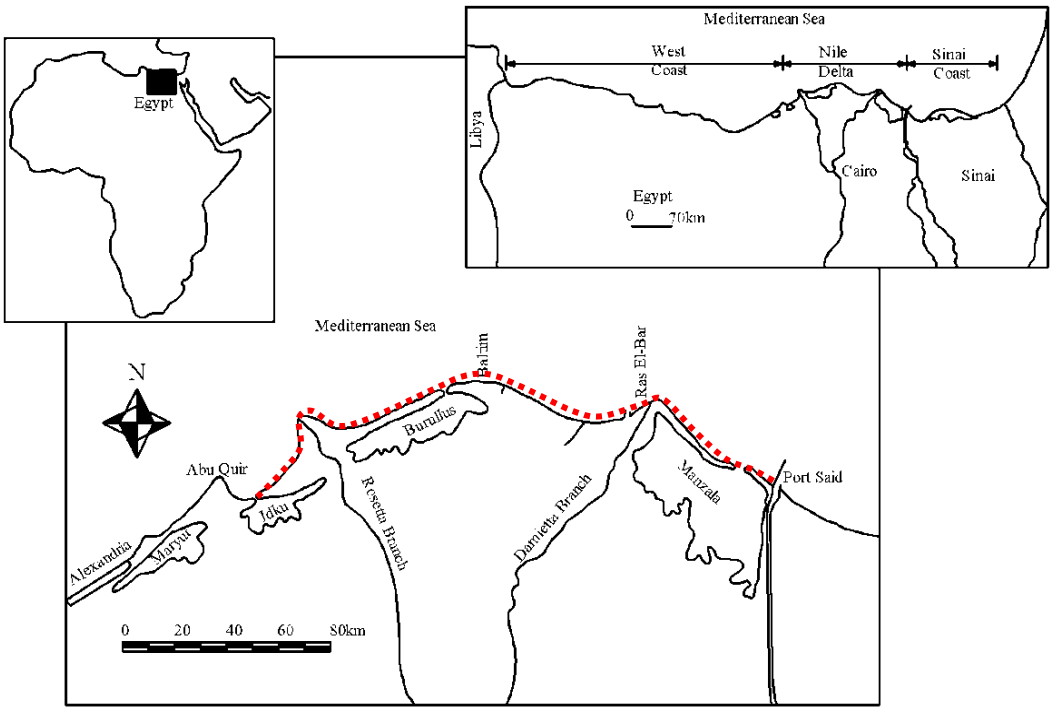

Figure 2.1. Location of the Nile Delta coast, and the study site.

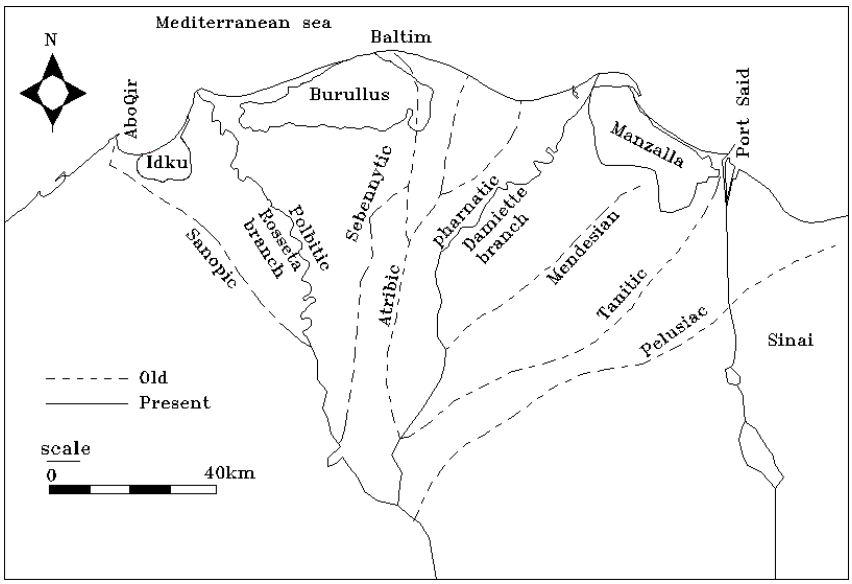

Figure 2.2. The Existing and old tributaries (UNDP, 1975).

2.2 Location and characteristics

The target study site is a part of the Nile Delta Coast, located between latitude 31° 0' 0" N to 32° 0' 0" N and longitude 30° 0' 0" E to 32° 25' 0 E. Figure 2.1 shows the top view of the target site. The coast line has the shape of concave and convex. It has four apexes; Abo Qir, Rosetta, Baltim, and Damietta. The Nile River branches are extruding the Delta. Both east and west sides of the coast are bounded by two jetties, i.e. jetty of Idku Lake and Port Said breakwater. The Nile Delta Coast consists of sandy beaches and has 250 km stretch of the coast line and faces to the Egyptian Mediterranean Sea. Seven outlets are exist within the study site, Idku Lake, Rosetta branch, EL Burullus laket, Gamasa drain, Damietta branch, and EL Gamiel 1&2.

2.3 Geomorphologic structure

The Nile Delta has different geomorphologic structures; desserts, coastal dunes, carbonate ridges, marches, lagoons, beaches, and backshores as shown in Figure 2.3. The desert is dominated in Sinai and Carbonate ridges exist near Alexandria. The beaches are backed by coastal flats and the sand dunes are subsisting at different locations. Four shallow highly polluted lagoons (Maryout, Idku, El Burullus, and Manzala) are distributed in the Nile Delta. These lagoons receive a great amount of agriculture drainage, sewage and industrial effluents before discharging to the Mediterranean Sea. The water level in Maryout is 1.2 m below the sea level and has no direct contact with the Mediterranean Sea, while the other three lagoons are

connected to the sea. Sand dunes exist near Idku, El Burullus (Figure 2.4), Baltim, and Gamasa. The dunes (longitudinal and crescentic forms) origin is interpreted as the result of coastal drifting and the subsequent transport of the former Sebennitic Nile branch sediments eastward by the predominant longshore current and by Aeolian processes (El Banna, 2004) . Most of the dunes in the study area have been subjected to deterioration and removal due to the construction of summer resort buildings and making the international coastal highway (El Banna, 2004).

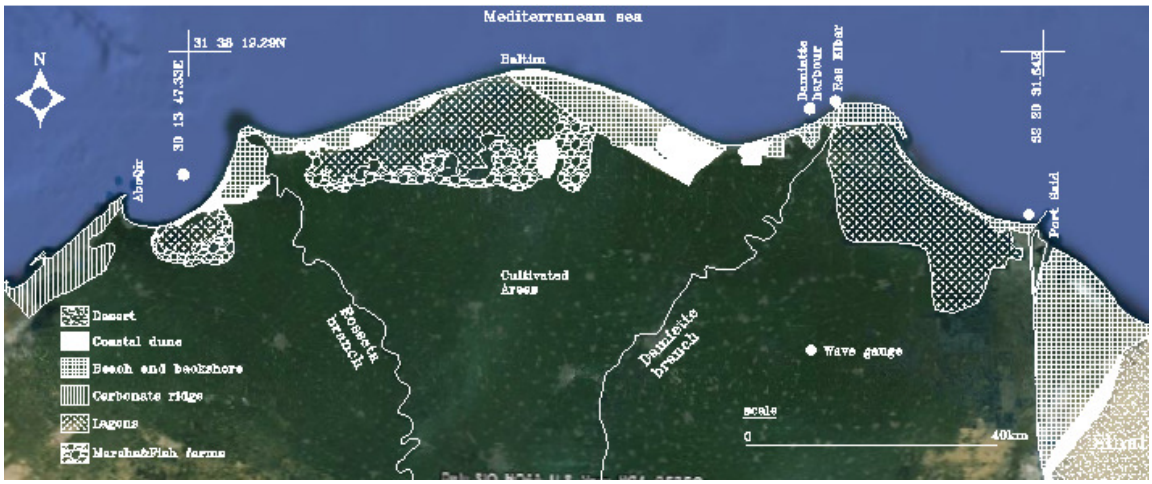

Figure 2.3. Geomorphologic structure of the Nile delta coast and locations of wave gauges, Frihy, and Lawrence (2004).

Figure 2.4. Sand dunes near Idku and EL-Burullus lake.

2.4 Wind and Waves

The predominant wind direction (60-50% of the year) is the NW and WNW directions, while wind from NE takes 10–15% of the year (Fanos, 1995), Average wind speed is seasonal in intensity, being 3-5 m/s in summer and spring; 5-7 in winter with the higher speed from the NW direction (Banna and Frihy, 2009). The waves in the study area are seasonal, with predominated

direction from the north-northwest. Low regular swell of 75 cm with 9-10 s wave period were noticed during the summer season (June to August), with calm waves during September and December (Manohar, 1981). Sixteen storms occur per year during the winter (November to march), the predominated wave is 2.5m wave height and 7-8 sec wave period, and the maximum wave height reaches 3.3m with the probability of occurrence for one time at least per year (Khafagy, 1979). From April to May, irregular waves are noticed with different directions (Manohar, 1981).Wave roses for different locations (Abo Qir, Rosetta, Ras Elbar, Damietta port, and Port Said) for different time periods along the Nile delta coast are illustrated in Figure 2.5. The locations of the wave gauges are shown in Figure 2.3. The data of the Port Said were measured by the Ministry of Electricity and Suez Canal Authority, and the other wave gauges were installed by the Coastal Research Institute in Alexandria.

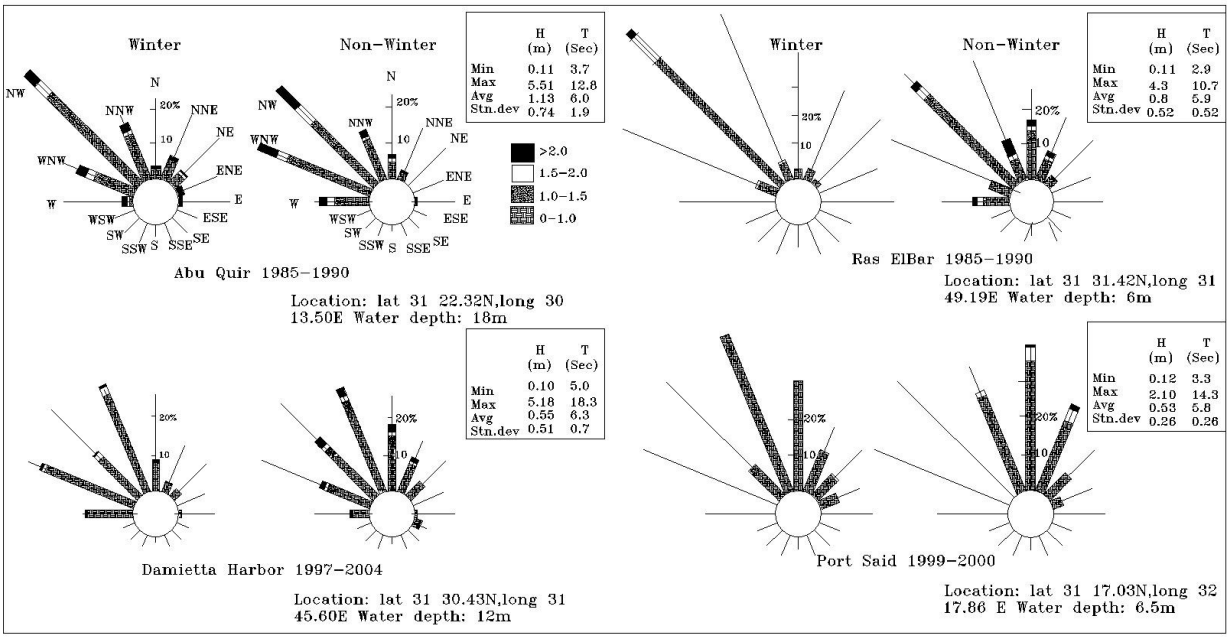

Figure 2.5. Wave roses for the study area, Frihy et al. (2010).

2.5 Tide, sea level rise, and land subsidence

The tide along the delta coast is semi-diurnal with a range 25-30 cm. The highest recorded water level is about 80 cm and the lowest level is -64 cm (UNECO/UNDP). British Admiralty records for the semi-diurnal, microtidal tides at Alexandria and Port Said show that tidal changes do not exceed 25-30 cm (Haslam, 1984). The delta is subsiding at rates of 0.1-0.5 cm per year (Stanley, 1990). Figure 2.6 present the subsidence within the Nile Delta. The sea level rise over the next

century is estimated to be varied from 56 cm to 3.45 m (Blodget, 1991). The sea level rise has, by itself, a relatively minor effect on coastal erosion, and estimates of local future sea-level rise by the year 2100 at Alexandria and Port Said, respectively, is expected to be 37.9 and 44.2 cm (Frihy, 1992). The yearly average sea level rise from 1930 to 1990 near Alexandria and Port Said is illustrated in Figure 2.7. At both locations the trend is increasing with average rate of 0.5 cm /per.

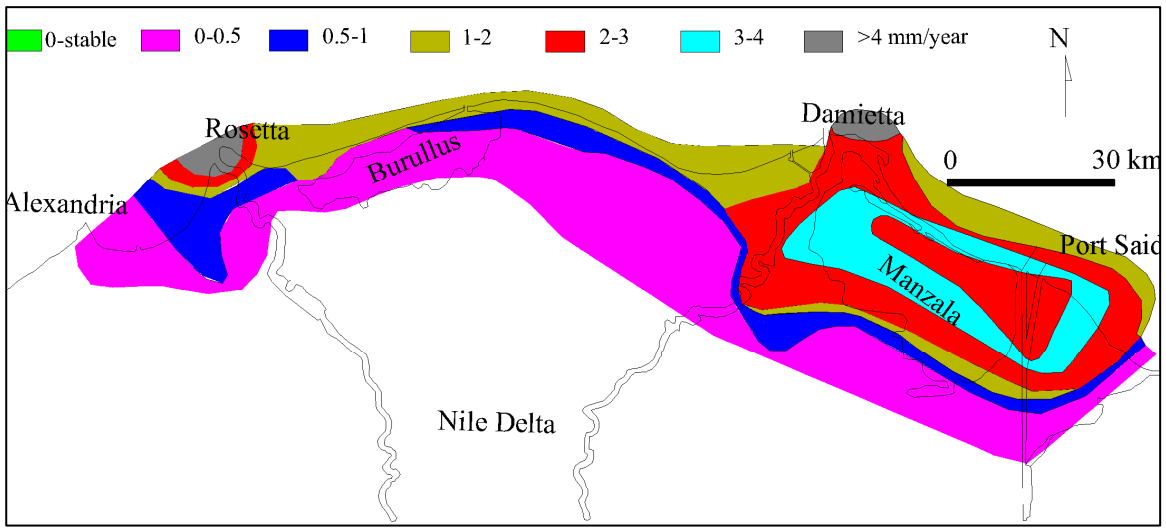

Figure 2.6. Land subsidence within the Nile Delta (Stanley, 1990).

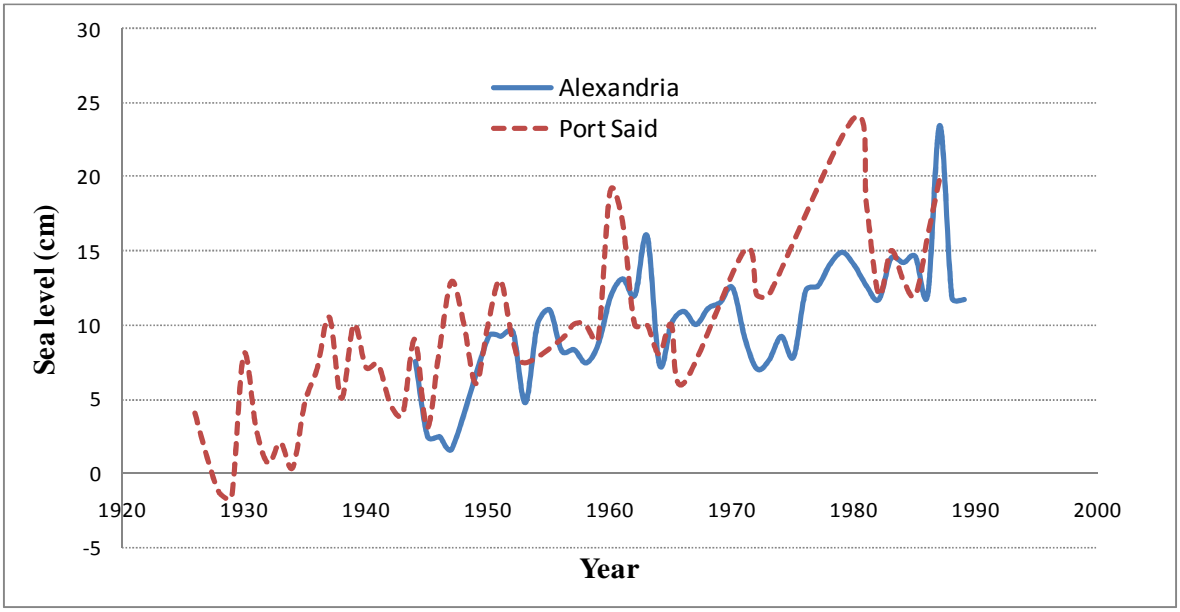

Figure 2.7. Yearly average mean sea level in Alexandria and Port Said port (Frihy, 1992).

2.6 Coastal structures

Construction of coastal structures such as revetment, seawalls, breakwaters, jetties, headland, and submerged breakwaters (hard stabilization) can be effective countermeasure to decrease the erosion or accretion. It sometimes increases the erosion problem or just shifts the erosion to the adjacent areas. The impact on the change of the natural conditions can increase the risk of erosion. In addition, these coastal structures are expensive and aren't permanent, and require costly maintenance to ensure that they continue to provide protection. Moreover, it Diverts storm water and waves into other properties and disturbs the land and disrupts natural water flows. On the other side there are other alternative countermeasures for coastal protection such as nourishment, dunes, and coastal plantation (soft stabilization) or sand-bypassing, which keep the natural conditions and have low impacts on environments. The hard stabilization appears at many locations along the Nile Delta Coast. About 25% of the coastal line is protected by coastal structures as shown in Figure 2.8. Description of more details about the coastal structures is presented in the next sections.

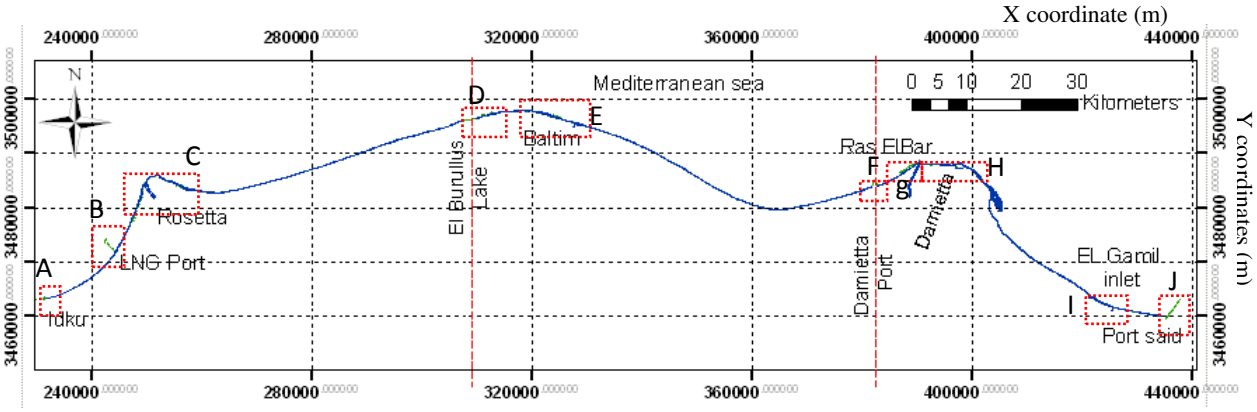

Figure 2.8. The locations of the coastal structures along the Nile Delta Coast.

2.1.1 Idku lake

Idku Lake entrance exists in the west side of Abo Qir bay. It is bounded the study site from the west. The entrance is located at 31°16'18.40"N latitude, 30°10'40.30"E longitude, and it is the only entrance from the Mediterranean Sea to Idku lake. Two Jetties were constructed in 1982 around the inlet of Lake Idku in order to protect the navigation channel from the sedimentation problems,

Figure 2.9. The west jetty has a length of 240 m, while the east jetty is 175 m long. Maadi fishing port was constructed in 1995 in the eastward side of Idku inlet. Jetties around the inlet were extended, the west jetty extended to be 340m length and the east jetty is 525 m. The east jetty is used as a breakwater for the fishing port. Additional jetty with 450 m length was constructed to protect the port from the prevailing wave directions (NW-NNW).

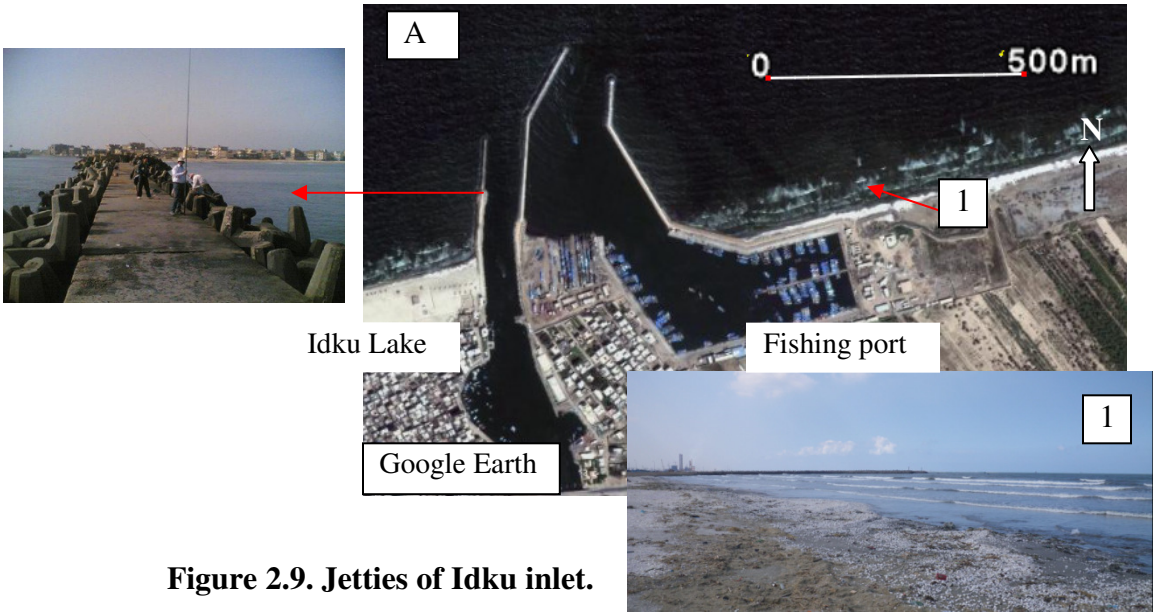

Figure 2.9. Jetties of Idku inlet.

2.1.2 Liquefied Natural Gas jetty and Idku Marina

Liquefied Natural Gas (LNG) port is located at Abu Qir Bay, 14 km to the west from Rosetta mouth, Figure 2.10. This Port is composed of open type jetty to the depth of 15m, and ends by turning and berthing area. 750 m detached breakwater exists at the end of the Jetty. This port was constructed in 2004, and another marina is under construction beside this port.

2.1.3 Rosetta mouth

Rosetta is the left branch of the Nile River. The Rosetta mouth is located at 31°28'1.96"N latitude, 30°21'54.73"E longitude. The protection of the Rosetta promontory starts from 1989-1991 by constructing two seawalls 3.35 km on the west, and 1.5 km on the east (artificial embankment covered by dolls concrete blocks of 4 to 7 ton, stable for a scour depth of 8 m, with width varying from 48-70m, and with crest level of 6.75m above the mean sea level). TETRA-TECH (1984); mentioned that based on the measurement of the scour rates around the promontory, by the year 2019 the eastern wall, and by 2027 the western wall will be in dangerous state if the

scour goes in linear behavior, also it is noted that by 2041 the 50-year design lifetime of these seawalls will be terminated .

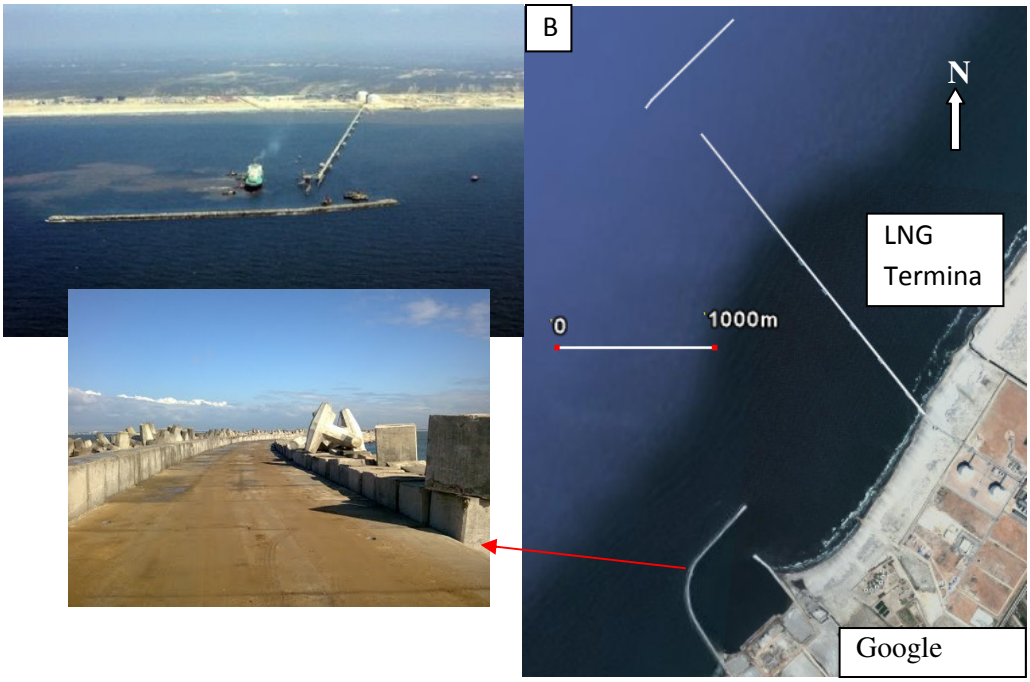

Figure 2.10. Idku LNG terminal and marine.

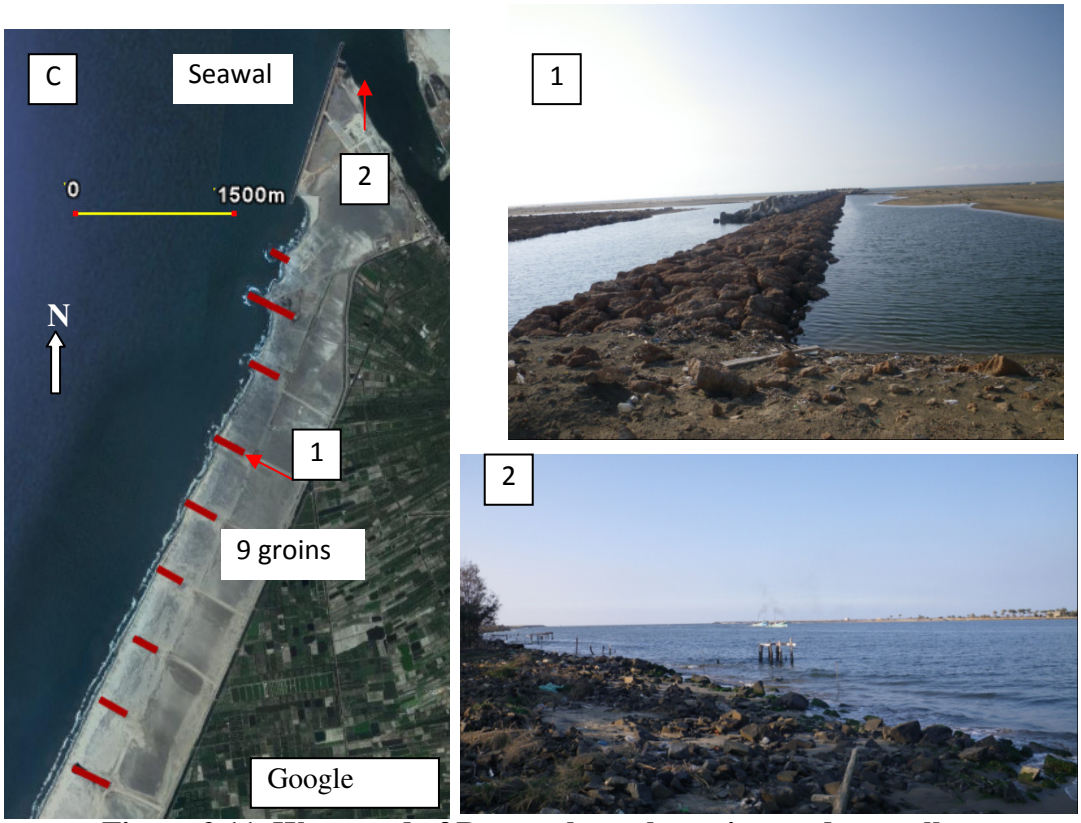

Figure 2.11. Westward of Rosetta branch, groins, and seawall.

Five groins were constructed in 2003 on the right side (with length varying from 400 to 500 m, and spaced from 800 to 900m), Figure 2.12. Nine groins were constructed starting from 2005 on the left side (with length varying from 250-450m, and spaced 450 to 700m), Figure 2.11.

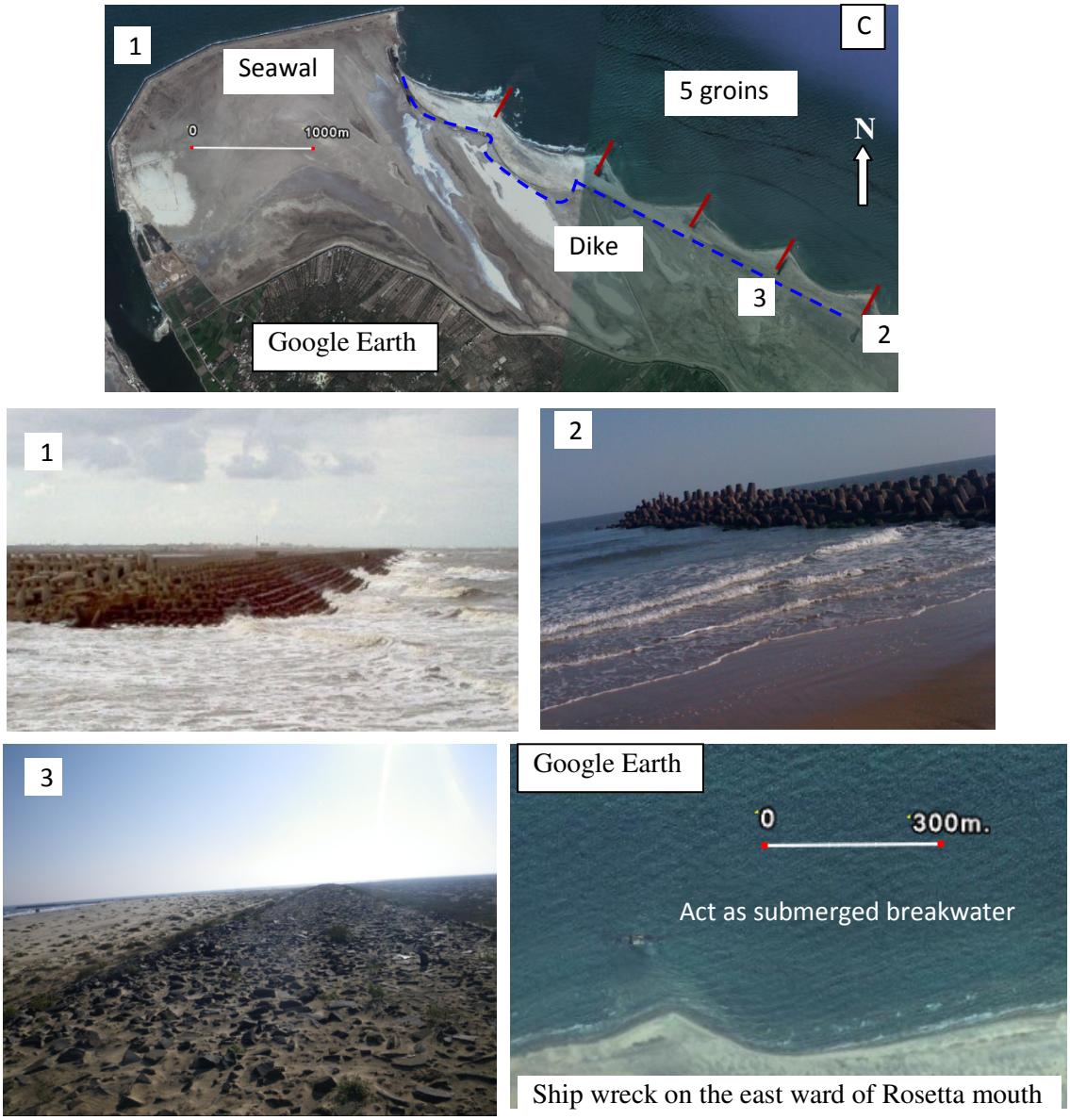

Figure 2.12. Eastward of Rosetta mouth, groins, dike, and seawall.

2.1.4 ElBurullus lake

El Burullus inlet and Baltim resort located approximately in the center of the Nile delta coast, in an active convex coastline which experienced erosion, and accretion. This area is characterized by the existence of barchans coastal dunes between El burullus inlet and Kitchener drain

(approximately 16 km length, 400 m to 1 km width perpendicular to the coastline, and 34 m as maximum height of these sand dunes). The Burrulus inlet is the only entrance from the Mediterranean Sea to El Burullus lagoon. The main problem in this area is the blockage of this inlet which results in major hazard of navigation. Many countermeasures were constructed around the inlet. Starting from 1947, seawall (600 m length) was built to protect the village of E1 Burg, and extended to the eastward (1400 m, basalt riprap revetment) in 1975. In 1971-1972 the west jetty of El Burullus inlet was constructed, and after 11 years in 1982-1983, the east jetty was constructed 250 m far from the west jetty. After 1990 another jetty on the east was constructed to keep the shape of the entrance, Moreover extension of the west jetty inside the sea. After 2003, fishing port was constructed on the west ward side of the inlet. The west jetty was used as a breakwater for the port and new breakwater was built on the left side of the west jetty. Two jetties and two breakwaters were constructed on the right side of the east seawall.

Figure 2.13, illustrate the current situation around El Burullus lake.

Figure 2.13. El Burullus inlet, jetties, and seawall.

2.1.5 Baltim resort

Baltim resort is 15 km on the eastward far from El burullus inlet, and it is one of many coastal places attracts the people during the summer season to enjoy the sea, and the sand. System of detached breakwaters was constructed in this area on stages to compact the erosion. Nine breakwaters (4-7 ton dolos, 250-350 m length, 220 m far from the coast, 300-400 m gap between each others, 3-4m water depth, and 2.5m crest level) were constructed between the years 1993-2002. Additional five breakwaters were constructed after 2003 with the same characteristics. Moreover short nine groins (75-100 m length, and 250-300 m apart) constructed on the eastward up to Kitchener drain. Google Earth image is presented in Figure 2.14, shows the fourteen detached breakwaters and the nine short groins.

Figure 2.14. Detached breakwaters, and groins at Baltim resort.

2.1.6 Damietta Port

Damietta harbor as presented in Figure 2.15 was constructed in 1984 in order to increase the trade along the Mediterranean coast. Damietta Port is situated at 31°28'56.58"N latitude, 31°45'29.41"E longitude, 8.5 km west of the Nile river of Damietta branch westward Ras El-Bar .The harbor constructed some distance inland to avoid the negative impact of the winter storms. In 1982, two jetties were constructed to protect the access channel from the littoral drift, which were extended in 1985. The western breakwater is 1640 m. long with 140 m land-based and 1500 m. sea-based area. The eastern breakwater is 738 m long with 200 m land-based and 538 sea-based area. Both breakwaters are made of stacked artificial acrobod piles topped with a

concrete head. These breakwaters obstruct the sediment which generally moving toward the eastward.

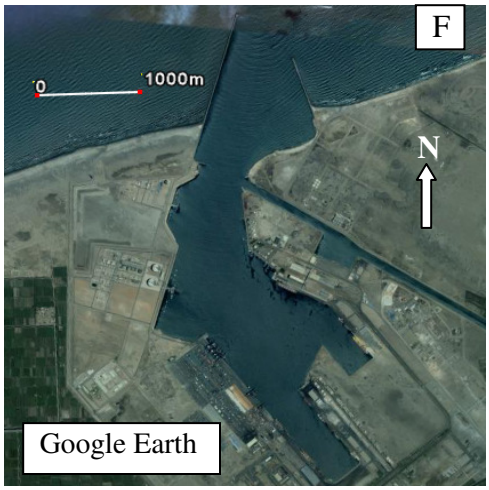

Figure 2.15. Damietta industrial port.

2.1.7 Ras El Bar resort

Figure 2.16 showing Damietta promontory. Ras El Bar is situated on the western flank of this promontory, 5 km on the eastward of Damietta harbor. The movement of the sediment was to the east and to halt the movement, jetty was constructed on the west side of the Damietta flank in 1940. To compact the erosion many structures were constructed later. Starting by a system of three groins in 1970, then revetment of basalt rock and dolose was placed between the groins in 1982-1983. The coastline change in this area is affected by the construction of Damietta harbor. Another system of groins were placed to sustain the sediment on the beach and to have a safe swimming area. The breakwaters are useful but the Currents and eddies generated in the gab areas between breakwaters have badly affected swimmers. The system of the breakwaters is composed of eight dolos detached breakwaters (4-7 ton unit weight, 200 m length, 200 m gap width, and 400 m far from the coastline).These breakwaters were installed in the period from 1990 to 2002. After that modification of the westward groins and additional breakwaters were constructed. This area is confined between the west jetty of Damietta flank, and the right jetty of Damietta harbor.

2.1.8 Damietta mouth

Damietta is the right branch of the Nile River. Damietta promontory located at 31°31'25.95"N latitude, 31°50'40.37"E longitude in the eastern half of the Nile delta. Many structures were constructed in this area. In 1976, jetty (260 m) on the eastward of Damietta flank was constructed to keep the shape of the River mouth. In 1971, vertical seawall was constructed to protect the coastal road between Damietta and Port Said but now it is not exist. Only an 800-m long segment of the western end of that seawall is still present. Another 6 km long dolos Seawall (4-7 ton concrete blocks) was constructed in 2000 onshore along the eastern side of the Nile mouth as one of the countermeasures to decrease the coastline change rates.

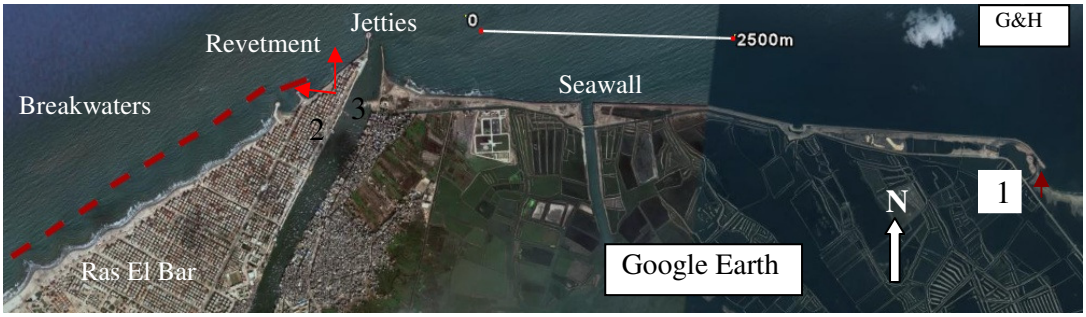

Figure 2.16. Damietta promontory, jetties, revetments, and detached breakwaters.

2.1.9 El Gamil inlet 1&2

There are two inlets (EL Gamil 1 &2) connecting Manzala lagoon with the Mediterranean Sea, Figure 2.17 (upper strip). Both inlets are located on the westward side of Port Said. Two jetties 225, and 250 m were constructed on the western and eastern sides of El Gamil inlet1 in 1972. Four detached breakwaters were constructed at 1996 parallel to the beach at El-Gamil zone on the westward of EL Gamil inlet 2. Each breakwater is 300 meter long and 200 meter gap between the breakwaters. Two additional breakwaters were constructed in 1998.

2.1.10 Port Said

The coastal road is protected by a bituminous dike of 3925 m length. The last end of the study site is the Port Said breakwater. This breakwater acts as a huge barrier of the sediment transport. This breakwater is extended over 7.7 km into the sea (submerged part and emerged part). It was 920m in 1864, and extended to its present length in 1924.

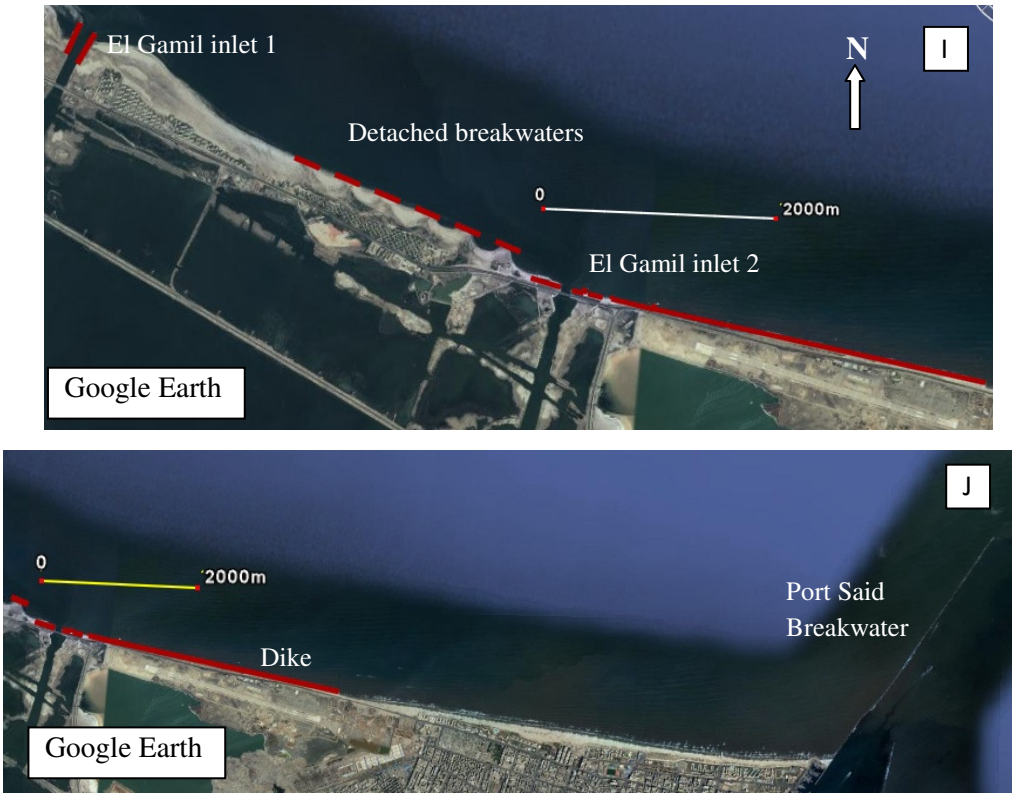

Figure 2.17. Port Said coast, El Gamil inlet, and Port said breakwater.

Chapter3 Analysis of Land-sat images

3.1 Introduction

To have a sustainable coastal protection, coastal zone monitoring has a great importance. Shoreline change is one of the cruical factors that were used in a coastal management and coastal hazerd assesment. Bin et al.(2008) divided the methods of soreline extraction into four categries; (i) conventional ground surveying, (ii) modern altimetry technology, (iii) airborne imagery,and (iv) satellite imagery. Chen and Rau, (1998) figured out that rader or laser altimeters has a great potential but the detectors are currently less avilable. All of these approaches have both advantages and disadvantages. While ground survey is the most conventional and accurte method, it is time-consuming and is not cost-effective (need intensive labor,and restricted by the difficulty of access). Both airborne and satellite imagery can overcome the difficulties of access (resricted areas). The satellite imagery has many advantages over aerial photography.For example, the satellite is operational all the time of the year and catures the images of the same area with certain frequency.Satellite image also captures larger areas with relatively high reolutions, No air traffic control restrictions, no aircraft, cameras or expensive equipmentuser are required. At the same time, the spatial resolution of the satellite images is low compared to aerial photography and cloud cover might exist based on the atmospheric conditions at the site.There are several satellites with different spatial/spectral resolutions in operation which could be used for shoreline extractions and detection of different features on the Earth surface. Different objects reflect or absorb different amounts of radiation with different wavelengths. The sensors detect the radiation reflected from objects on the Earth's surface and analysis of this spectral signature can assist in identifying what the object is. Commonly used satellites and their characteristics are summarized inTable 3.1.

Table 3.1.Some earth orbital Satellites and their characteristics.

Satellite	Sensor Type	Type	Satial resolution (m	Scene extents (km)	No of bands	Repeat cycle
Airborne sensors	variable	-	0.1-10m	variable	-	-
Terra	ASTER	Optical	15,30,90	60x60	14	4-16days
SPOT	Pan, MSS	Optical	2.5,5,10,20	60x60	4	2.5days
Landsat	MSS,TM,ETM+	Optical	15,30	185x170	8	16 days
ERS	ERS	RADAR	12.5	100x100	1	2.5 days
ALOS	Prism,AVINR,PALSAR	RADAR	4,10	35x35 up to 350x350	1	several times per year
IKONOS-2	Pan , MSS	Optical	1.4	11x11	1,4	1.5-3 days

Multispectral remote sensing satellites provide digital imageries in infrared spectral bands where the land-water interface is well defined. Furthermore this method has advantages in its time effectiveness, unexpensive executed cost and large ground coverage monitoring,Bin et al. (2008).

Identification of the shoreline using remotely sensed imagery started inthe 1930s utilising aerial photography(Chen and Rau, 1998). Many researchers use the remote sensing techniques to study the coastal changes along the NileDetaCoast especially around Rosetta,and Damietta promontory. Blodget, and Taylor,(1991) and Frihy et al. (1994) used the Landsat Multi-spectral Scanner (MSS) digital data to monitor coastal changes along the Rosetta Promontory. Dewidar and Frihy, 2008 used images from different satellites sensors MSS,TM,ETM from 1972 to 2006,and extracted the shorelines based on image threshold to band 4 for the MSS, and band 7 for TM/ETM+. Following the same method,Dewidar and Frihy, 2010 studied the shoreline change rates around Damietta promontory in the period between 1972 to 2007.

Much effort was exerted to optically detect the shoreline from the images. Various methods rely on the use of a supervised classification (human-guided, the spectral features (the brightness and "color" information) of some areas of known landcover types are extracted from the image. These areas are known as the "training areas". Every pixel in the whole image is then classified as belonging to one of the classes depending on how close its spectral features are to the spectral features of the training areas.Abd El-Kawy et al. (2011), detect the land use and land cover in the western Nile delta of Egypt using remote senseing using supervised classification technique.Other mrethod rely on unsupervised classiffication (calculated by software, the computer program automatically groups the pixels in the image into separate clusters, depending on their spectral features. Each cluster will then be assigned a landcover type by the analyst).Frihy etal.(2009) detect the spit evolution,margin changes of Manzala lagoon and its islands using unsupervised technique. Various thresholding techniques, as followed by (White and Asmar, 1999),and (Dewidar and Frihy, 2008)are also used in the detection of the shoreline.

3.2 Review on the use of Land sat images, and their characteristics

Ground surveying was the most commonly used technique to determine the coastline maps in the period from 1807 to 1927. After 1927 aerial photographs were known as the sole source

for coastal mapping until 1980. However, large number of aerial photographs are required for coastline mapping, even for a regional scale, Alesheikh et al. (2007). From 1972 the digital images provided by Landsat and other remote sensing satellites were commonly used.The Landsat Program, a joint effort of the U.S. Geological Survey (USGS) and the National Aeronautics and Space Administration (NASA), was established to routinely gather land imagery from space; consequently, NASA develops remote-sensing instruments and spacecraft, then launches and validates the satellites. The USGS then assumes ownership and operation of the satellites, in addition to managing all ground-data reception, archiving, product generation, and distribution(USGS-EROS).Sevensattelites were launched to collect the data around the Earth. The Landsat 1, 2, and 3 satellitesorbited at an altitude of 920 kilometers,and carried the Multispectral Scanner (MSS) sensor; the Landsat 4 and 5 satellites orbited at 705 kilometers,and carry both the MSS and the Thematic Mapper (TM) sensors; and the Landsat 7 satellite orbited at 705 kilometers, and carries the Enhanced Thematic Mapper Plus. Table 3.2,summarizes the charactristics of the different sattellites and the use of different bands. Each sensor has different bands. Each band or combind bands could be used to detect specific feature as different features (vegetation, urban development, rock formation, soil water content etc) yield different spectral response.The sensor's on board the Landsat Satellites records the surface reflectance of electromagnetic (EM) radiation from the sun in seven discreet bands including visible light and three bands beyond visible light within the infrared portion of the spectrum.

Here, the shoreline detected from the landsat images twice; the first time using single band, and the second time using multispectral bands. Since the use of the infrared wave band has the advantage in removal of the haze and enhancement of land-water boundaries. Band 7 for MSS (0.80-1.01μm) and band 7 (2.08-2.35μm) for TM, and ETM were used as the first trial to extract the shoreline. The second trial is to use multispectral infrared bands; 4, 5, 6, and 7 for MSS, and 4, 5, 7 for TM, and ETM.The detected shorelines were analyzed to quantify the erosion and accretion pattern along the coastline of the Nile Delta, from Idku lake to Port Said. The 250 km coastline of the Nile Delta has been changed drastically in the last few decades. The hot issue is the coastal erosion problems especially around the two river mouths. The Rates of shoreline changes were calculated from the shoreline positions generated at 2350 locations using a Digital Shoreline Analysis System (DSAS) version 4.0. The methodology of the detection of the shoreline and the analysis of the changes are presented in the next section.

Table 3.2. The characteristics of the Land sat missions by USGS.

			Return Bream Vidicon (RBV)			Multispectral scanner (MSS)					
Working years	Landsat	Rsolution/pixel size	Band1	Band2	Band3	Band4	Band5	Band6	Band7	Scene size	Repeat cycle
1972-1978 1975-1983 1978-1983	Landsat1,2,3	80m (57x79m)	Visible blue-green (475-575 nm)	Visible orange-red (580-680 nm)	Visible red to Near-Infrared (690-830 nm)	Visible green (0.5 to 0.6 nm)	Visible red (0.6 to 0.7 nm)	Near-Infrared (0.7 to 0.8 nm)	Near-Infrared (0.8 to 1.1 nm)	170kmx185km	18 days
use						Emphasizes sedimentladen water and delineates areas of shallow water	Emphasizes cultural features	Emphasizes vegetation boundary between land and water, and	Penetrates atmosphere haze best; emphasizes vegetation, boundary between land and water, and landforms		

			Thematic Mapper (TM)								
Working years	Landsat	Rsolution/pixel size	Band1	Band2	Band3	Band4	Band5	Band6	Band7	Scene size	Repeat cycle
Land sat 3(1982-1993) & Land sat 4(1984- now in 1995 MSS powered off)	Landsat4,5	30 m reflective, 120 m thermal	Visible (0.45 → 0.52 nm) 30 m	Visible (0.52 → 0.60 nm) 30 m	Visible (0.63 → 0.69 nm) 30 m	Near-Infrared (0.76 → 0.90 nm) 30 m	Near-Infrared (1.55 → 1.75 nm) 30 m	Thermal (10.40 → 12.50 nm) 120 m	Mid-Infrared (IR) (2.08 → 2.35 nm) 30 m	170 km x 185 km	16 days
						Multispectral scanner (MSS)					
						Band4	Band5	Band6	Band7	Scene size	Repeat cycle
		80m (57 x 79 m)				Visible green (0.5 to 0.6 nm)	Visible red (0.6 to 0.7 nm)	Near-Infrared (0.7 to 0.8 nm)	Near-Infrared (0.8 to 1.1 nm)	170 km x 185 km	16 days

			Enhanced Thematic Mapper (ETM)									
Working years	Landsat	Rsolution/pixel size	Band1	Band2	Band3	Band4	Band5	Band6	Band7	Band 8	Scene size	Repeat cycle
1993- now	Landsat6	30 m reflective, 120 m thermal	Visible (0.45 → 0.52 nm) 30 m	Visible (0.52 → 0.60 nm) 30 m	Visible (0.63 → 0.69 nm) 30 m	Near-Infrared (0.76 → 0.90 nm) 30 m	Near-Infrared (1.55 → 1.75 nm) 30 m	Thermal (10.40 → 12.50 nm) 120 m	Mid-Infrared (2.08 → 2.35 nm) 30 m	Panchromatic (PAN) (0.52 - 0.90nm) 15 m	170 km x 185 km	16 days

			Enhanced Thematic Mapper plus (ETM+)									
Working years	Landsat	Rsolution/pixel size	Band1	Band2	Band3	Band4	Band5	Band6	Band7	Band 8	Scene size	Repeat cycle
1999- now	Landsat7	30 m reflective, 60 m thermal	Visible (0.45 → 0.52 nm) 30 m	Visible (0.52 → 0.60 nm) 30 m	Visible (0.63 → 0.69 nm) 30 m	Near-Infrared (0.76 → 0.90 nm) 30 m	Near-Infrared (1.55 → 1.75 nm) 30 m	Thermal (10.40 → 12.50 nm) 120 m	Mid-Infrared (2.08 → 2.35 nm) 30 m	Panchromatic (PAN) (0.52 - 0.90nm) 15 m	170 km x 185 km	16 days
use			Bathymetric mapping; distinguishes soil from vegetation; deciduous from coniferous vegetation	Emphasizes peak vegetation, which is useful for assessing plant vigor	Emphasizes vegetation slopes	Emphasizes biomass content and shorelines	Discriminates moisture content of soil and vegetation; penetrates thin clouds	Useful for thermal mapping and estimated soil moisture	Useful for mapping hydrothermally altered rocks associated with mineral deposits			

3.3 Methodology

The entire system of satellite-based shoreline monitoring consists of several processes: (i) acquisition of the shoreline from the Land-sat images data collection, image preprocessing, unsupervised classification and change detection;and (ii) analysis of the rates of the erosion and accretion based on linear regression and empirical functions.Figureillustrates the work flow of the entire system of shoreline change analysis based on satellite images.

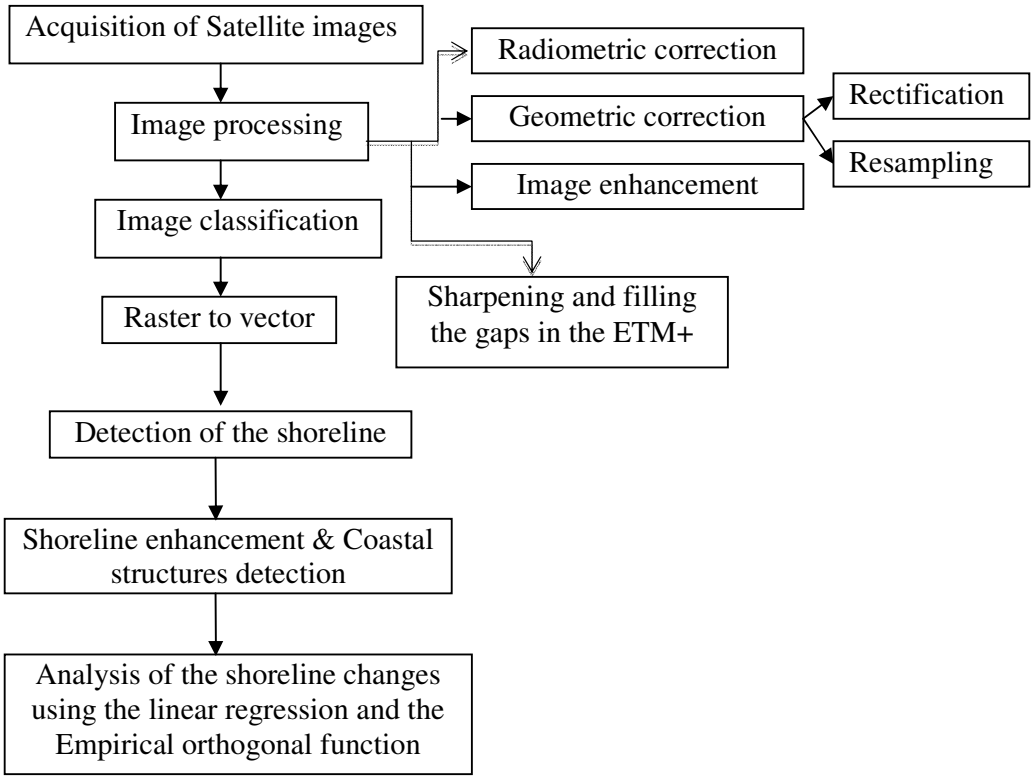

Figure 3.1.Diagram of the research workflow.

3.3.1 Acquisition of the shoreline from the land-sat

3.3.1.1 Data collection

Satellite images used for this study were obtained from the United States GeologicalSurvey (USGS) Earth Explorer free of charge. 11 Land-Sat images were acquired within 37 years starting from 1973 till 2010 at unequal interval spanning as described in Table 3.3.The dates of constructing the countermeasures were taken into consideration when landsat acquisition time is chosen.Each respective image was obtained from Landsat constellation of

satellites.TheNileDeltaCoast is located within the dataset of World Reference System path 189,190 and Row38 for MSS and within path 176,177 and Row38 for both TM and ETM+. The used images are with correction level 1-T. The Standard Terrain Correction (Level 1T) provides systematic, radiometric and geometric accuracy by incorporating ground control points (GCP's) while employing a Digital Elevation Model (DEM) for topographic accuracy. Geodetic accuracy of the product depends on the accuracy of the ground control points and the resolution of the DEM used.

Table 3.3.The Land-Sat images used in the research and their specifications.

Date of acquisition	Satellite	Sensor	Path/Row	Correction level
May,07,1973	Landsat 1	MSS	189/038	Level 1-T
May,10,1973			190/038	
May,10,1978	landsat3	MSS	189/038	
May,21,1978			190/038	
Sep,20,1984	landsat5	TM	176/038	
Sep,11,1984			177/038	
Apr,22,1987	landsat5	TM	176/038	
May,31,1987			177/038	
May,15,1990	landsat4	TM	176/038	
Aug,4,1990			177/038	
Apr,20,1998	landsat5	TM	176/038	
Aug,1,1998			177/038	
Jul,6,2000	landsat7	ETM+	176/038	
Apr,24,2000			177/038	
Aug,8,2003	landsat5	TM	176/038	
Sep,9,2003			177/038	
May,17,2005	landsat7	ETM+	176/038	
Mar,5,2005			177/038	
Jul,10,2007	landsat7	ETM+	176/038	
Jul,1,2007			177/038	
May,6,2010	landsat7	ETM+	176/038	
May,15,2010			177/038	

3.3.1.2 Image processing

These images are already geometrically corrected (rectified, resampled) based on WGS84 ellipsoid and Universal Transverse Mercator (UTM) projection for zone 36 N. The images are somehow radiometrically calibrated except for the atmospheric effect for all sensors and missing line data for ETM+ sensor. The main disadvantage of using the Land-sat images here

is the presence of the clouds in the images, thus we selected images without clouds. In order to ensure the waterline mapping accuracy, image data with 3 x 3 edge enhancement filters was used to sharpen the boundary between water and land classes. Failure of the ETM sensor occurred in may 2003 results in missing lines of data in the image. Since that time all Landsat ETM images have had wedge-shaped gaps on both sides of each scene, resulting in approximately 22%-loss of the data. For these missing line data; additional image was used to fill the gaps in the original image. The acquisition data of the additional data should be near to the acquisition data of the original one. Model in Erdas 8.4 is used to mosaic the data from the additional image to the original image at the missing lines locations. Figure 3.2, shows a part of the 2004 image around Rosetta mouth and part of the 2010 image around Damietta before and after filling the missing line data. The gaps have width from 140 m up to 350 m based on the locations,and it is reduced to 20 m.

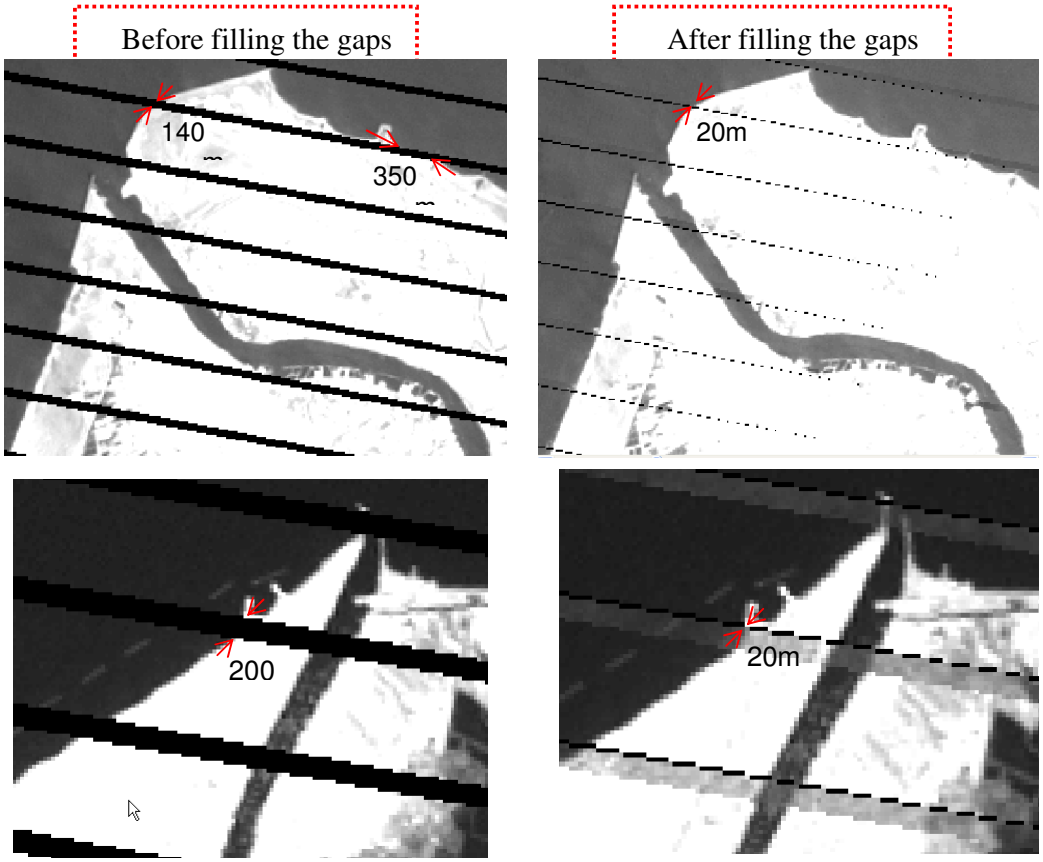

Figure 3.2.Parts of the landsat image before and after filling the gaps.

Pan-sharpening was done on ETM images to merges high-resolution panchromatic data (pan - Landsat-7's band 8) with medium-resolution multispectral data from bands 1, 2, 3, 4, 5,and 7 to create a multispectral image with higher-resolution features (15 m) as shown in Figure 3.3.

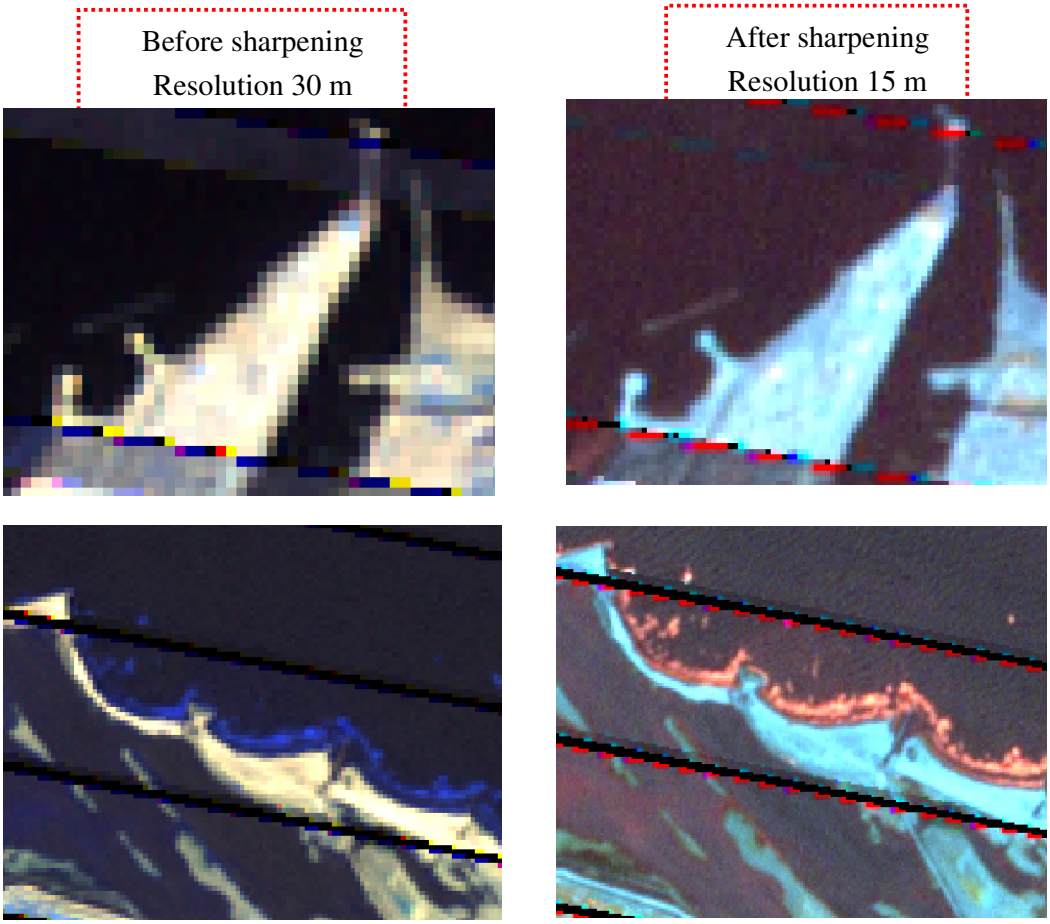

Figure 3.3. Parts of the 2007 landsat multispectral image before and after Pan-sharpening.

The images were unsupervised classified using Isodata algorithm.The clusters were classified into two; one is the water and the other is elsewhere. There are various techniques to classify the image to its Land/sea components as density slicing,ratio,isodata,edge detection,and region growing.**The density slicing** is a single band image classification technique. This technique divides the image digital number (DN) into clusters or slices based on their brightness,and the number of slices and boundaries between clusters depend on type of land covers of the area. It is envisaged that the highest or lowest DN values representing the sea or the boundaries between the sea and the land. Band **ratioing technique** needs bandsin

which,the DN value in one band at a specific X,Y is divided in another band. Energy reflectance for water is higherin the green and red portions of the electromagnetic spectrum compared to thatof the NIR band. Therefore, when pixels in the green and/or red bands aredivided by corresponding pixels in the NIR band, discrimination of water shouldbe achievable. Vegetation index is one of the indexes which could be used aswell to decrimnate the shoreline loaction. **Edge detection** technique defines the abrupt changes in the intensity of brightness in each pixel, with lower intensity pixels made darker and higher intensity pixels made lighter. Before applying edge detection it would be better to enhance the contrast between land and sea using filter (low-pass filters, or high-pass filter). **Region Growing** technique is a trial and error technique. In this technique, the image is divided into regions based on the spectral and spatial properties such as sea and land. **Isodata algorthim** (ERDAS, 1997) is an iterative Self-Organizing Data Analysis algorthim (ISODATA) for classification,whereby uses spectral distance , iteratively classifies the pixels, redefines the criteria for each class, and classifies again, so that the spectral distance patterns in the data gradually emerge.Pixels that are closest to the specific cluster centre are then included into that cluster and the center of each claster is then recalculated after the new pixels were included in the cluster. Iterating these procedures, ISODATA finally classifies the entire image into two clusters,one is the sea and the other is the land. The use of the ISODATA has the advantages in that: (i) the technique is not geographically biased to the top or bottom pixels of the data file; and (ii) it does not matter whereever the initial arbitrary cluster centers are located as long as enough iterations are assured.

Figure 3.4, shows part of Land sat image around Rosettaand Damietta promontory before and after classification. The white color represent the land and the grey color represent the sea.

After classification of the clusters, obtained data format was converted from raster to vectorand then shoreline locations were extracted as boundary between two clusters, i.e.,the one on land and the other on the sea.Here, the shoreline detected from the landsat images twice; the first time using single band, and the second time using multispectral bands. Band 7 for MSS (0.80-1.01μm) and band 7 (2.08-2.35μm) for TM, and ETM were used as the first trial to extract the shoreline. The second trial is to use multispectral infrared bands; 4, 5, 6, and 7 for MSS, and 4, 5, 7 for TM, and ETM. The extracted shorelines from the two trials were enhanced and the final shoreline is determined as the one whose root mean square error from these two extracted shorelines is minimized. The coastal structures were interpreted and

digitized from the images presented by Google earth.**Error! Reference source not found.**,shows part of Land sat image around Rosetta mouth after detecting the shoreline and placing the coastal structures.

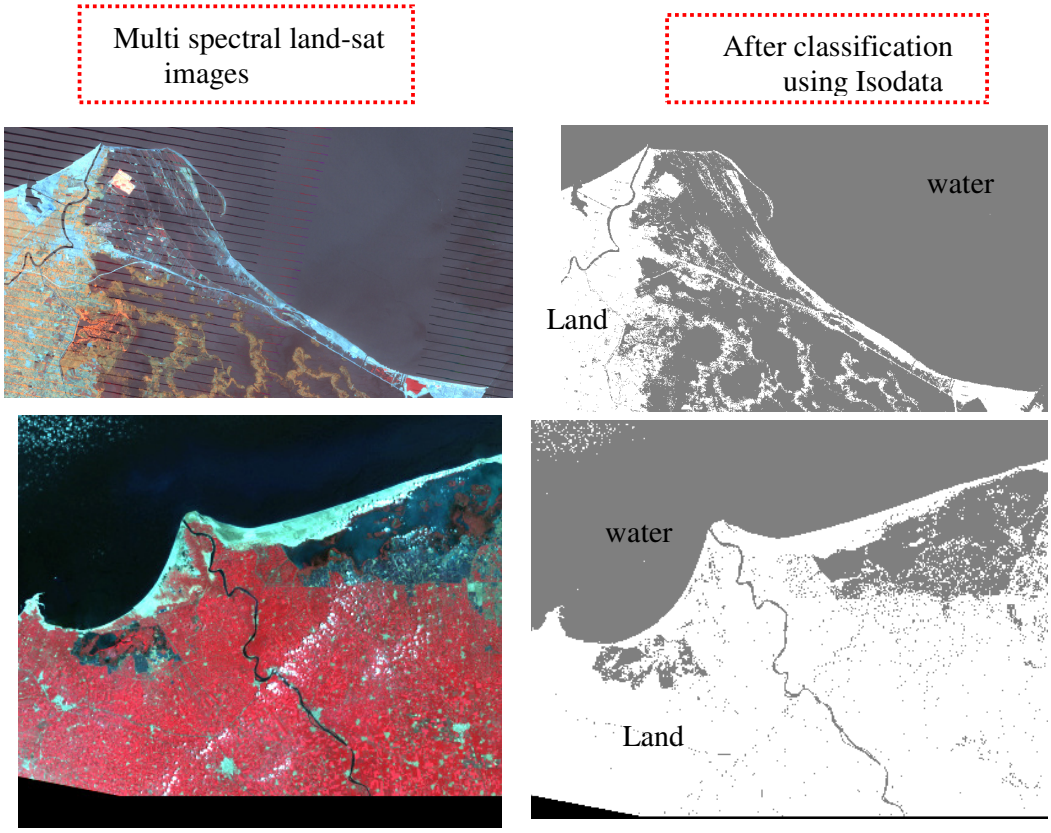

Figure 3.4. Parts of the 2007 landsat multispectral image before and after Classification.

3.3.2 Linear regression analysis

Shoreline data set extracted from the landsat images were used for calculations of the shoreline changes. The rates of the shoreline change were determined by comparing the shoreline positions at different times and different alongshore locations with horizontal intervals of 50m and the total grid numbers of around 2350.There are different statistical approaches for calculating the rates, i.e., EPR (End point rate), LRR (Linear regression rate), and LMS (Least median of square). This study calculated the rates of moving shoreline based on the linear regression. In the linear regression method, least-squares regression line is fitted to all shoreline points along the particular transect. The regression line is placed so that the sum of the squared residuals determined by squaring the offset distance of each shore line position from the regression line is minimized. In order to assess the accuracy of the results, calculated shoreline change rates at 31 different locations based on the present satellite-

extraction technique were compared with the ones based on the direct field survey results for the period from 1972 to 1990 (Frihy and Komar 1993).

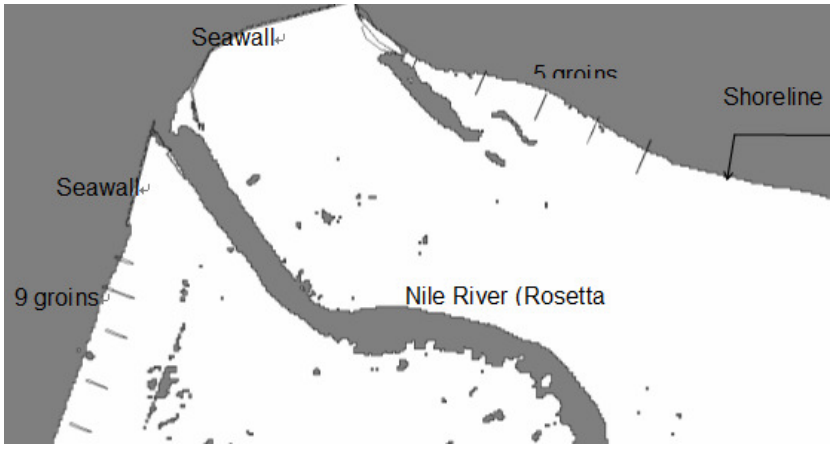

Figure 3.5. Part of the landsat image after detecting the shoreline.

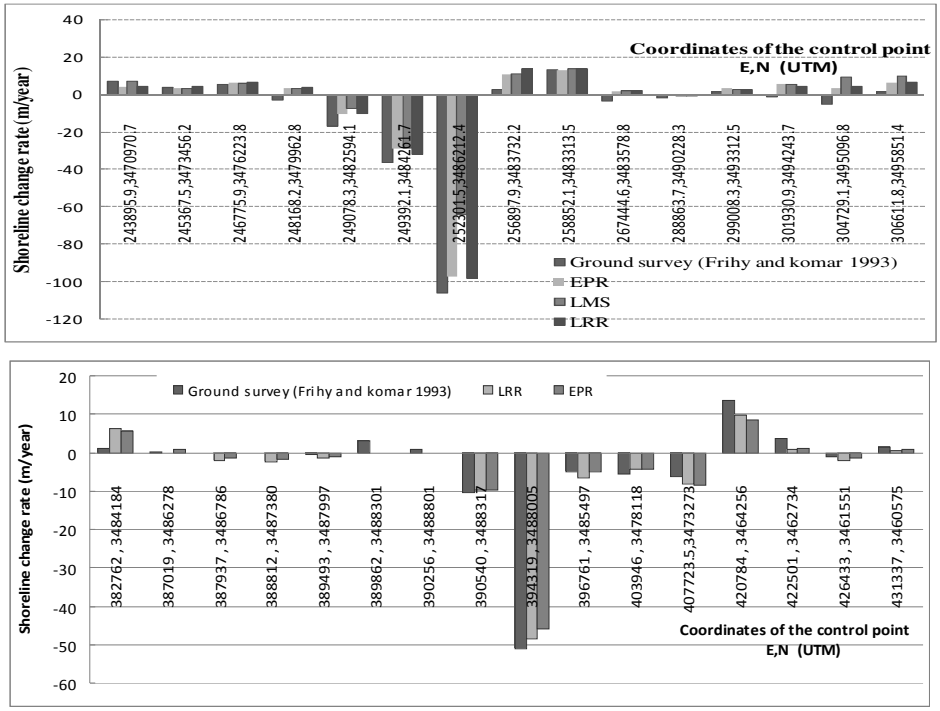

Figure 3.6.Comparison between the rates obtainedby field survey (Frihy and Komar, 1993) and the calculated ones (the upper part is around Rosetta promontory and the lower part around Damietta promontory).

The comparison in Figure 3.6 shows relatively good agreement at many locations amongestimated shoreline change rates basd on different statistical methods. The differences between the direct field survey rates and the present calculated rates should be partially due to the the difference in the number of the available data, and more dominantly due to the

difference in the transect angle (at which direction they measured the location of the shore line).

3.3.3 Empirical orthogonal function analysis

Further investigation of the shoreline data set was performed based on the Empirical Orthogonal Function (EOF) analysis technique. Here EOF is used to decompose the time and spatial variations of the shoreline locations into different modes, i.e., to distinguish cross shore movement and longshore movement of the shoreline with factors which indicates the relative importance of each mode. In this manner, this study aims to investigate the effect of the coastal structures. The EOF analysis is based on the separation of the temporal and spatial dependence of the data so that it can be represented by a combination of corresponding function of time and space. This statistical technique was introduced by the meteorologists (Lorenz, 1956). This technique was first introduced to the coastal studies by Winant et al. (1975). Many researches followed this study and applied EOF to the coastal engineering field to descibe the cross shore and long shore variabilities (e.g.,Miller and Dean, 2007 and Liu et al. 2010).The original time series of the shoreline around Rosetta promontory is given by:

$$y(x,t) = \sum_{k=1}^{n} y_k(x,t) = \sum_{k=1}^{n} PC(t).EOF(x) = \sum_{k=1}^{n} a_k.C_k(t).e_k(x) \tag{3.1}$$

$$a_k = \sqrt{\lambda_k n_x n_t} \tag{3.2}$$

where each column contains the spatial observation at specific time, y_k is the k-th combined eignfunction pair (spatial and temporal), n is the number of modes, the lesser number of the temporal (n_t) or spatial (n_x) samples, EOF(x) (spatial eigenfunction) is the spatial structure of the major factors that account for spatial variation of y, Pc (t) (temporal eigenfunction) is the principal component that show how the amplitude of each EOF varies with time, a_k is the eignvalue associated with the kth eigenfunction, $e_k(x)$ and $c_k(t)$ are the spatial and temporal eigenfunctions respectively.

3.4 Results and discussion

Three main promontories separated by embayments are found along the NileDeltaCoast, i.e. Rosetta in the west, Damietta in the east, and El Burullus promontory midway between these two promontories. Figures 3.7, 3.8, and 3.9 show the Land-sat images around Rosetta mouth, El Burullus promontory, and Damietta mouth. Clear changes could be distinguished by comparing the land-sat at these locations.The long-term pattern of shoreline change along the

Nile DeltaCoast during the period from 1998 to 2010 is illustrated in Figure 3.10. The red clear represent the erosion while the blue represents the accretion. Various areas of erosion and accretion are present along the NDC, with the most severe erosion around the tips of Rosetta and Damietta promontories.

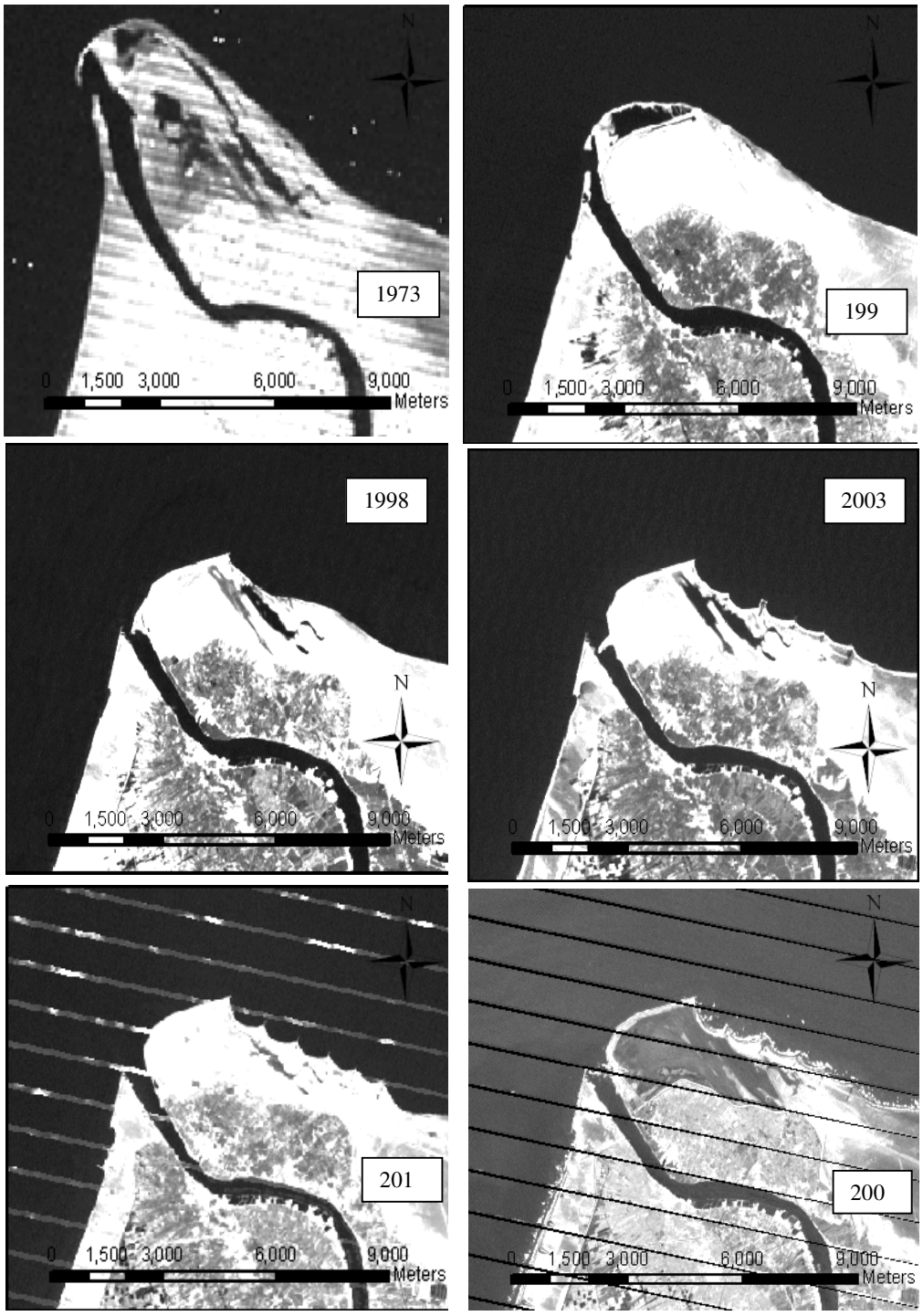

Figure 3.7. Land-sat images around Rosetta mouth.

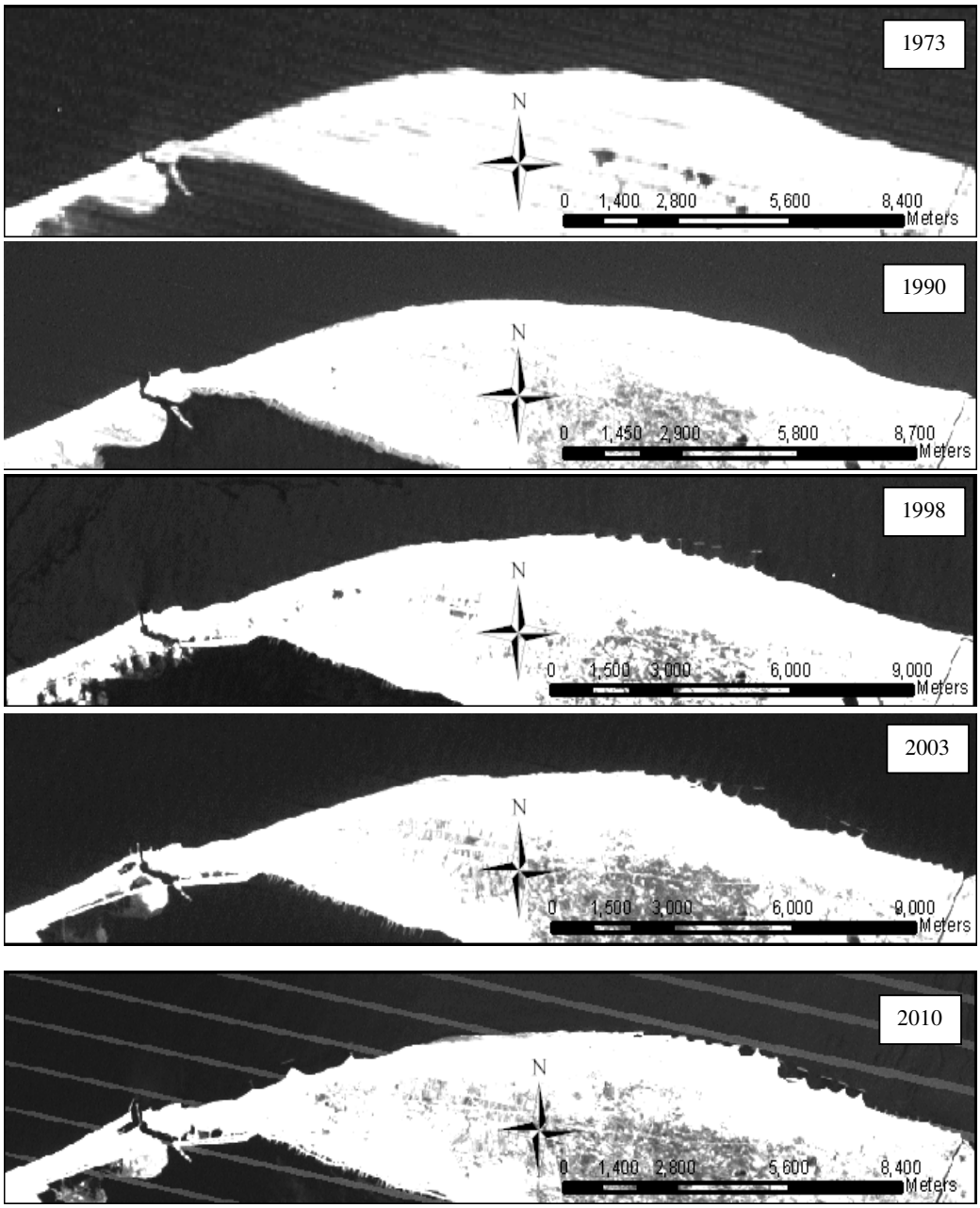

Figure 3.8. Land-sat images around El Burullus promontory.

The erosion decreased further along the promontories far from the River mouths and accretion start to appear. The study site topography and the prevailing wave directions suggested that the sediment mainly is moving toward the east with reversely movement for short period of timeespecially in winter.

The rates of erosion and accretion from 1998 to 2003 and from 2003 to 2010 are illustrated in Figure 3.10. The positive values means accretion and the negative values mean erosion. The change rates show substantial variations from locations to others. The three promontories are the most dynamic parts of the study coast.

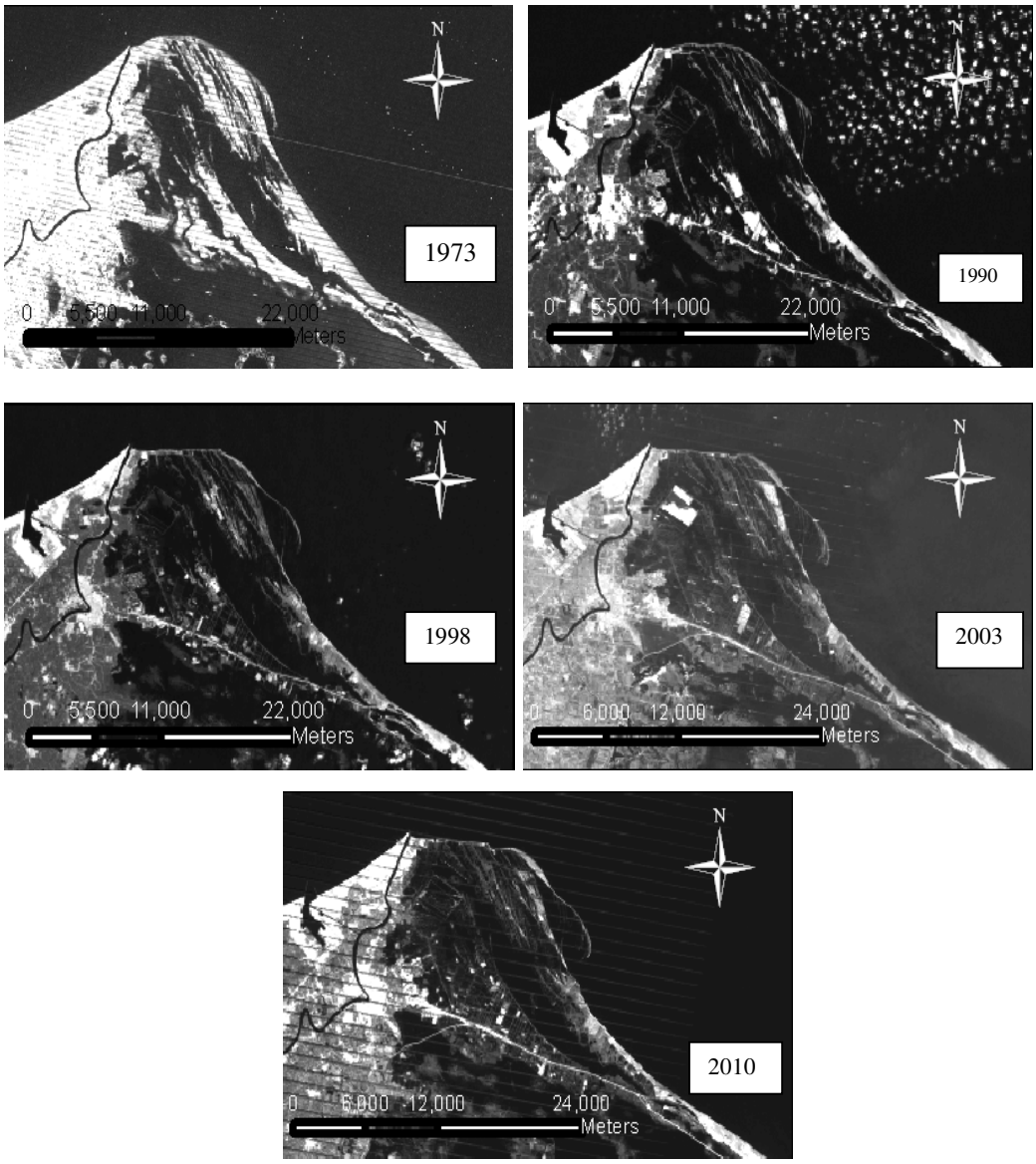

Figure 3.9. Land-sat images around Damietta promontory.

Comparison betweenthe shoreline in 1973 and 2010 around the three promontories are illustrated in Figure 3.11. Severe erosion is experienced within this period around the both river mouths. Around Rosetta mouth more than 10 million m^2 were eroded. While 9 million m^2 from the right side, and 1.6 million from the left side. Accretion were presented clearly, 5 km to the eastward with area exceed 1.8 million m^2. The same pattern of erosion is presented eastward of Damietta mouth with less value. The eroded area reaches 7.7 million m^2. The sand spit advanced 6 km to the south west direction from the 1973 to 2010.

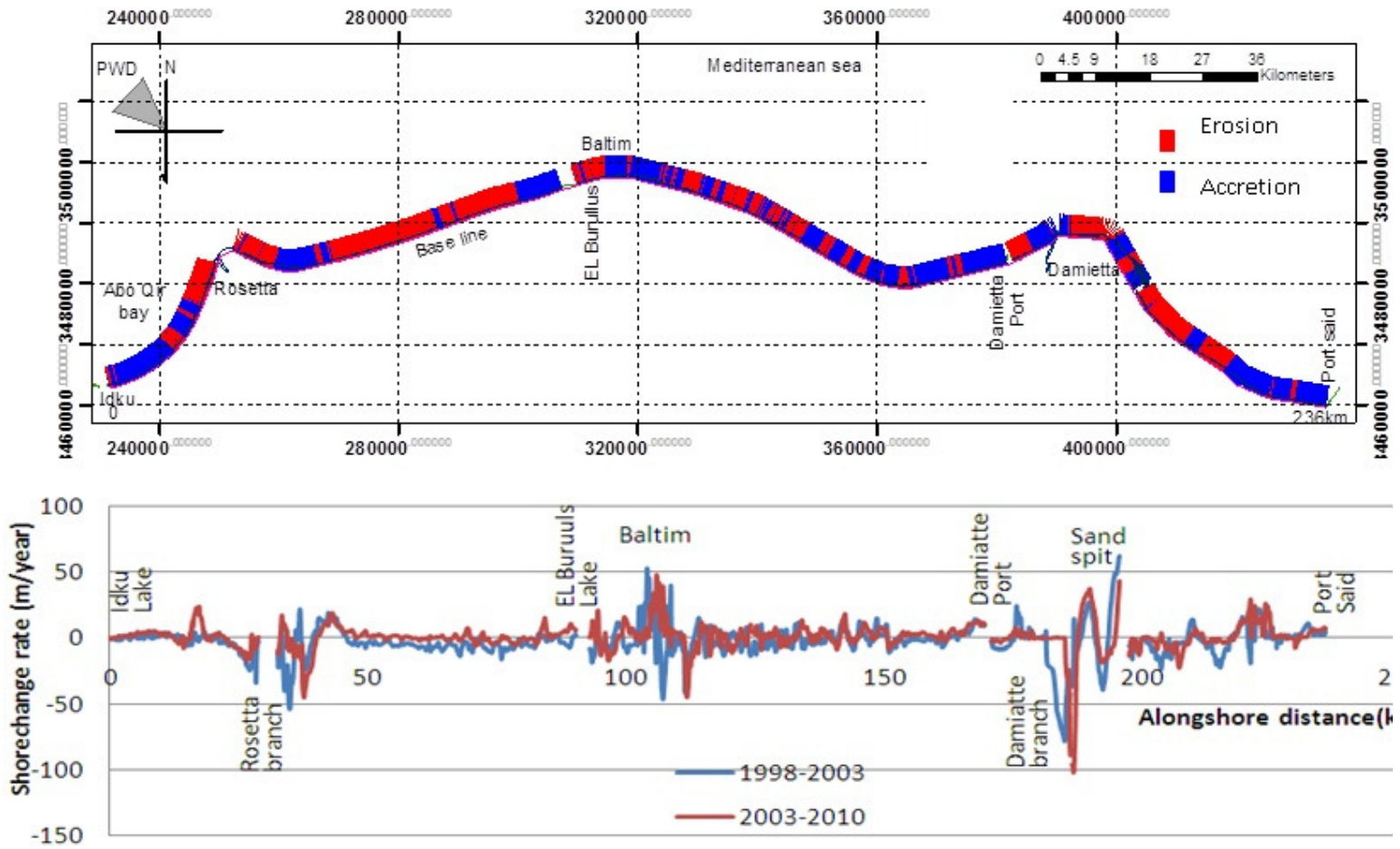

Figure 3.10. A) Study area, accreted and eroded areas and some representative sand samples along the study area. B) Rates of erosion and accretion along the Nile Delta Coast.

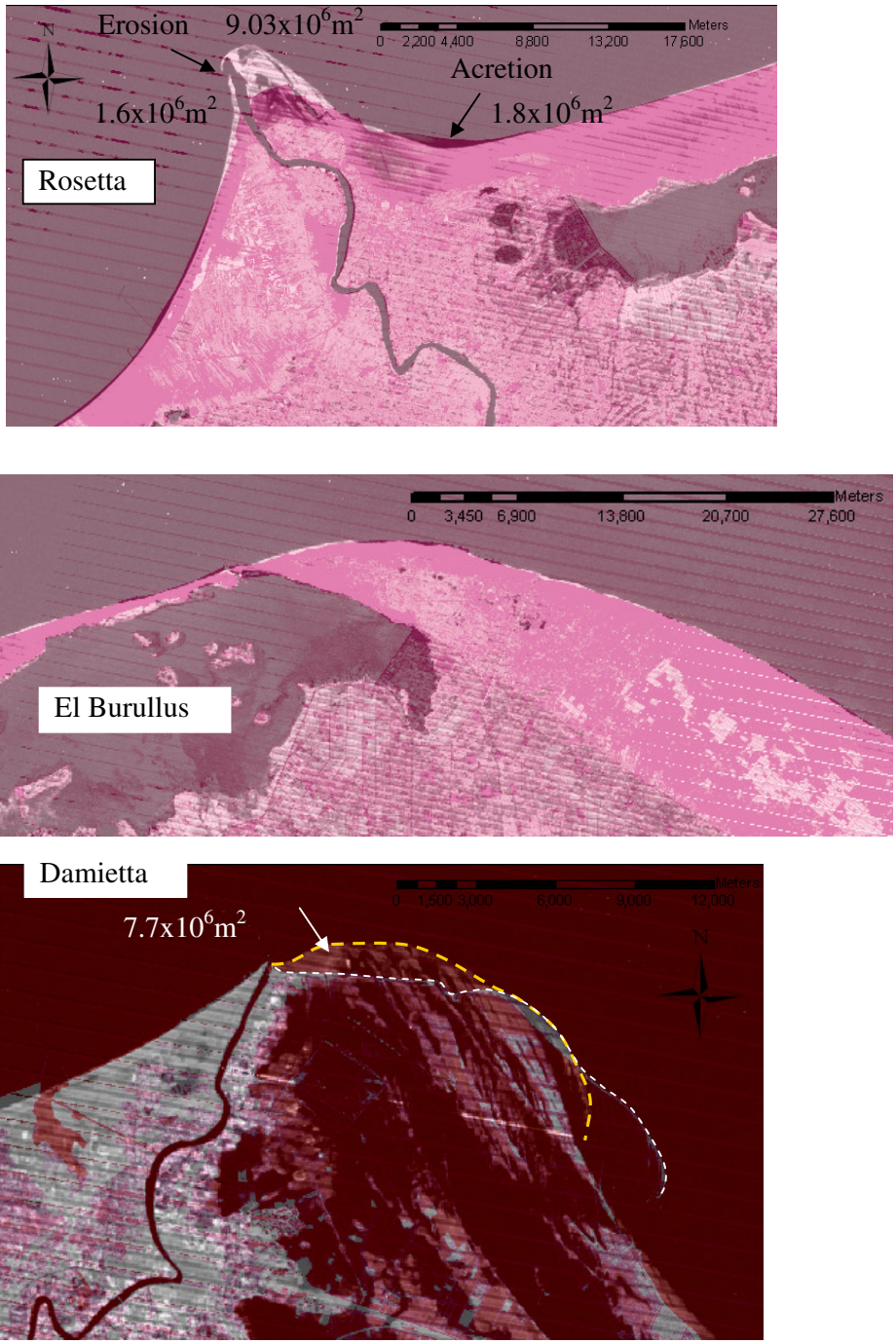

Figure 3.11.Comparison of the morphological changes around the three promontories, Rosetta, El Burullus, and Damietta.

Approximately 46% of the NDC experienced erosion while 52% some accretion.One of the most locally affecting factors on the pattern of erosion and accretion is the placement of shore-protection structures. The patern of the erosion and accretion at different locations along the NDC is strongly affected by placing coastal structures especially around the Rosetta and Damietta river mouths. In the study site the

government is placing different kinds of hard structures.The evolution of the Rosetta and Damietta promontories were examined in more details over 37 years covering the period 1973 to 2010 as discussed in the below sections.

3.4.1 Around Rosetta promontory

3.4.1.1 Image processing

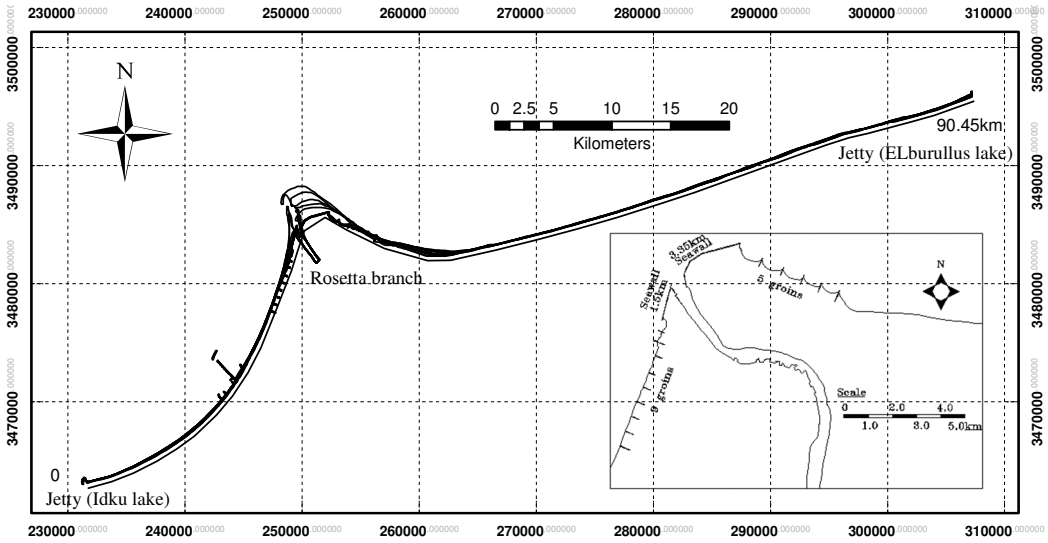

Figure 3.12.Rosetta promontory and coastal structures.

Superimposed shorelines around Rosetta promontory are presented in Figure 3.12. The observed shoreline changes during the focusing period can be classified into three stages: before the construction of the protection works (1973-1990); after construction of the seawalls (1990-2003); and after constructionof the groins (2003-2010). The rates of erosion, and accretion were calculated for these three stages. Figure 3.13 A-C shows the shoreline changes along the study area in these three stages. During the first stage severe erosion took place near the river mouth while the highest rate of erosion around the river mouth of Rosetta promontory was 124m/year. The major reasons for this severe erosion could be due to the blockage of the sediment supply from the river, wave transformation around this area, the sediment size which characterized by fine to very fine sand (D_{50}= 0.15- 0.25 mm), and the sharp shoreline orientation with the predominant wave direction.

Further to the east and the west of the river mouth, erosion gradually decreases and accretion begins to appear around 4 to 5 km away from the river mouth both in the east and westward directions as shown in Figure 3.13 A. The highest rate of accretion reached 19.5 m/year at the eastward side.

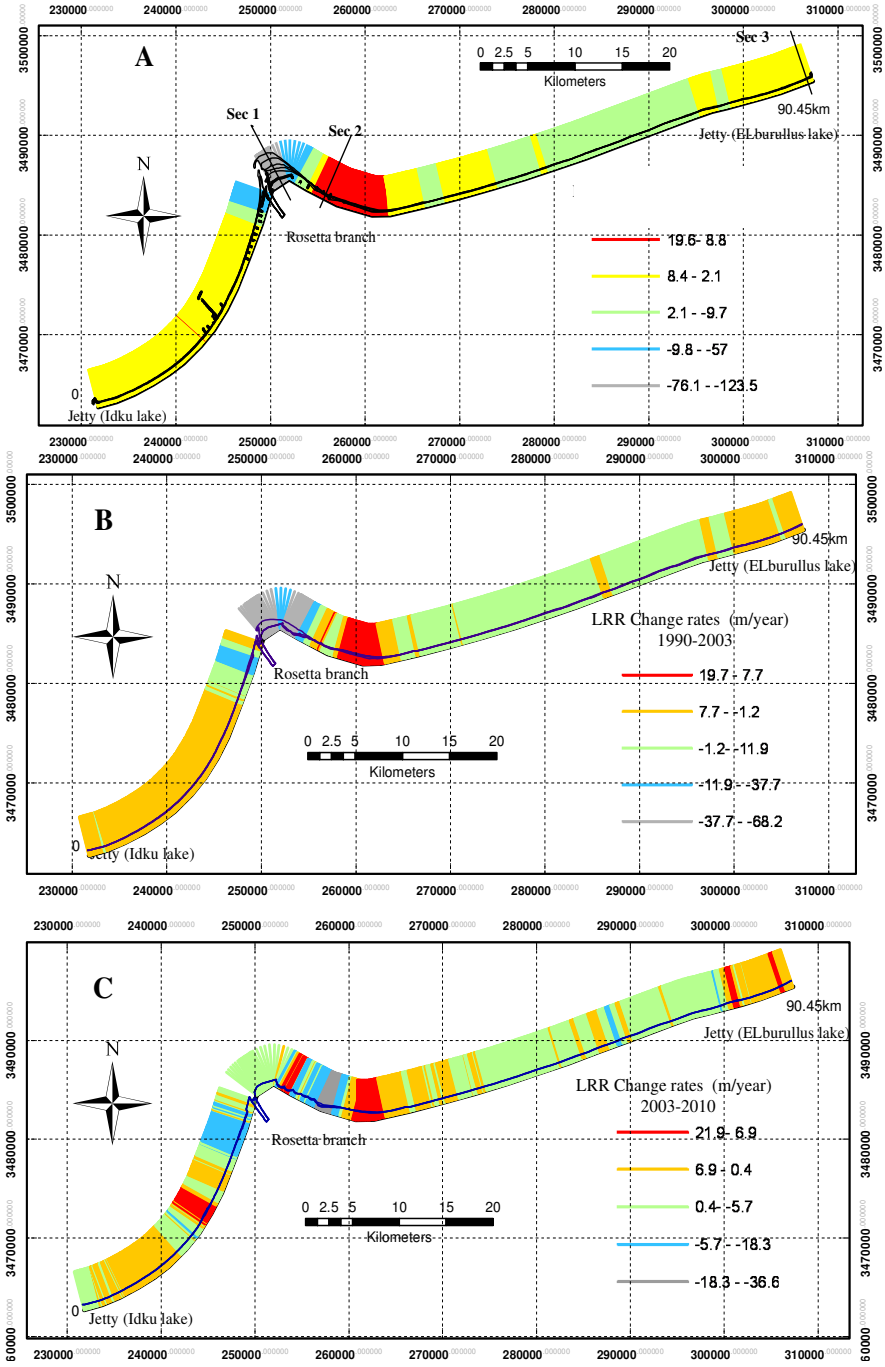

Figure 3.13. Superimposed shoreline positions alongshore Rosetta.

At the western and eastern end of the study area accumulation of the sediment were noticed as the sediment blocked by the jetty of LakeIdku, and the Jetty of lake El Burullus respectively. During the second stage in 1989-1991 two seawalls on the east and west wardswere constructed with a length of 3.35 and 1.5 km respectively near the mouth river.These seawalls covered by concrete blocks of 4 to 7 ton, and designed

for stable scour depth of 8 m, with width varying from 48-70m, and with crest level of 6.75m above the mean sea level (Dewidar and Frihy, 2008).These two seawalls constructed on land so it had no effect on the bathymetry change until 1990 for the western seawall, and until 1995 for the eastern seawall. After 1995, the eastern seawall began to touch the seawater and thus to affect on coastal morphology changes. These coastal structures decreased the shoreline retreat to 70 m/year from 1990 to 2003. In contrast to the protected area, these structures appear to have caused the shoreline retreat further on the downward of the seawalls as shown in Figure 3.13 B. It is worth to mention here that the maintenance and monitoring of the scour rate is important to keep the stability of the seawalls.

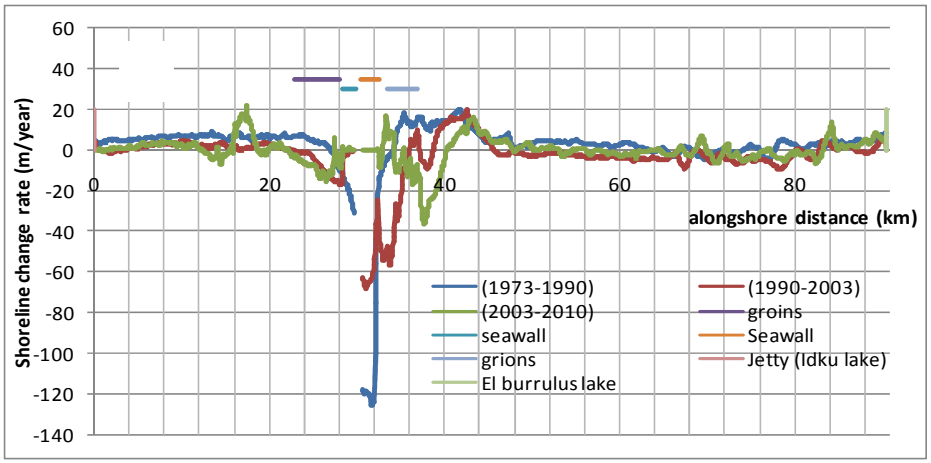

Figure 3.14. Shoreline change rates along the Rosetta promontory.

Based on the measurement of the scour depth, TETRA-TECH (1984) warned that the eastern and western seawalls will be in dangerous state respectively by 2019 and 2027 if the scour depth linearly increases with time in front of these seawalls. It is also noted that the 50-year design lifetime will be terminated by 2041(Dewidar and Frihy, 2008).

During the third stage additional countermeasures were built to mitigate the erosion in the adjacent areas to the seawalls. While five groins were constructed at the east side with length varying from 400 to500 m and horizontal intervals of 800 to 900m in 2003,nine groins were constructed on the west side with length varying from 250-450m and spatial intervals of 450 to 700m starting from 2005. The westward groins were also constructed on land and only the first two groins in 2008 have a short distance in the sea, and now it has length about 150 m in the sea which has an effect

of decreasing the shoreline retreatment adjacent to the seawall. While the eastward groins decreased the retreat of the shoreline, the same erosion problem occurred just adjacent to the last groin with rate equal to 40 m/year as shown in Figure 3.13C. These coastal countermeasures fail to maintain the stability of the shore line over the entire coastal study area while these structures certainly mitigate the local erosion. The shoreline in the eastward coast of Rosetta promontory from X= 42 km up to 80 km has unsteady process alternating from erosion to accretion in the second and third stages as shown inFigure 3.14. Around this part of Nile delta, sediment supply comes from two sources: the River sediment discharge which is very small after construction of Aswan high dam and series of barrages along the river path, and the second source is the eroded area from the tip of Rosetta promontory. The second source also became almost zero after excessive erosion took place and seawalls were constructed. Erosion started to appear adjacent tocountermeasures and this sediment is distributed along the coast.

3.4.1.2 Empirical orthogonal function analysis

The first two modes will be discussed in the paragraphs below as these two modes represent the most variability among the data set, almost more than 98% in our data. The first mode variation of the EOF analysis is linked to the cross-shore movement (Miller and Dean 2007); however the second mode is linked to the longshore sediment processes. Figure 3.15 A&Bpresented the results of the first and second modes respectively, the upper part of each figure shows the temporal eigenfunctiona.C(t).In Figure 3.15 A, e1(x) shows a strong correspondence to the statistical mean of the shoreline data. The first mode exhibitspositive values within the whole considered area with a maximum value nearby Rosetta mouth (at X= 32km) with gradual decrease to the east and the west. This figure implicates that cross-shore variation is more significant near by the river mouth.

The first temporal eigenfunction shows all positive values with a gradual decrease from 1973 to 1998 followed by almost stable trend up to 2010. The effect of constructing the two seawalls at 1989 doesn't appear as it constructed on land and it doesn't have direct contact with the water until1996.

In Figure 3.15 B, e2(x) exhibitspositive and negative values within the whole considered area with maximum value nearby Rosetta mouth. Two nodal points separating the areas of erosion, and accretion are clearly observed on the east, and westward at X=25, 35 km alongshore. These nodal points indicate the importance of the longshore sediment processes. The second temporal eigenfunction $c_2(t)$ shows a positive decreasing trend through the period 1971 to 1990. The temporal eigenfunction changes its sign from positive to negative around 1990, which indicates the change in the longshore transport pattern/direction at that time. A stable and uniform trend was detected from 1998 to 2010.

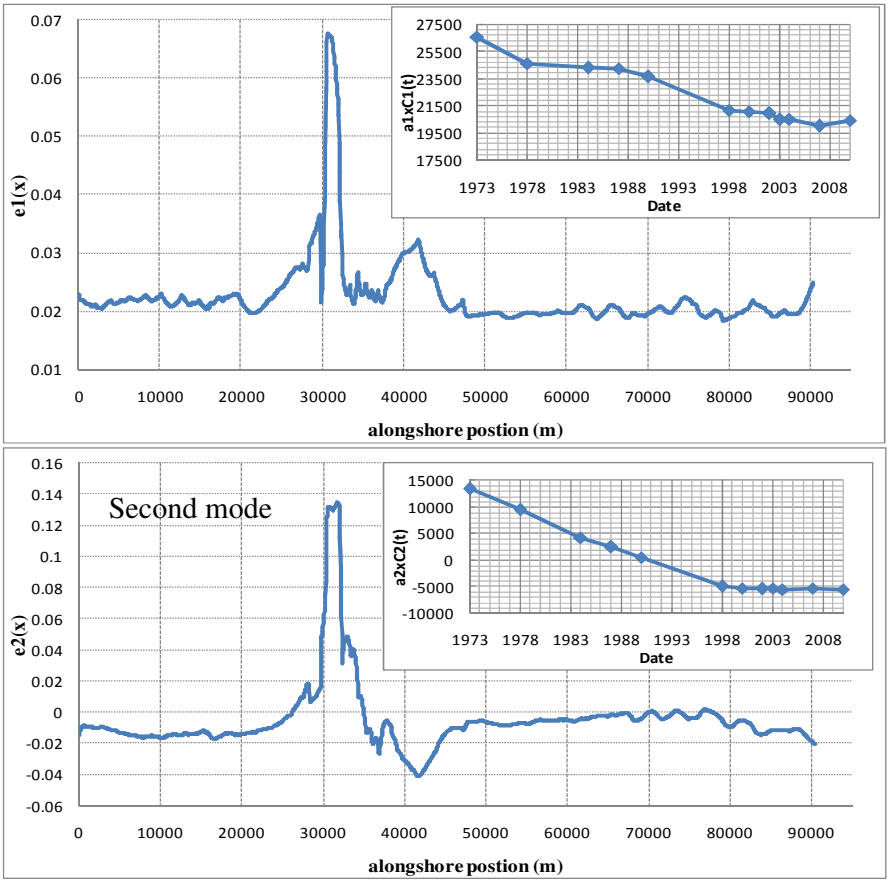

Figure 3.15. First,and second modes results of the Rosetta coast shoreline variationspatial eigenfunction, e1(x),and temporal eigenfunction, c1(t).

Three representative locations , X= 31.15,40, 90.5 km (the east region points) were chosen to show a comparison between original shoreline data, the first, the second mode results and the first plus second mode results derived from the EOF analysis. The locations of these three locations presented in Figure 3.13. The first location

represents eroded area, and the other two locations represent accreted areas. Figure 3.16, represents the results of comparison

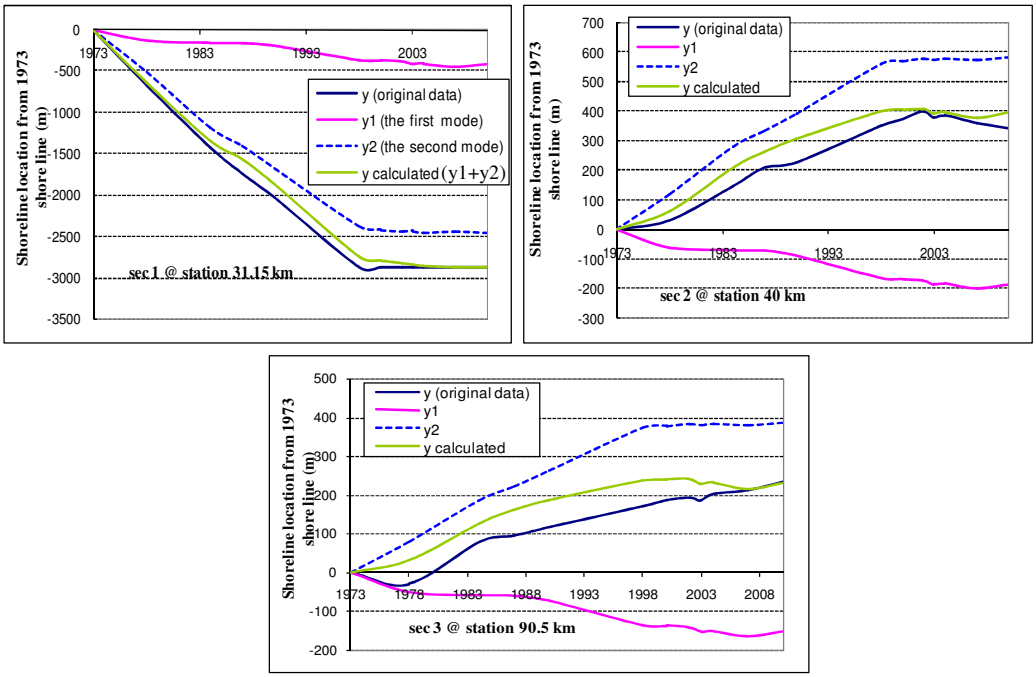

Figure 3.16. Comparison among the original shoreline data, the first mode,second mode results and the first plus second mode results derived from the EOF analysis

It is clearly observed that the first two modes can reproduce the original shoreline variation satisfactorily. The contribution of the first mode is relatively small compared with the second mode as the long shore movement is dominant in case of long term analysis. The small difference between the original data and the first plus second mode results implicates the shoreline variabilitycontributed from the higher order modes of the EOF analysis, e.g., the third, and forth modes.The trend of the shoreline changes shows erosion at the first location followed by stable trend from 1998 to 2010 as a result of seawall constructing. However, it is accretion at the second location between 1973 and 2003. Subsequently, small erosion pattern is observed from 2003 to 2010 as a result of constructing the groins. On the other hand at the third location shoreline data gradually increase all over the study period as the sediment blocked at the jetty of EL BurullusLake.

3.4.2 Around Damietta promontory

3.4.2.1 Image processing

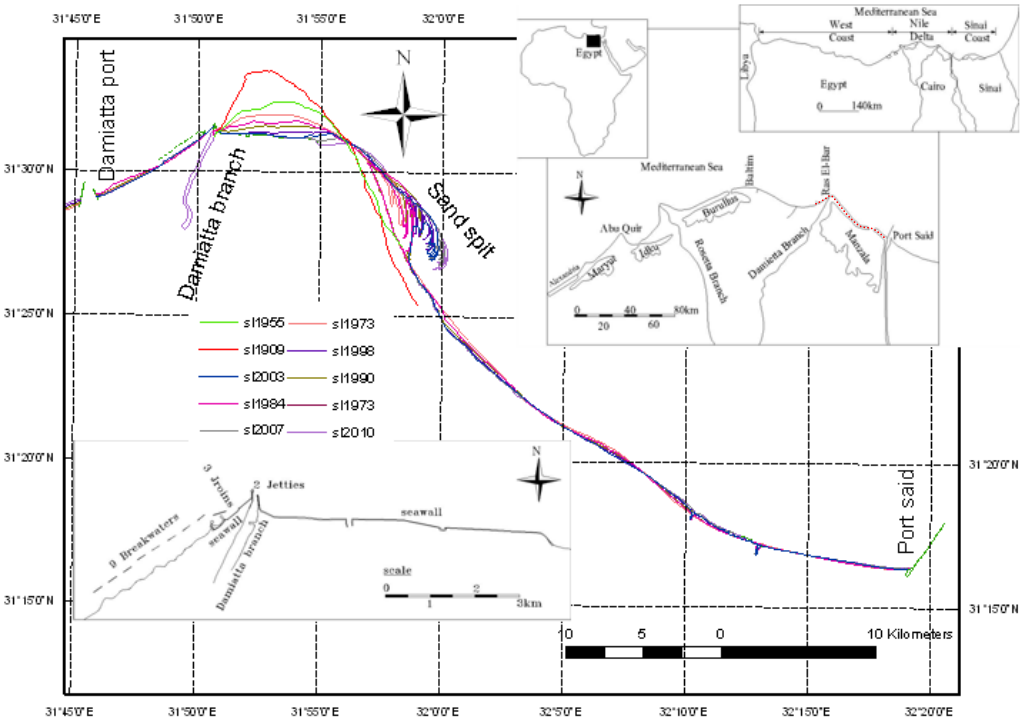

Figure 3.17. Study area, Damietta promontory coastal structures, and dominant longshore sediment transport directions.

The superimposed shorelines, location, and coastal structures around Damietta promontory are presented in Figure 3.17. At this area, comparisons of the extracted shorelines revealed that observed shoreline changes during the focusing period can be classified into two stages, i.e., before and after the construction of the shore protection works in 2003. The rates of erosion and accretion were calculated for these two stages and are presented in Figure 3.18.The study area can be classified into two parts in terms of different behaviors of the shoreline changes: (i) the 10-km-stretch west coast bounded from the east and west by Damietta breakwater and western jetty of Damietta mouth, respectively and (ii) the 55-km-stretch east coast starting from the river mouth to Port Said breakwater.

The Western part has suffered erosion especially after construction of the Damietta port breakwater which blocked the alongshore sediment movement. While the maximum shoreline retreat rate was 4 m/year near Ras EL Bar before 2003, the accretion becomes dominant with maximum rate reaching 10 m/year near the lee-side

of the breakwaters between 2003 and 2010 as shown in Figure 3.18. The erosion rate near Damietta port breakwater is almost the same before and after construction of breakwaters. Sand accumulation is noticed near the eastern breakwater of Damietta port eastern breakwater of Damietta harbor in 1984. This accumulation may be due to the disposal of 5 million cubic meters of sand dredged during the excavation of the port entrance (Frihy et al. 1991).

The eastern part has both accretion and erosions. Historical shorelines data in 1909 and 1955 were detected from(Fanos, 1995) showing that the erosion start from very long time. Within the study period, the erosion is clearly appeared around the river mouth. The highest rate of erosion around the river mouth of Damietta promontory was -50m/year between 1973 and 2003. The seawall was first constructed in 2000 on the land and, since the seawall had no direct contact with the seawater, it had no effect on the bathymetry change until 2003. After 2003, the eastern seawall began to touch the seawater and thus to affect on the coastal morphology changes. This seawall terminated the shoreline retreat. In contrast to the protected area, this seawall appears to have caused the shoreline retreat further on the downward of the seawall with retreat rate of -100m/year as shown in Figure 3.18. During this period, sand spit was developed by the significant sand supply from the severely eroded area near the river mouth. This sand spit started to appear in a certain year between 1955 and 1972 as shown in Figure 3.18. The sand spit developed next to this eroded area has also shown significant deformation. The spit was extended eastward with distance of 1.5, 1.9, 2.5, 3, and 3.8 km measured from the eastern end of the spit in 1973 to the years, 1984,1990,1998,2003 and 2010, respectively. Along with the extension of the sand spit, the coastline behind the extended tip of the sand spit was eroded. The sand spit appears to act as a breakwater and the erosion is shifted to the east as the sand spit is extended. From 1974 to 2003, the maximum erosion rate behind the sand spit reached -20m/year at X=29,800m. While this erosion was terminated at the same location, nearly the same erosion rate was observed at X= 35,900m between 2003 and 2010. Further to the east, many nodal points, where accretion or erosion patterns switch to each other, are found between the spit and Port Said breakwater, as seen in Figure 3.19.

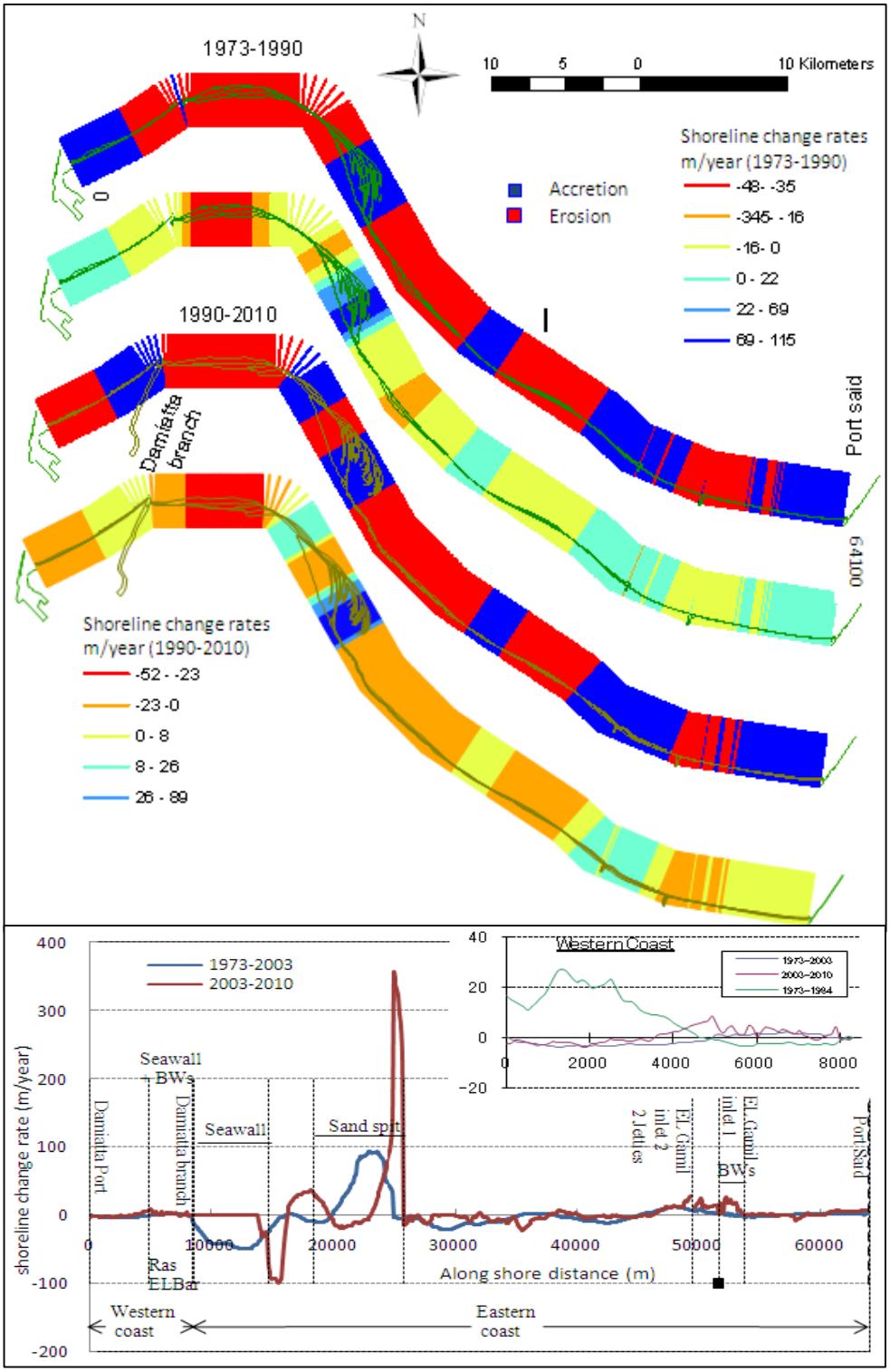

Figure 3.18. Superimposed shoreline positions alongshore Damietta promontory and the rates of erosion and accretion during the study period.

Local accretion is accumulated near the jetties of EL Gamil inlet 2 which constructed in 1972 and the six detached breakwaters constructed in 1996 on the east side of EL

Gamil inlet 1 while the maximum rate of accretion reaches 28m/year, 23 m/year near the jetties and breakwaters, respectively, from 2003 to 2010.

The end point of the study area is Port Said breakwater. This breakwater acts as a huge barrier against the incident waves and blocked the eastward sediment movement and, as a result, the area of Port Said has experienced accretion all the time with maximum rate of 6m/year.

3.4.2.2 Empirical orthogonal function analysis

Since the shoreline around the center of the spit was relatively stable, this analysis focused on the shoreline change around the east end of the spit. As seen in Figure 3.19.The shoreline at the east end of the spit curves toward the land. This study took x and y in the south-west and south-east directions, respectively. The spatial eigenfunctions are the spatial structure of the major factors in different order that account for spatial variation of y whereas the temporal eigenfunctions are the principal components that show how the amplitude of each spatial eigenfunctions vary with time. Finally, a_k is the normalizing factordetermined as a function of λ_k, eigenvalues associated with the$k$-th eigenfunction.

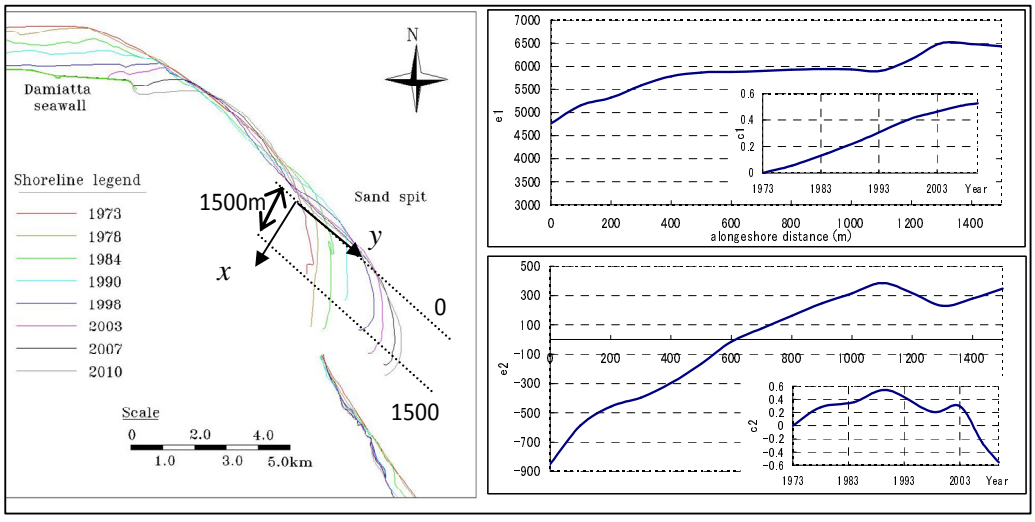

Figure 3.19. Plan view of the sand spit and the first and second modes of spatial and temporal eigenfunctions, e(x) and c(t), for the sand spit variation.

The results of EOF analysis at the study area revealed that the first two modes represent the 97% of the observed shoreline changes. The first mode represents the

south-eastward extension of the entire east end of the spit whereas the second mode represents the shoreline changes associated with the local balance of the longshore sediment movement.

Figure 3.19 presents the spatial and temporal eigenfunctions of the first and second modes, respectively. The first mode exhibitspositive values with a maximum value observed around x=1300m, the east-end of the spit.The first temporal eignfunction, e_1, shows gradual increase with time and this feature indicates that the entire east-end of the spit is kept propagating toward south-west with smaller rate after 1998. On the other hand, $e_2$exhibitspositive and negative values. One nodal point are clearly observed at x=600m. This nodal point indicates the change in the angle of the shoreline. The second temporal eigenfunction, c_2, shows a positive mild increasing trend through the period 1973 to 1990 then sharp decrease until 2010. The temporal eigenfunction changes its sign from positive to negative around 2006, which may indicate that incident wave conditions has been changed with extension of the sand spit.

Chapter4 Thermo-Luminescence and Sediment characteristics

4.1 General

The physical sediment characteristics affect the shoreline and the morphological changes. The size of the sediment grains influences the way how a beach behaves. Sediment transport depends on sediment properties, characteristics of the sediment bed, and properties of the wave and currents. The sediment characteristics are important factors among the previously mentioned factors in describing how the sediment is transported. Also the sediment characteristics could be used as an indicator of the sediment transport pattern and to distinguish between the eroded and accreted areas. Primary properties for specifications of the sediment characteristics are types, size distributions, density, settling velocity and colors of the grains.

Accurate and reliable measurements of sediment transport are necessary for both developing efficient countermeasures against coastal-erosion problems and proposing better predictive tools in coastal-engineering applications. In a case study of the nearshore sediment processes, identification of sediment sources, sinks, transport paths, and historical evolution are of crucial importance, Liu et al. (2009). While there are various techniques to detect and evaluate the sediment transport and differentiate between the eroded and accreted areas, all of these techniques have both advantages and disadvantages. i.e., 1) Tracer techniques (fluorescent, dye-marked sand or color sand) are ones of such techniques to investigate the sediment transport characteristics. Zed and Shereet (2005) studied the sediment movement around the Rosetta mouth through the analysis of fluorescent sand tracers, Fluorescent dyed grains analysis were performed at the western side of Rosetta branch and along the spit of the eastern side during 2003. This technique is good for relatively small areas and it may not work well in relatively large scale areas. One of primary disadvantages of this technique is that, compared to the natural sand, the injected sand may have different chemical and physical properties (grain size, distribution, shape, specific density, and mineral composition) and this difference may cause unreliable results. 2) The usage of large scale sediment traps (groins and inlets), Frihy et al. (1991) determined the patterns of nearshore sediment transport along the Nile Delta through studying the response of the beaches near the coastal structures. This approach is passive and could be used with short and long period and it could be used for large areas but it needs to install the traps. 3) Study of sediment physical and chemical

features (sand size analysis and mineral or magnetism decomposition) could be used to discriminate the erosion and accretion areas. Frihy and Komar, (1993) investigate the long term shoreline changes along the Nile Delta and correlated it with the alongshore distributions of consisting ratios of heavy minerals and the sediment grain sizes. They found that the eroded areas are associated with finer-grained beach sands with more heavy minerals and the greater the rate of erosion the beach tends to have the finer sand grains and the more content of heavy minerals. Inversely, the areas of shoreline accretion are characterized by coarser sands that are depleted in heavy minerals, and richer in quartz-feldspar light minerals. 4) El-Gamal, (2012) implement a new indicator to differentiate between the eroding and accreting coast through the analysis of the dissolved inorganic silicate and suspended particulate material concentrations in seawater near Rosetta mouth and El Gamil inlet. He concluded that relatively small values of the dissolved inorganic silicate and suspended particulate material concentrations were contributed to the coastal erosional area (Rashid) and relatively higher values to the coastal accretionary area (El-Gamil inlet) 5) Remote sensing techniques as explained in the pervious chapter .

The main objectives of this part of the study are as follows. The first objective is to determine the characteristics of the sediment (sand size, color, and mineral decomposition) along the entire study area which could be used in the sediment transport investigation and erosion and accretion discrimination. The characteristics of the sediment along the study area are an important factor to be used for the numerical simulation of the shoreline change as explained in the last chapter of this thesis. The second objective is to use the Thermoluminescence (TL) signal in littoral zone feldspar to study the sediment transport in the nearshore zone. The TL signal of the littoral samples along the fluvial system of the 250 km Nile delta was analyzed in order to investigate the relation between the sample positions and longshore drift. This study confirms the validity of this useful technique to be used in studies of sediment transport along the Nile Delta Coast (different environmental conditions than other areas of the pervious studies).

4.2 Literature review of the Thermo-Luminescence (TL)

TL is merely one of a large family of luminescence phenomena. Figure 4.1, presents the family tree of the luminescence. When radiation is incident on a material some of its energy may be absorbed and re-emitted as light of a longer wavelength (Stoke's Law). This is the process of luminescence. The wave length of the emitted light is characteristic of the

luminescent substance and not of the incident radiation (Mckeever, 1983).

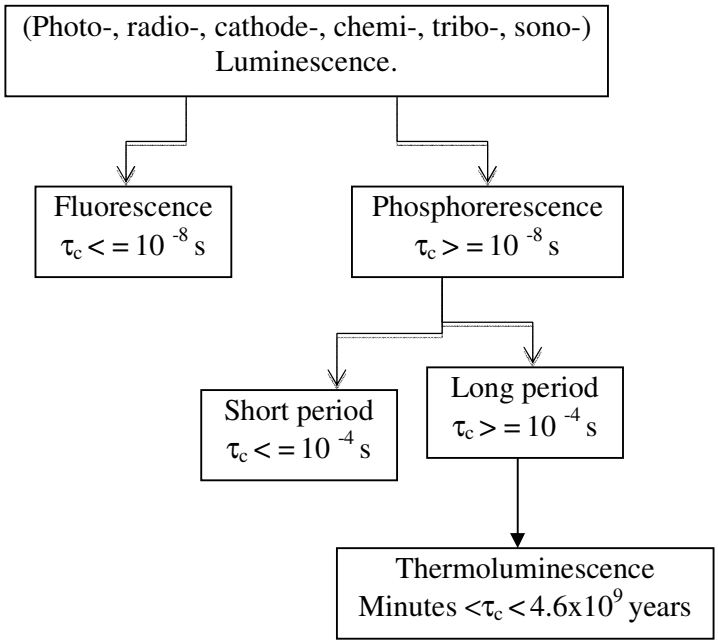

Figure 4.1. the family tree of luminescence phenomena (Mckeever, 1983).

τ_c : The emission of light characteristic time after the absorption of the radiation

Radioactivity (potassium (^{40}K), thorium (^{232}Th), uranium (^{238}U), and rubidium, (^{87}Ru)) and cosmic radiation are the main sources of Radiation. Figure 4.2, is a schematic showing the both sources of radiation upon the buried materials. All buried materials are exposed to a constant flux of ionising radiation. When crystalline materials as feldspar or quartz are exposed to ionising radiation, a redistribution of electrical charge takes place within the crystal. Some electrons finds its way back to the original state within a short period; other electrons are trapped, or arrested, for extended periods of time by localized defects, or imperfections. If the defect is large enough electrons can be held for long periods of geological time. These trapped electrons could be released after exposing to an external stimulation. In case the external stimulation is light it is called Optical Stimulate Luminescence (OSL) and in case of heat it is called Thermo luminescence (TL). The graph of the amount of light emitted during the TL process as a function of the sample temperature is known as a TL glow curve. (Mckeever, 1983) figured out that there are three essential ingredients are necessary for the production of TL can be deduced. Firstly, the material must be an insulator or a semiconductor (metals do not exhibit luminescent properties). Secondly, the material must have at some time absorbed energy during exposure to ionising radiation.

Thirdly, the luminescence emission is triggered by heating the material. The principle of luminescence methods has been described in detail in (Aitken, 1998). He defines the TL as the emission of light from a semiconductor or an insulator when it is heated, due to the previous absorption of energy from irradiation. Figure 4.3, shows the level diagram describing the ionization, storage, and evection process**.**

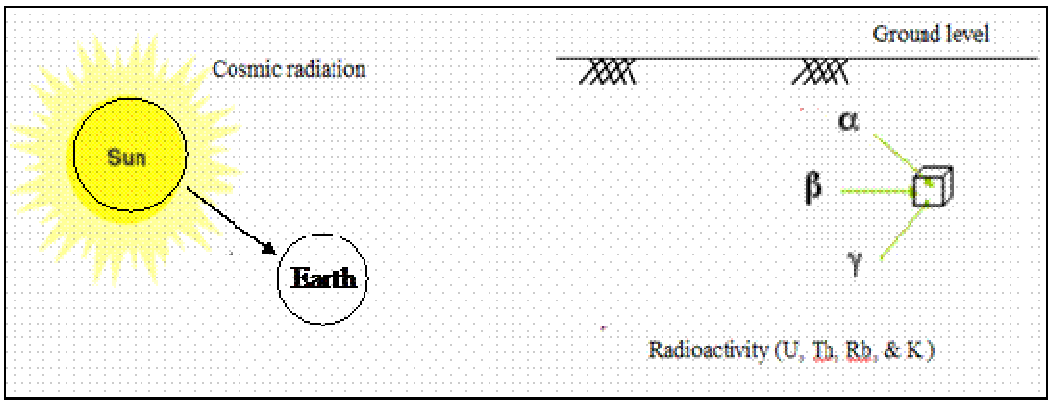

Figure 4.2 schematic for the main sources of the radiation.

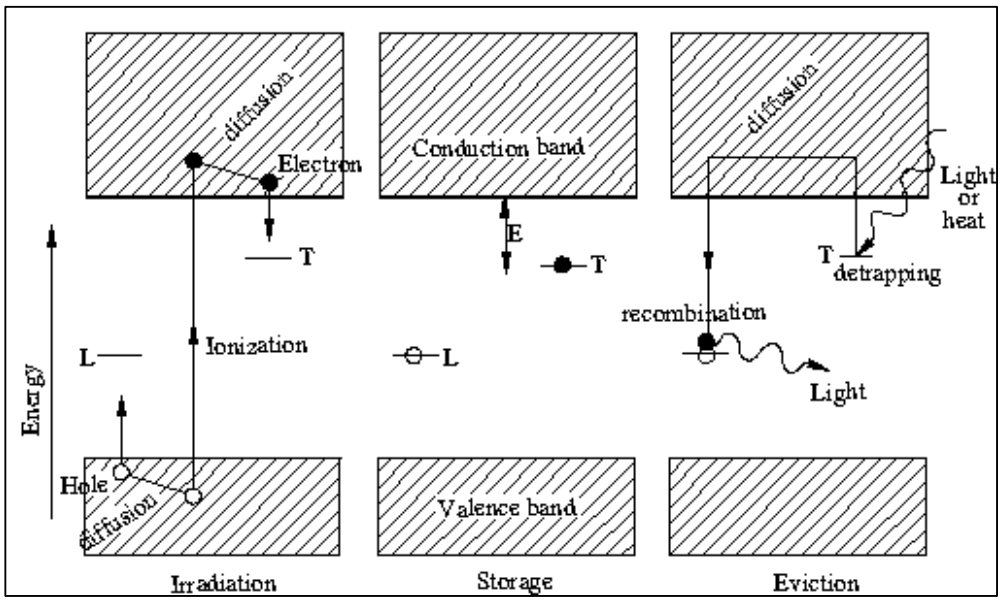

Figure 4.3. Energy level representation of TL process (Aitken, 1998).

i) Ionization due to the exposure of the crystal to the flux of nuclear radiation, with trapping of electrons and holes at defects, T and L respectively. ii) Storage during antiquity. iii) By shinning light or heat, electrons are evicted from traps and some of these reaches luminescence center. The electrons may recombine at non luminescence center, be recaptures by a trap of other type. For deeper traps, higher temperature is necessary (Aitken, 1998). If the crystal is then cooled and re-heated it does not re-emit light, because the energy excess

which produced the first emission has now been released from the crystal. The amount of light emitted is proportional to the number of trapped electrons, which in turn, is related to the time lapsed since the sediment was last exposed to light (Aitken, 1998). Since the intensity of TL is dependent on how long such crystalline materials absorbed the radiation energy without being exposed to the sun light, TL intensities of sand grains are known to decrease when they are transported along the shoreline under the sunlight, Keizars et al. (2008). The longer the burial time, the greater the number of trapped electrons is. In general, natural erosion and transportation of sedimentary particles from the upstream river watershed to the downstream area, to the river mouth, and finally, to the nearshore region, are accompanied by solar radiation exposure. Such sand movement reduces the particle luminescence signals by depopulating the trapped electronic charges from the lattice defects where they were stored during burial. This illustrates the possible use of TL/OSL as a tool for describing the temporal and spatial sediment-movement processes, Liu et al. (2009). Figure 4.4, shows a schematic diagram to illustrate the grain TL signal accumulation/release process.

TL is a geochronometric technique utilized in a variety of applied sciences. Recently it is used in the coastal studies. Rink, (1999, and 2003) suggested the use of the TL properties of quartz and feldspar grains as a transport indicator in the study of various coastal depositional processes. Rink and Pieper, (2001) analyzed the residual TL in quartz collected from the surface and the subsurface of the beach at the S1. Joseph Peninsula State Park. Samples to represent a hurricane deposit and a littoral drift deposits. A higher residual signal was found in samples from the underwater zone than in those from the beach Surface. Rink, (2003) investigated the variation in the natural residual TL of quartz from samples collected at the southeastern Mediterranean Sea. The sediment transport direction was derived from the variation of the TL signals along the coast.

Forrest, (2003) used OSL to date quartz samples collected from dune ridges on the St. Joseph Peninsula, to test the feasibility of dating quartz from heavy mineral layers as a solution to the problems associated with the low luminescence signal inherent to young samples and to use the natural residual thermoluminescence (NRTL) signal in littoral zone quartz to study sediment transport in the nearshore zone. Shirai and Omura, (2007) proposed the use of the ratio of bleached grains in a sample (bleaching percentage) which would be able to offer significant information on processes of grain transport.

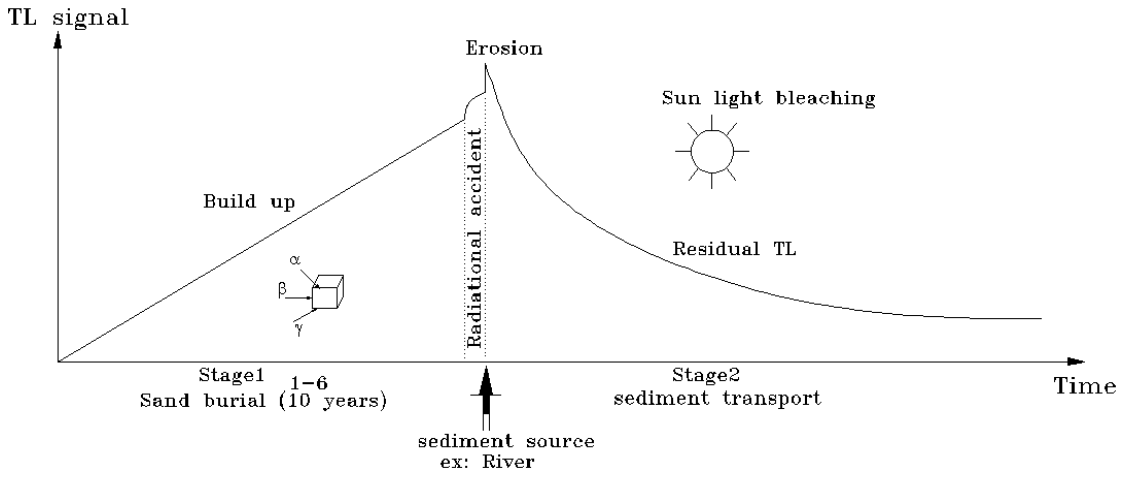

Figure 4.4. Schematic diagram on temporal variation of grain TL (modified after Liu et al. 2009).

This method was applied on southeast off the Kii Peninsula, central Japan. Liu et al. (2010) investigated the sediment movement along the Tenryu–Enshunada fluvial system, Japan based on Feldspar TL properties. Tajima et al. (2011) detect the nearshore sedimentary characteristics along the West Coast of Sri Lanka Based on the Analysis of Satellite Images and Feldspar TL. Liu et al. (2011) monitor the nearshore sediment movement and mixing process with nourished sands along the Miyazaki coast, Japan based on the feldspar luminescence measurement, including both TL and OSL. Nourished sand presents larger TL/OSL properties than the natural beach sand.

4.3 Methods

4.3.1 Sample collection

Field survey was conducted in February 2011. Samples were collected from several locations along the study area along the Nile Delta Coast from the both branches of the River, Sand dunes, and along the shoreline. The acquisition date and coordinates of samples are prescribed in Annex A-1. The detailed locations of the samples in Google Earth images are illustrated in annex A-2 “Sand samples locations on Google Earth images”. In order to identify the sand source, riverbed surface samples (about 30 km upstream of the river mouth) upstream and down stream of Delta barrages were extracted along the two braches of the Nile River. The locations of the sand samples are presented in Figure 4.5.

Samples were collected from the layer at 5-10 cm below the ground surface in the inter-tidal zone. Littoral samples were collected along the entire length of the Nile delta coast from Idku Lake up to Port Said. Sample collections were carried out with a spatial interval of several kilometers. Sample intervals varied from 3km to 25 km. All littoral samples were collected during three days. Fifty-four littoral samples and four samples from Rosetta, three samples from Damietta, and two samples from the sand dunes. The sample was placed in an opaque Ziploc bag and transferred to a large black dark bag. The tools and the steps used in the sampling are prescribed in Figure 4.6. These samples were used in both the analysis of the sediment characteristics and TL test.

4.3.2 Sample preparations

Figure 4.7, presents the steps followed for samples preparation. After field collection, all samples were sent to the Coastal Engineering Lab –Tokyo University. All samples kept to be dried for several days. Pretreatments were conducted in a dark room to avoid the exposure of samples to the light which leads to underestimating the luminescence signals. Taking into account that luminescence signals are less sensitive to low energy photons (red to green) than to higher energy ones (blue to ultraviolet), laboratory preparation was carried out under subdued, orange light (600 nm), which had little influence on the TL signals, (Liu, 2010). Here we followed the same method as, Liu et al. (2009), A portion of each sample was taken and water washed. The samples were sieved to extract the 180–300 μm grain fractions then subsequently treated with 15% H_2O_2 and 18% HCL to remove the organic material and carbonates. The lithium–heteropolytungstate heavy liquid was then used to isolate the feldspar (density < 2.58 g/cm3) using centrifugal machine. To avoid the thermal transfer the drying was under the room temperature.

Figure 4.5. Research area and sampling locations; The green color represents the sampling location from the river, the magenta color represents the sand dunes , and the yellow color represent the littoral samples .

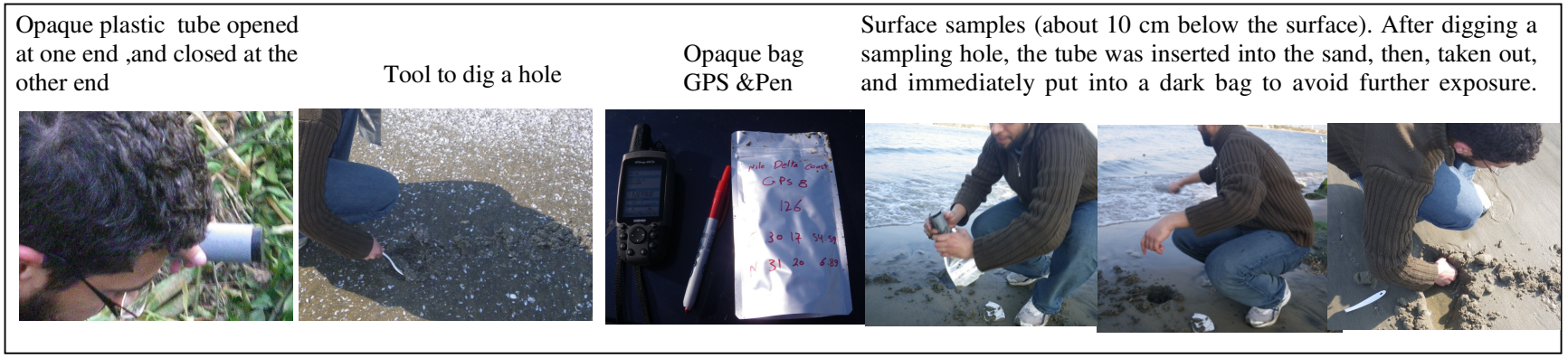

Figure 4.6. The tools and steps to take the sample.

4.3.3 Thermo luminescence measurements

TL measurements were performed using an automated Risϕ–48 TL/OSL reader with an internal $^{90}Sr/^{90}Y$ beta irradiation source. A Corning 7-59 filter was used as a blue/violet filter and a Schott BG-39 filter was used to remove red fluorescence and to restrict the blue range detected. Annex A-3 includes photo of the TL reader. Four monolayer aliquots of each sample were prepared and mounted on a 10 mm diameter stainless steel discus by mask (silicon). The tools and the steps of preparing the discus are illustrated in Figure 4.8.

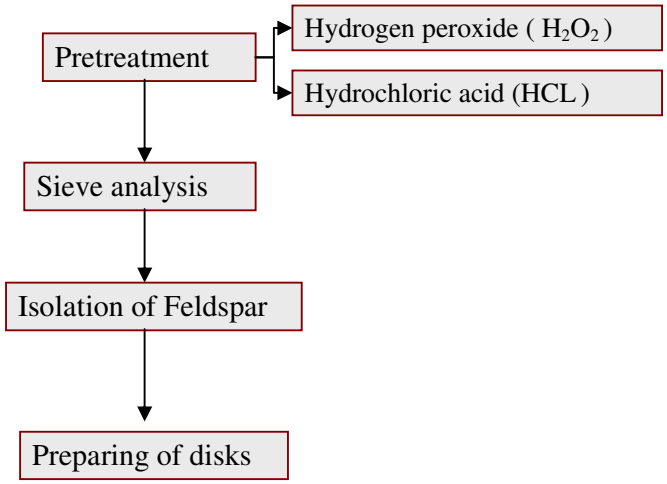

Figure 4.7. Flow chart of the preparation sequence.

Description of sequence and protocols

Each aliquot was measured following the protocol proposed by, Liu et al. (2009) as outlined in Figure 4.9 except in the preheating temperature. A series of pretests was carried out on sample 134 to determine the most appropriate preheating temperature. The preheating was done to remove the unstable luminescence signal (Duller and Augustinus, 1997). Figure 4.10, shows a comparison between the TL signal after given artificial dose for the two cases, with and without preheat. It is clear that for the case with out preheating, many shallow traps are filled and the TL peak is experienced in a low temperature around 100-110o. Such low-temperature TL peak does not exist in natural TL signals because of the long storage times in the field. Shallow-trap–related low-temperature TL peaks are unstable, and their signals gradually decay with time, Liu et al. (2009). Forrest, (2003) found that as the heating rate increased the

peak intensity lowered and the peak itself shifted to higher temperatures until, at a rate of 15^{o} C/sec the peak was no longer visible. Also the natural TL obtained without using preheat had a higher standard deviation than when preheat was used.

Duller and Augustinus, (1997) adopted the preheating temperature to be 220° C at a rate of 10^{o} C/sec and held at this temperature for 10 s. Liu et al. (2009) suggested the preheating to be 180^{o} C/sec for 10 sec. Here, the natural TL measurement was carried out after preheat of 200^{o} C for 10 sec to remove the unstable TL signals. This preheat temperature were acquired from several pretest. Figure 4.11, presents the TL intensity for different preheat temperature (plateau test).

After measuring the natural TL, the sample is heated to 450^{o} for 30 sec to remove any residual signals. Since the aliquots are different in mass, the TL response of each aliquot was measured after receiving an artificial test dose stimulation of 60 s (10.8 Gy beta dose) and used in normalization of the natural signal. The TL is recorded while the sample was heated from the preheating temperature to a maximum temperature of 500° C at a ramp rate of 5° C/s.

The back ground is subtracted from the TL results. All measurements were conducted under nitrogen-rich conditions. Two normalized techniques were used. The first; both the natural and the artificial dose curves were integrated between 200° C and 450° C. In the second method, the natural curves were integrated between 350 °c and 450° C and the artificial dose curves were integrated between 250° C and 350° C. The average normalized feldspar TL signal was acquired by averaging the normalized TL signal of no of aliquots depending on the standard deviation of each aliquot.

4.4 Sediment characteristics

4.4.1 Methods

Using the same samples, sand characteristics were further investigated. The grain size distribution was measured using the laser diffraction particle size distribution measuring apparatus. The color of sand grains was identified by naked eyes and the mineral compositions based on color were interpreted using the automated analysis of images captured by a digital microscope.

Figure 4.8. The tools and the steps of preparing the samples.

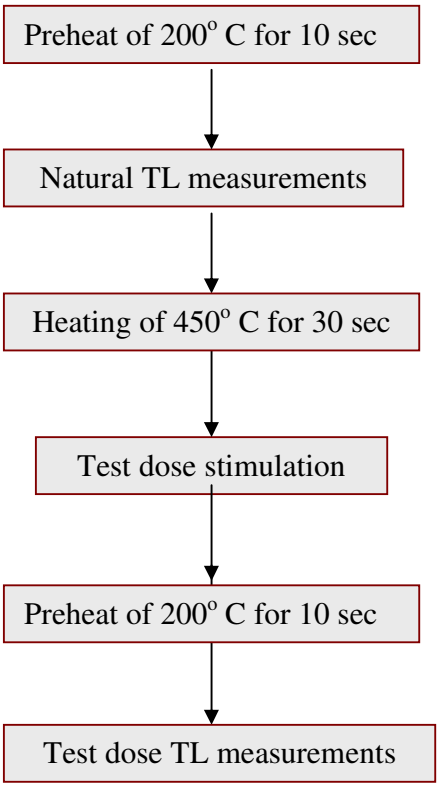

Figure 4.9. TL Test protocol.

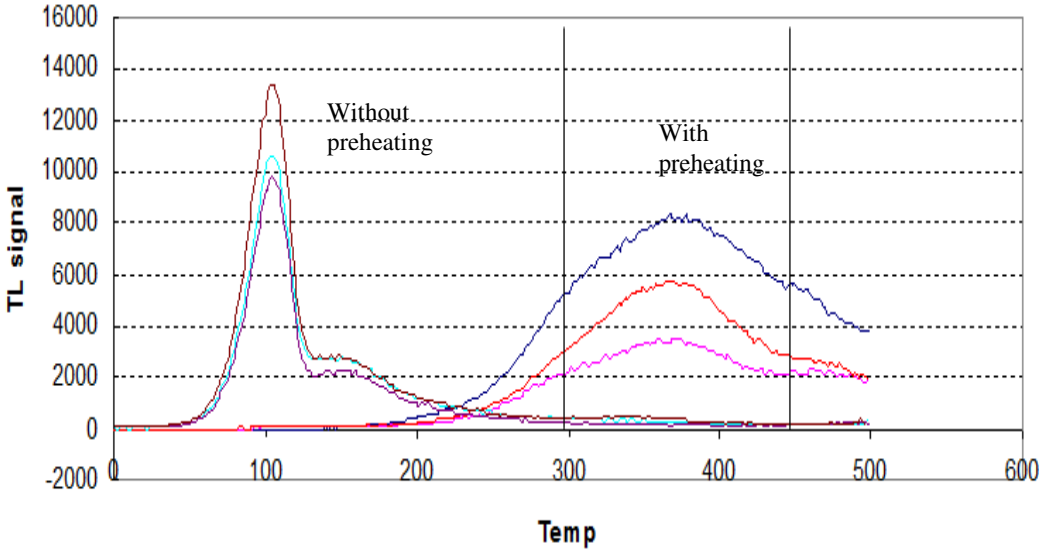

Figure 4.10. Comparison between the TL signal with, and without preheating.

4.1.2 Sediment size

Traditional methods of determining grain sizes are either sieving (wet or dry) analysis or the settling tube techniques based on Stoke's law. Here, the laser diffraction particle size distribution measuring apparatus (SALD-3100) was used to define the

grain size distribution. Annex A-3 includes photo of the measuring apparatus. This apparatus has the ability to cover wide rage of sediment from 0.05 to 3000 µm using a single measurement principle, a single optical system, and a single light source.

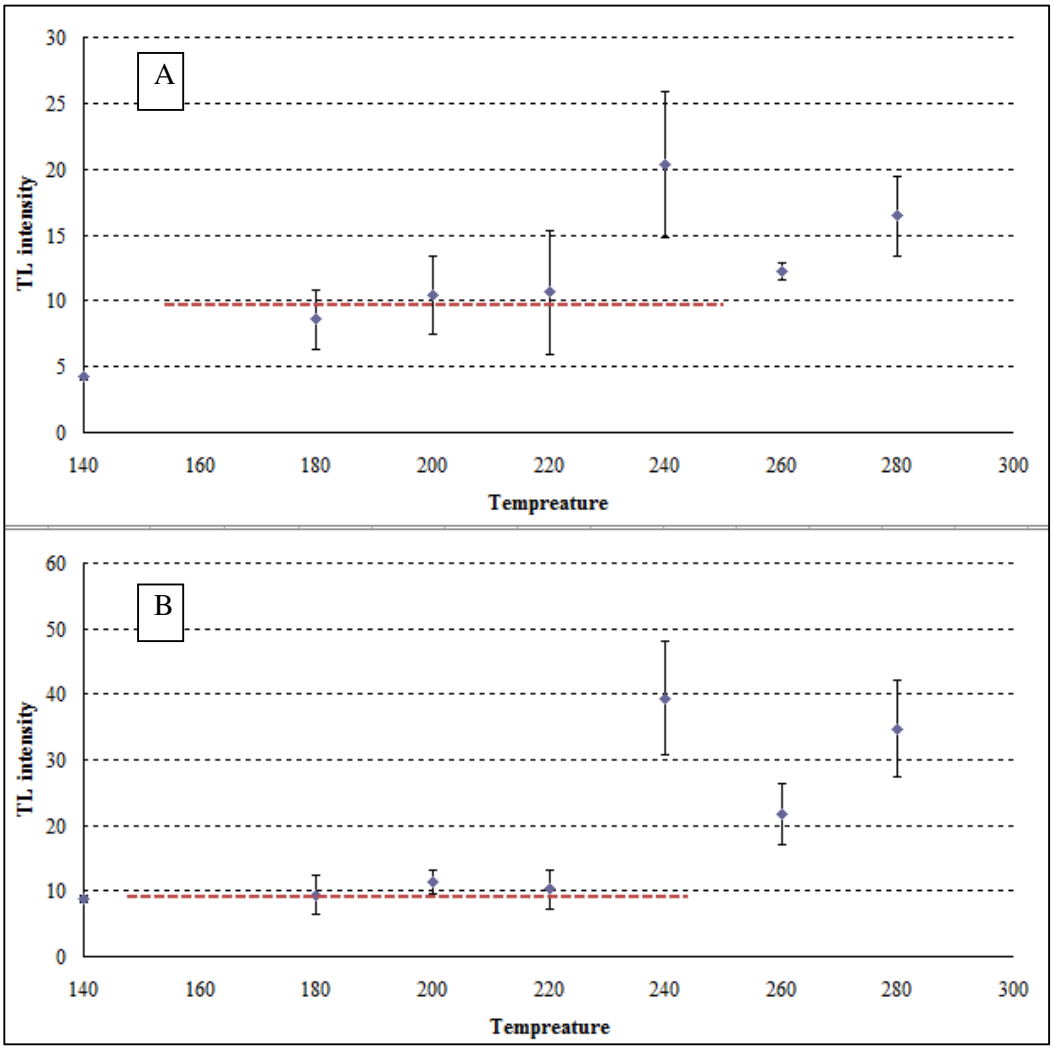

Figure 4.11. Plateau test, the normalized TL for different values of preheating temperature, artificial dose of 6 sec (1.08 Gy). A) The natural curves were integrated between 350 °C and 450° C and the artificial dose curves were integrated between 250 °C and 350° C. B) The natural and artificial curves were integrated between the preheating temperature up to 450° C.

4.1.3 Sediment color

The color difference between samples was first identified by naked eyes. Annex A-4 includes scanned images of the sand samples. The mineral composition based on color was interpreted using the image analysis after taking sand sample image under the microscope (Olympus MVX10).

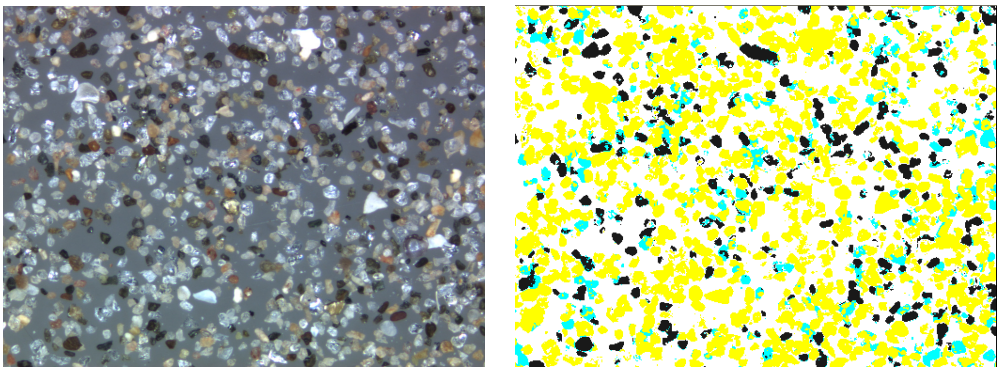

Figure 4.12. Sample 116 images before and after classification.

Annex A-3 includes photo of the microscope. Annex A-4 includes photos taken under the microscope. Each image was classified into a number of clusters. Each cluster sorts pixels of the same features, representing a kind of mineral component. Finally three clusters were acquired, Opaque, transparent, and colorful grains. The image classification was based on supervised classification using Isodata algorithm (the same way as explained in chapter 3 except that the classification is supervised and the spectral signals is defined from the picture itself). Figure 4.12, presents the image of the sample 116 taken under the microscope and after classification.

4.5 Results and discussion

4.5.1 Thermo-luminescence

The sediment supply from the both branches of the Nile River and the sand dunes are the dominant sources of sediment along the entire study area. Based on the test protocol, TL measurements were carried out for all collected field samples. All natural glow curves show peaks in signal intensity at approximately 300° C and 425° C. All test dose curves show peaks at approximately 250° C to 350° C. Figure 4.13, presents the normalized TL glow curves (the average of four discs for each sample) for three samples, two samples from Rosetta and Damietta branches near Delta barrages (136, 178) and one typical coastal sample (116). It is found that the TL signals of the River have much larger values than the coastal sample.

Figure 4.14, demonstrates the spatial distribution of the natural residual TL intensity in terms of the alongshore horizontal coordinates along the Nile Delta Coast. Detailed measurements of the TL are illustrated in annex A-1. TL intensity is expressed as an average of the normalized TL glow curve over the two temperature ranges. The first

range is from 200-4500 C for both natural and artificial dose, and the second is from 3500 C to 4500 C for natural and from 2500 C to 3500 C which covers dominant TL signals. It is noted that the standard deviation of the measured TL in the first range is less than the ones in the second range.

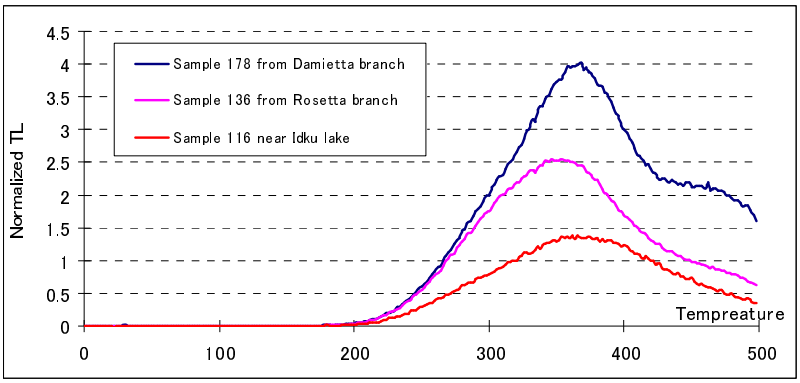

Figure 4.13. Normalized TL glow curves for two River samples (178 from Damietta branch, 136 at Rosetta branch (both samples near Delta barrages), and one coastal sample (116 near Idku jetty).

It is found that the TL signals gradually decrease with increasing distance from their primary source at the both branches Rosetta and Damietta as the sediment experience increasing light exposure during transport process, which indicates sediment alongshore transport features. Local TL intensity variation can also be observed around the middle part of the Nile Delta which might be due to the existence of the sand dunes near this area.

The small difference of TL intensities between the sand grains near the river mouth and the ones on the natural coast indicates that the sediment supply from the river is limited. On the right side of Rosetta mouth TL signal is dropped within a short distance and this feature indicates that the sediment moves slowly at this area due to the existence of five groins. The estimated sediment transport directions based on the TL analysis are consistent with the interpretations based on the analysis of land-sat images around Rosetta promontory while these two estimations were contrary to each other on the west side of Damietta promontory. Observed inconsistency may be due to fluctuating errors of TL measurements since, as discussed previously, little sand supply from the river ended up to yield finite difference of TL along the coast even around the river mouth.

4.5.2 Sediment physical properties

Grain sorting patterns in beach and shelf sediments are strongly influenced by the dynamic action and energy of waves and currents. The sediment characteristics trends generally follow the hydrodynamic processes of shoreline erosion, or accretion, along the Nile Delta. As expected, the greater the rate of erosion, the more concentrated is the coarser grains while the finer grains accumulate in areas with increased rates of accretion. The upper part of Figure 4.15, presents the sand samples and their location while the lower part demonstrates the grain size (D_{25}, D_{50}, D_{75}) for each sample along the Nile Delta Coast. Detailed measurements of the sediment sizes are illustrated in annex A-1. In general the grain distribution indicates that the sand samples are well-sorted. Frihy and Dewidar, (2003) mentioned that the nearshore area of the Nile Delta is generally covered with shore-parallel belts of graded grain sizes having a finding offshore trend. These belts, beginning from shore, contain grain sizes of 0.167-0.5 mm, 0.125 - 0.167 mm to 0.063 - 0.125 mm. Conversely, this pattern is locally disrupted by scattered patches of coarse rgrained sediment (0.125 - 0.5 mm) on the outer nearshore zone Burullus promontory. This coarse-gained sediment might be related to relict sediment dispersed from former Nile branches, probably the Canopic, Saitic and Sebennitic distributaries. The grain size distribution is in line with the results of Frihy and Dewidar, (2003).

Investigations of sampled sand grains yield following many findings. Clear difference was noticed by the naked eyes in the sand color, and size between different areas. Around Rosetta promontory the sand color is light and average size is 0.28 mm, while in the middle part of the Delta (Baltim to Gamasa) the color is lighter and grain sizes are coarser with average size of 0.6mm, and from Damietta to Port Said the color is darker and average grain size is 0.23mm. Frihy and Dewidar, (2003) demonstrated that the correlation between the seafloor change rate and the mean grain size is very poor however the correlation coefficient between the contents of heavy mineral with the seafloor changes is nearly to 0.5.

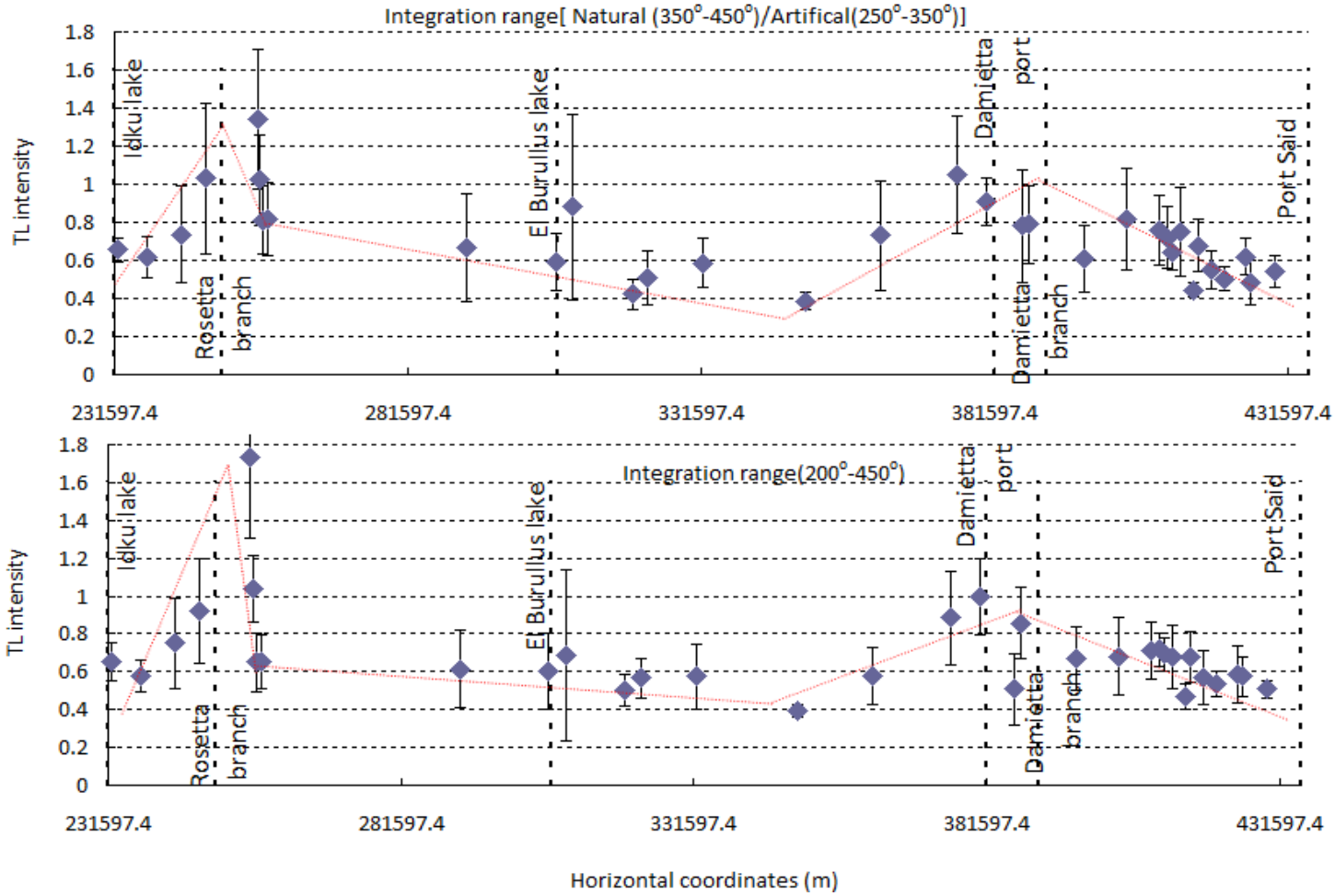

Figure 4.14. Spatial distribution of residual TL intensity in the research area.

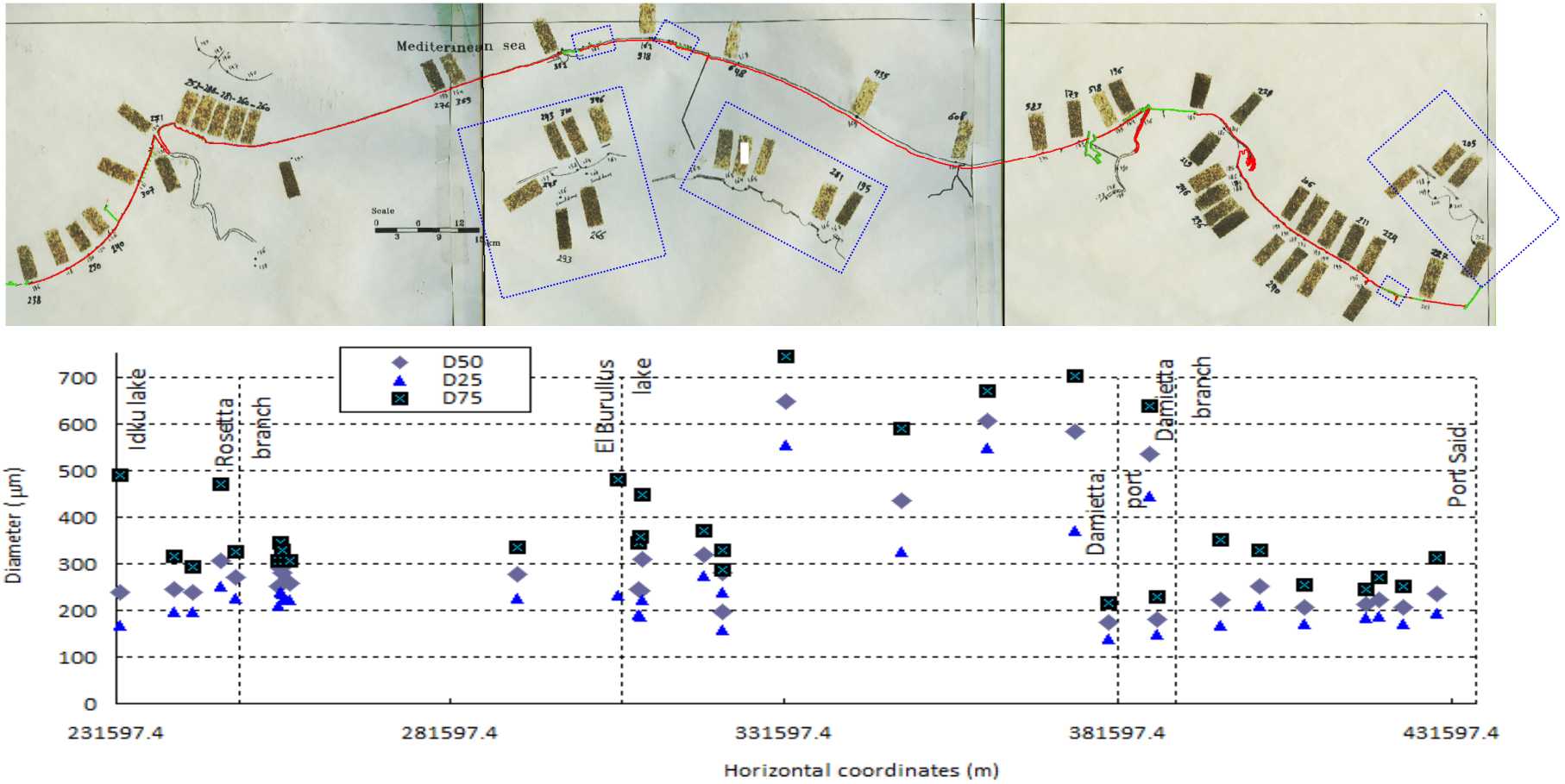

Figure 4.15. Spatial distribution of the grain size along the research area.

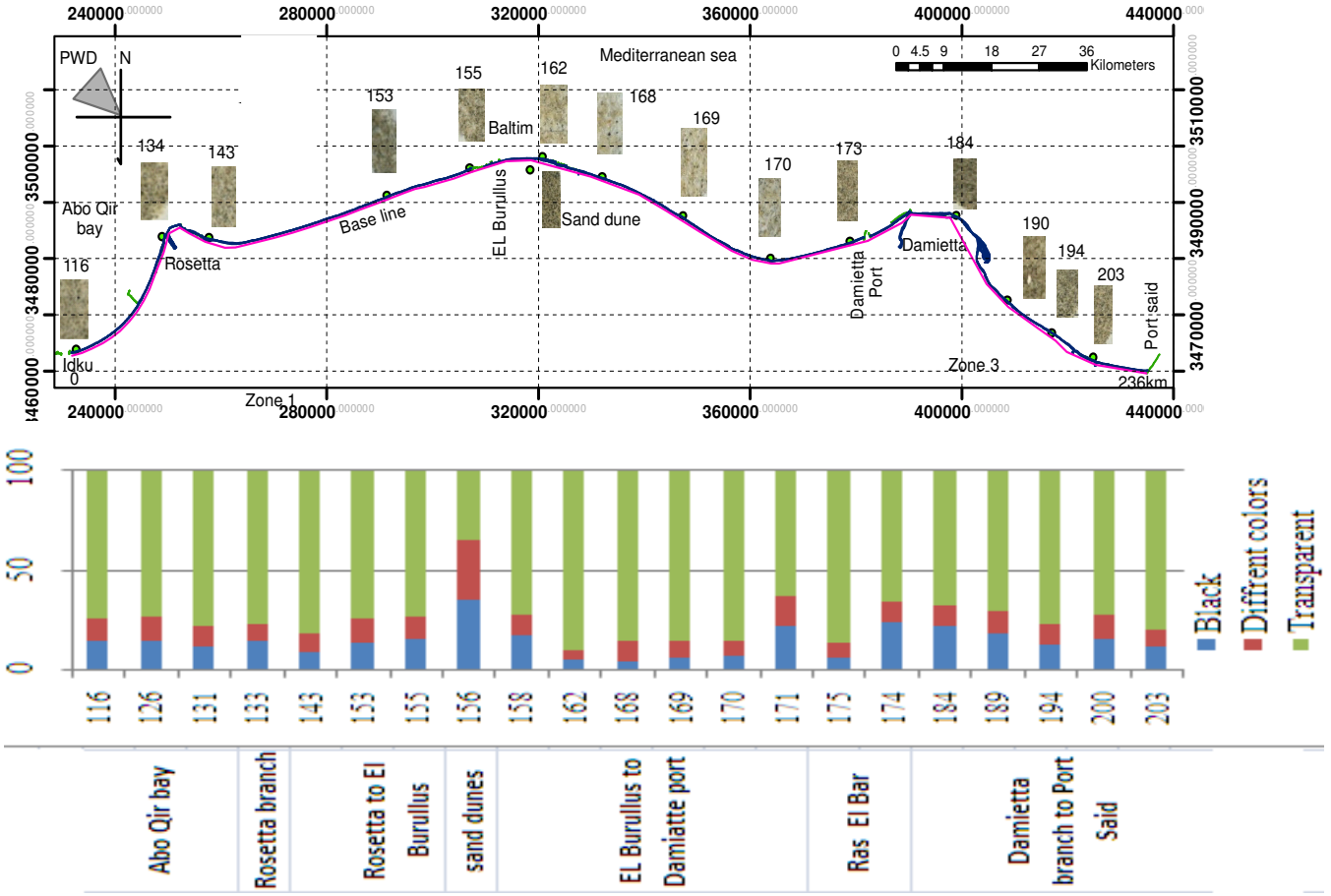

Figure 4.16. Spatial distribution of the sand samples composition.

Three sample images taken under the microscope are presented in Figure 4.17. These images for the samples number 168 (representing the middle part, it is large and dominated by transparent grains), 116 (near the Idku lake representing an accreted area, it is fine grains with high percentage of black color grains), and 156 (representing the sand dune, dominated by black color).

Sand compositions examined in terms of the grain colors by analyzing the images of the sand samples under the microscope. Average of three images for each sample was considered in this analysis. The sand samples were classified to three categories, transparent (feldspar or quartz), black (magnetite and ilmenite), and colorful (amphiboles (mainly dark green hornblende), pyroxenes (mainly augite), epidote, garnet (various colors), tourmaline, zircon,rutile, monazite, kyanite, and staurolite) grains. The composition of different samples along the Delta Coast is presented in Figure 4.16. The evidence which concluded from this analysis was that the sediment comes from the river contains black sand with small size and other colors with bigger size. The dark sand is dominant in the sand dunes. The sand samples near the large traps i.e., Idku jetty, El Burullus jetty, and Damietta breakwater are characterized by dark color. This illuminates that the dark grains is smaller than other grains which moves easily and accumulated near the coastal structure.

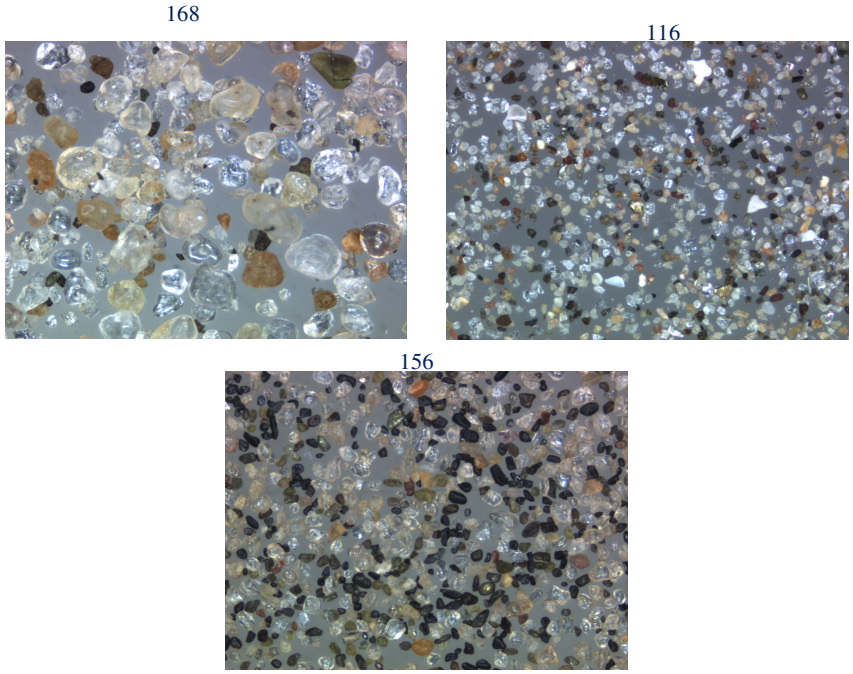

Figure 4.17. Enlarged images under the microscope for sand samples number 168, 116, and 156.

Chapter5 Wave model

5.1 General

The numerical models have great contribution in understanding several coastal engineering problems. These models allow quantification of altered conditions (waves, coastal structures, boundary conditions, bathymetry, and so on). The numerical models could be used over different scales in time and space. The main problems faced the numerical models are; 1) the adequate information about the study site (detailed description of the study site data were acquired for the Nile Delta Coast (NDC) as explained in the pervious three chapters), 2) the limited set of processes which included within the model due to the assumptions and the difficulties of incorporating some features along the coast.

It is not always obvious which model is most suitable to a particular problem. Various physical situations are existed in the coastal zone however there is no unique model applicable to simulation of all these physical conditions. So the model should be chosen to cover the important physical process at the study site.

The long-term predictive morphology change models are crucial for the coastal management. However, to ensure the applicability of these models, they should be computed efficiently. This chapter carried out numerical simulations of shoreline changes observed along the Nile delta coast. The simulation consists of two parts, wave module and shoreline module, respectively. The wave model simulates the wave transformation.

5.2 Brief review on wave model

Wave models could be classified into: 1) phase-resolving models (deterministic), and 2) phase-averaging models (stochastic).

In the first type, the fluctuating instantaneous sea surface is directly resolved, i.e. the surface is covered with a grid which must be sufficiently fine relative to the wave length. The individual waves in a spectrum are resolved as per their phase. The phase-resolving models are used when average properties of waves change rapidly and when there is rapid variations in depth and shoreline. Among the phase-resolving wave models; Boundary integral models, Mild Slope Equation model, Shallow Water Equation model, and Boussinesq Equation

models. The mild slope equation is weekly nonlinear and required mild bed slope. The Boussinesq model consists of one continuity equation and one momentum equation. It was derived by (Peregrine, 1966) and it was restricted to shallow water and it was weak nonlinearity. Various attempts have been made to improve the applicability of Boussinesq equations by improving the frequency dispersion characteristics, Madsen et al.(2006), and by including the effect of vortex. The phase resolving models are capable to describe the shoaling, diffraction, and refraction at the intra-wave scale (fine resolution in space and time). Nonlinearity is accounted for and the computation of the current could be done implicitly. These models still have some instability and need high computational time; also they are less dispersive in deep water.

In the second type, wave models, is commonly based on Energy Balance equation and Parabolic equation. The phase-averaged wave energy is computed. These models consider evolution of a directional and frequency spectrum. These models predict averaged or integral properties like significant wave height, average wave period, and wave energy etc. These models are used when average properties change slowly over few wave lengths. The phase average models have the advantages of that it is quite stable and takes less computational time (Coarse resolution). It is highly dispersive and the generation, dissipation and wave-wave interaction could be included. Drawback of these models in coastal waters is the use of linear wave theory for wave propagation and explicit computation for the current. Also for detailed investigation of the beach morphology in the nearshore zone, it is better to use the phase resolving models. Tajima and Madsen (2006) incorporated the non linear effects by establishing a correspondence between linear and non-linear wave characteristics. Horikawa and Kuo (1966) studied the linear wave transformation inside the surf zone analytically based on the concept of the phase average model. Dally and Dean (1985) investigated the intuitive expression for the spatial change in energy flux associated with wave breaking in the surf zone. Several studies followed the same concept were carried out. The basic equation of the Energy balance equation is:

$$\frac{\partial N}{\partial t} + C_g \nabla N = -\varepsilon N \qquad \textbf{(5.1)}$$

Where, N=N (f, θ, x, y, t) is the directional Spectrum (f = wave frequency, θ = angle of wave approach, x and y are horizontal coordinates, t = time instant),

$$-\varepsilon N = N_{in} + N_{nl} + N_{ds} \qquad \textbf{(5.2)}$$

Where, N_{in} is the source term representing wind energy input; N_{nl} is the source term representing input energy from non-linear interaction between different wave frequencies in a spectrum resulting in energy transfer to another component. There can be two components in a spectrum which resonate. If they transfer energy to third one then it is known as Triad. If four components interact, then it is known as quadruplate. N_{ds} is the source term representing energy loss in dissipation like breaking.

Three generations were developed until now based on this concept. The WAM and SWAN are among most famous models following the concept of phase average. Originally they don't count for diffraction. Recently diffraction is included by different ways based on approximation from Mild Slope Equation or approximation based on Parabolic Equation. (Mase 2001) developed a random wave transformation model called in which diffraction effects were included. The diffraction term was introduced by utilizing the parabolic approximation of the wave equation. The numerical scheme is stable (the first order upwind finite difference). Mase et al. (2005) improved his model by using Quadratic upstream interpolation for convective kinematics in the discretization to reduce numerical diffusion, in addition to taking the account of reflection in his model. The main Advantage of using the Mase's model is the ability to reproduce wave transformation over complicated bathymetry and setting up the input and output for many different wave spectra.

5.3 Objective of present wave modeling

The Purpose of the wave model is to quantify the change in the wave's parameters (height, direction) between the deep water up to the neashore zone especially at the breaking zone. The waves at the nearshore zone are strongly affected by the variation of the bathymetry and the existence of coastal structures. The wave parameters and the cross shore and longshore gradients are very important in calculating the sediment transport in cross and longshore. Here, as the long term change is considered, the longshore sediment transport is only taken into consideration.

5.4 Description of wave model

The used wave model is the EBE model which was developed by Mase (2001) based on the energy-balance equation for multidirectional random waves taking into account wave shoaling, refraction, diffraction, and wave breaking.

Basic assumptions

1- Steady state random waves.
2- The breaking is the only dissipation term taken into consideration. Assumptions based on Tajima and Madsen (2006) is followed. Random waves are narrow banded, wave height is following the Raleigh distribution, and only waves of heights larger than the local breaking wave height are breaking.
3- The input spectrum is constant along the offshore boundary.
4- No reflection is considered in the model (All structures are energy dissipative , the model should perform backward marching for seaward if reflection taken into consideration)
5- Linear refraction and shoaling are considered, and the diffraction is included based on Mase 2001 model.
6- The slope is mild and it is always in the wave direction (the energy propagates from offshore to onshore only) when the slope is against the wave direction it is considered as horizontal slope.

5.4.1 Energy Balance equations

For computations of the wave field, this study applied horizontal steady state conservation equations of the spectral energy of the waves and accounted for the effect of wave diffraction by introducing (Mase, 2001) dispersion-type terms.

$$\frac{\partial C_x N}{\partial x}+\frac{\partial C_y N}{\partial y}+\frac{\partial C_\theta N}{\partial \theta}=-\varepsilon_b N+\frac{k}{2\sigma}\left[\frac{\partial}{\partial y}\left(CC_g\cos^2\theta\frac{\partial N}{\partial y}\right)-\frac{1}{2}CC_g\cos^2\theta\frac{\partial^2 N}{\partial y^2}\right] \quad \textbf{(5.3)}$$

Where, N is the wave action, $N(x,y,\theta,f)=E/\sigma$; θ is the wave angle. The second term at right side is the diffraction effect proposed by (Mase, 2001) and Mase et al. (2005). Here, C is the wave phase velocity, C_g is the wave group velocity, κ is a coefficient, $\kappa=2.5$ was adopted by (Mase, 2001) .The characteristic velocities c_x, c_y and c_θ are defined as follows.

$$c_x=C_g\cos\theta \quad \textbf{(5.4)}$$

$$c_y=C_g\sin\theta \quad \textbf{(5.5)}$$

$$c_\theta=\frac{\sigma}{\sinh 2kh}\left(\frac{\partial h}{\partial x}\sin\theta-\frac{\partial h}{\partial y}\cos\theta\right) \quad \textbf{(5.6)}$$

Where, C_g is the group celerity. σ is the intrinsic wave frequency. The dispersion relation of waves with uniform current is expressed as

$$\sigma^2 = gk \tanh kh \tag{5.7}$$

5.4.2 Wave breaking model

The energy dissipation was estimated by Tajima & Madsen's (2006) model. In 5.3, ε_b : is the coefficient of wave energy dissipation term.

$$\varepsilon_b N = \frac{K_b}{h} C_g \exp(-\zeta_b^2)\left[E_{total}(1+\zeta_b^2) - E_r\right].\frac{N}{E_{total}} \tag{5.8}$$

Where,

$$\zeta_b = \frac{H_b}{H} \tag{5.9}$$

$$K_b = \begin{cases} \frac{5}{2}\frac{\gamma_s^2 \tan\beta}{\gamma_s^2 - \gamma_r^2}, \tan\beta > 0 \\ \frac{5}{16}\gamma_r, \tan\beta \le 0 \end{cases} \tag{5.10}$$

$$\gamma_s = \gamma_r + 4\tan\beta \tag{5.11}$$

$$\gamma_r = 0.3 \tag{5.12}$$

$$E_r = \frac{\rho g(\gamma_r h)^2}{8} \tag{5.13}$$

And the breaking wave height H_b is estimated by

$$\frac{k_b H_b}{\tanh k_b h_b} = 1.07 - 0.59\exp\left(-8.6\frac{h_b}{L_0}\right) + 2.59\tan\beta\ \exp\left(-15.1\left(\frac{h_b}{L_0}\right)^{1.5}\right) \tag{5.14}$$

Where, H is the wave height, k is the wave number, β is the bed slope, h is the water depth, L_0 is the deep water wave height, and the b indicate the breaking. An iterative procedure was applied for the computations of such implicit energy dissipation term.

5.4.3 Boundary conditions

At the offshore boundary, incident wave is random in terms of both frequency and direction. The wave spectra are generally expressed as the product of frequency spectrum N(f) and directional spreading function G(f,θ). The spectra were determined based on Bretschneider-Mitsuyasu type frequency spectrum and the Mitsuyasu type directional spreading function

with specified significant wave heights, periods, mean wave directions and spreading parameters of directional spectra.

$$N(f,\theta) = N(f).G(f,\theta) \tag{5.15}$$

$$N(f) = 0.257 H_{\frac{1}{3}}^{2} T_{\frac{1}{3}}^{-4} f^{-5} \exp\left[-1.03\left(T_{\frac{1}{3}} f\right)^{-4}\right] \tag{5.16}$$

$$G(f,\theta) = G_0 \cos^{2s}\left(\frac{\theta}{2}\right) \tag{5.17}$$

$$G_0 = \left[\int_{\theta_{\min}}^{\theta_{\max}} \cos^{2s}\left(\frac{\theta}{2}\right) d\theta\right]^{-1} \tag{5.18}$$

$$S = \begin{cases} S_{\max}.(f / f_p)^5 & f \le f_p \\ S_{\max}.(f / f_p)^{-2.5} & f \ge f_p \end{cases} \tag{5.19}$$

$$f_p = \frac{1}{1.05 T_{\frac{1}{3}}} \tag{5.20}$$

Where, f is the frequency, and f_p is the peak frequency.$H_{1/3}$ & $T_{1/3}$ are the significant wave height and period respectively. S_{max}=25 is considered in this study. Goda et al. (1978) suggested the below values of S_{max}.

$$S_{\max} = \begin{cases} 10 & \text{for wind waves} \\ 25 & \text{for swell with short to medium decay distance} \\ 75 & \text{for swell with meduim to long decay distance} \end{cases} \tag{5.21}$$

At the onshore boundary the land is assumed to absorb all the energy. The both sides of the study site, No energy can enter the domain and energy can freely leave the domain.

5.4.4 Discretization scheme (Numerical solution)

Governing equations are discretized by finite difference method (the first order upwind scheme) (Mase, 2001). Considering waves are mainly propagating in *x* direction, *x* directional derivative is approximated by explicit difference, and y directional derivative and θ directional derivative are approximated by implicit difference. In this way, wave height can be calculated step by step in *x* direction from offshore to onshore, and in each step wave spectrum is calculated implicitly. Since the slope along the NDC is not in the x direction, an

iterative procedure was applied for computations to include the energy dissipation. As (Mase 2001) after discretaizing $\frac{\partial C_x N}{\partial x}+\frac{\partial C_y N}{\partial y}+\frac{\partial C_\theta N}{\partial \theta}=-\varepsilon_b N+\frac{k}{2\sigma}\left[\frac{\partial}{\partial y}\left(CC_g\cos^2\theta\frac{\partial N}{\partial y}\right)-\frac{1}{2}CC_g\cos^2\theta\frac{\partial^2 N}{\partial y^2}\right]$ (5.3, it yields the below equation.

$$A_1 N_n^{ijk}+A_2 N_n^{i(j-1)k}+A_3 N_n^{i(j+1)k}+A_4 N_n^{ij(k-1)}+A_5 N_n^{ij(k+1)}=-BN_n^{(i-1)jk}-\varepsilon_b N_n^{ijk} \quad \textbf{(5.22)}$$

Where,

$$A_1=c_x^{(i+1)jk}/\Delta x+\varepsilon_{bn}^{ij}+\frac{k}{2\omega_n\Delta y^2}\left\{\left(CC_g\right)^{i(j+1)k}+\left(CC_g\right)^{ijk}-\left(CC_g\right)^{i(j+1/2)k}\right\}.\cos^2\theta_k$$
$$+\begin{cases}c_{yn}^{i(j+1)k}/\Delta y & (c_y\ge 0)\\ -c_{yn}^{ijk}/\Delta y & (c_y\ge 0)\end{cases}$$
$$+\begin{cases}c_{\theta n}^{ij(k+1)}/\Delta\theta & (c_{\theta n}^{ijk}\ge 0, c_{\theta n}^{ij(k+1)}\ge 0)\\ 0 & (c_{\theta n}^{ijk}\ge 0, c_{\theta n}^{ij(k+1)}<0)\\ \left(c_{\theta n}^{ij(k+1)}-c_{\theta n}^{ijk}/\Delta\theta\right)/\Delta\theta & (c_{\theta n}^{ijk}<0, c_{\theta n}^{ij(k+1)}\ge 0)\\ -c_{\theta n}^{ijk}/\Delta\theta & (c_{\theta n}^{ijk}<0, c_{\theta n}^{ij(k+1)}<0)\end{cases} \quad \textbf{(5.23)}$$

$$A_2=\frac{k}{2\omega_n\Delta y^2}\left\{-\left(CC_g\right)^{ijk}+\frac{1}{2}\left(CC_g\right)^{i(j+1/2)k}\right\}.\cos^2\theta_k+\begin{cases}-c_{yn}^{ijk}/\Delta y & (c_y\ge 0)\\ 0 & (c_y<0)\end{cases} \quad \textbf{(5.24)}$$

$$A_3=\frac{k}{2\omega_n\Delta y^2}\left\{-\left(CC_g\right)^{i(j+1)k}+\frac{1}{2}\left(CC_g\right)^{i(j+1/2)k}\right\}.\cos^2\theta_k$$
$$+\begin{cases}0 & (c_y\ge 0)\\ -c_{yn}^{i(j+1)k}/\Delta y & (c_y<0)\end{cases} \quad \textbf{(5.25)}$$

$$A_4=\begin{cases}-c_{\theta n}^{ijk}/\Delta\theta & (c_{\theta n}^{ijk}\ge 0, c_{\theta n}^{ij(k+1)}\ge 0)\\ -c_{\theta n}^{ijk}/\Delta\theta & (c_{\theta n}^{ijk}\ge 0, c_{\theta n}^{ij(k+1)}<0)\\ 0 & (c_{\theta n}^{ijk}<0, c_{\theta n}^{ij(k+1)}\ge 0)\\ 0 & (c_{\theta n}^{ijk}<0, c_{\theta n}^{ij(k+1)}<0)\end{cases} \quad \textbf{(5.26)}$$

$$A_5=\begin{cases}0 & (c_{\theta n}^{ijk}\ge 0, c_{\theta n}^{ij(k+1)}\ge 0)\\ c_{\theta n}^{ij(k+1)}/\Delta\theta & (c_{\theta n}^{ijk}\ge 0, c_{\theta n}^{ij(k+1)}<0)\\ 0 & (c_{\theta n}^{ijk}<0, c_{\theta n}^{ij(k+1)}\ge 0)\\ c_{\theta n}^{ij(k+1)}/\Delta\theta & (c_{\theta n}^{ijk}<0, c_{\theta n}^{ij(k+1)}<0)\end{cases} \quad \textbf{(5.27)}$$

$$B=-c_{xn}^{ijk}/\Delta x \quad \textbf{(5.28)}$$

5.4.5 Bathymetry

The used bathymetry acquired from ETOPO1. ETOPO1 is a 1 arc minute bathymetry grid produced by combining diverse global and regional digital data sets developed by National Geophysical Data Center (NGDC) (an office of the National Oceanic and Atmospheric Administration (NOAA), 2008). Since the ETOPO1 is not always reliable in shallow regions. An improved bathymetry for the study area (the NDC) is derived by merging the ETOPO data with the nearshore zone data which extracted from Omar et al. (2005). The nearshore data were derived by digitizing the depth contours of 5, and 10m from bathymetric map in the Nile Delta region (300^{o} E to 32.50^{o} E and 31^{o} N to 32^{o} N) and adding the shoreline from the land-sat image. Digitization of the contours was carried out using AutoDesk land. The map with contour lines was assigned to X–Y projection, and geo-referenced using three points. The digitized data are then gridded and used to modify the existing ETOPO1 datasets for depths less than 25 m using GMT (Generic Mapping Tools) package. Based on the obtained contour map, water depth was interpolated on each square grid with grid size of 50mx50m by using the surface program in the GMT package. The surface program is a generalization of the minimum curvature algorithm. Figure 5.1.A, presents the bathymetry of the NDC based on ETOPO1. Figure 5.1.B, illustrates the bathymetry after modification of ETOPO1 in the nearshore area. The bathymetry around Rosetta promontory in 2003 was developed based on two assumptions; the first is that the closure depth is 10 m; the second is that the profile shape is constant along the coast within this period. Figure 5.2 A, and B present the bathymetry survey around Rosetta promontory in 1978 and 2003 used in this study.

5.4.6 Wave conditions

The wave condition is a very important factor representing the driving force of the sediment transport. The wave conditions along the NDC considered in this study was decided based on the analysis of literature review from previous studies. Wave roses at Rosetta and Damietta mouths in winter and non-winter seasons were presented in Chapter 2, Section 2.4.

Nafaa et al. (1991) analyzed the wave records at Abu Qir between 1971 and 1987. The data was recorded by an offshore pressure operated suspended wave recorder. Nafaa et al. (1991) concluded that the severe wave conditions could reach as high as 4.0 m with wave period of 14 sec in winter, 3.50 m in spring, and 2.50 m in summer with wave period of 13 sec. Nafaa et al. (1991) also discussed that the average significant wave height is within the range of 0.50 - 1.00 m, and the average wave period is 7-8 sec. Dominant wave direction is WNW-

NW while a small amount of waves arrives from the NNE-NE sector. Abdallah et al. (2006) studied the wave data at Abu Qir bay in 1986, and concluded that about 87% of all wave height are less than or equal to 1.5 m and 13% is greater than 1.5m. Most of the wave period values (59%) range between 5 and 8 s with an annual mean period of 6.5 s. About 80% of wave periods are less than or equal to 8 s. Frihy et al. (2010) pointed that the deep-water climate are uniform along the NDC are uniform in term of average wave conditions. The waves are dominantly arriving from the NW with percentage of occurrence reaches 75% and rarely from the NE (20%). 5% of the time, wave components approaching from the SW and SE quadrants.

In the current study, the height of the offshore wave was taken as 1 m and the corresponding wave period was 7 sec as concluded from the literature review. This offshore wave was used as input data for the Energy Balance Equation (EBE) model in order to reproduce the nearshore wave climate at the study sites from four different directions (N, NW, NNW, and NE).

5.5 Results and discussion

Since we assume that the wave propagates in x-direction so the energy dissipation is calculated in the x-direction. However, the cross-shore direction is not in the x-direction at everywhere along the coast especially in the west side of Rosetta promontory, thus the effect of broken wave energy dissipation term was iteratively computed. The energy dissipation is a function of the wave height H_i. since the target is H_i so in the direct calculation ,the dissipation term is calculated based on the wave height from the point behind the current point, H_{i-1} (assuming that the energy is dissipated in the x direction). In the iterative method, first we calculate the energy dissipation based on H_{i-1} then Hi could be easily calculated. The energy dissipation is recalculated again using the Hi. This process is repeated until the difference between H_i in two successive time steps is very small. Comparison between the wave height transformation in two cases (calculation of energy dissipation with or without iterative approach) is presented in Figure 5.3. In Figure 5.3 the wave transformation around Rosetta mouth is presented due to deep water wave of 1 m height propagating from the NW direction.

Based on the wave specter from the EBE model, this study extracted significant wave heights and average wave directions. Figure 5.4 to Figure 5.7 illustrates the results obtained from the

EBEM computations for four cases in which the model applied different deep water wave directions, N, NNW, NW, and NE respectively. In all these four cases, significant wave height and period in deep water were respectively set as 1m and 7 sec. Alongshore distributions of the breaking wave heights and directions are illustrated in Figure 5.8. The variation of the breaking wave height along the NDC for the four cases shows three local peaks at Rosetta, El Burullus and Damietta. These peak wave heights could represent the erosion took place around these three locations.

The breaking wave height along the NDC in the four cases varies from 0.5 m to 1.32 m and the maximum wave height is computed around Rosetta mouth. The wave height for the cases of the wave incident from the N and the NNW are higher than the other two cases around Rosetta mouth.

The wave direction is measured from N direction counter clock wise. The breaking wave direction varies from -0.8 radian to 1 radian. The breaking wave direction (measured counter clock wise) respected to the shoreline orientation varies from -1.5 radian to 0.9 radian as presented in Figure 5.9 in term of the alongshore distance start from Idku lake at 0 to Port Said at 240100 m. The waves caused transportation of the littoral sediment along the study Delta Coast. Based on the breaking wave information versus the shoreline orientation, some evidences were revealed.

The predominant wave directions from the N and NW generate eastward longshore currents. However, wave incident from the NE generates a reverse westward longshore current. Around Rosetta promontory, along the western and eastern sides of Rosetta mouth, the sediment is generally moves toward the Southwest (SW) and E respectively due to waves coming from the N to NW sector. Reverse effect were experienced due to waves approaching from the NE. Around Damietta promontory, along the western and eastern sides of Damietta mouth, the sediment generally moves toward the NNE and SW respectively due to waves coming from the N to NW sector. On the contrary, waves approaching from the NE direction generate the movement in the opposite directions.

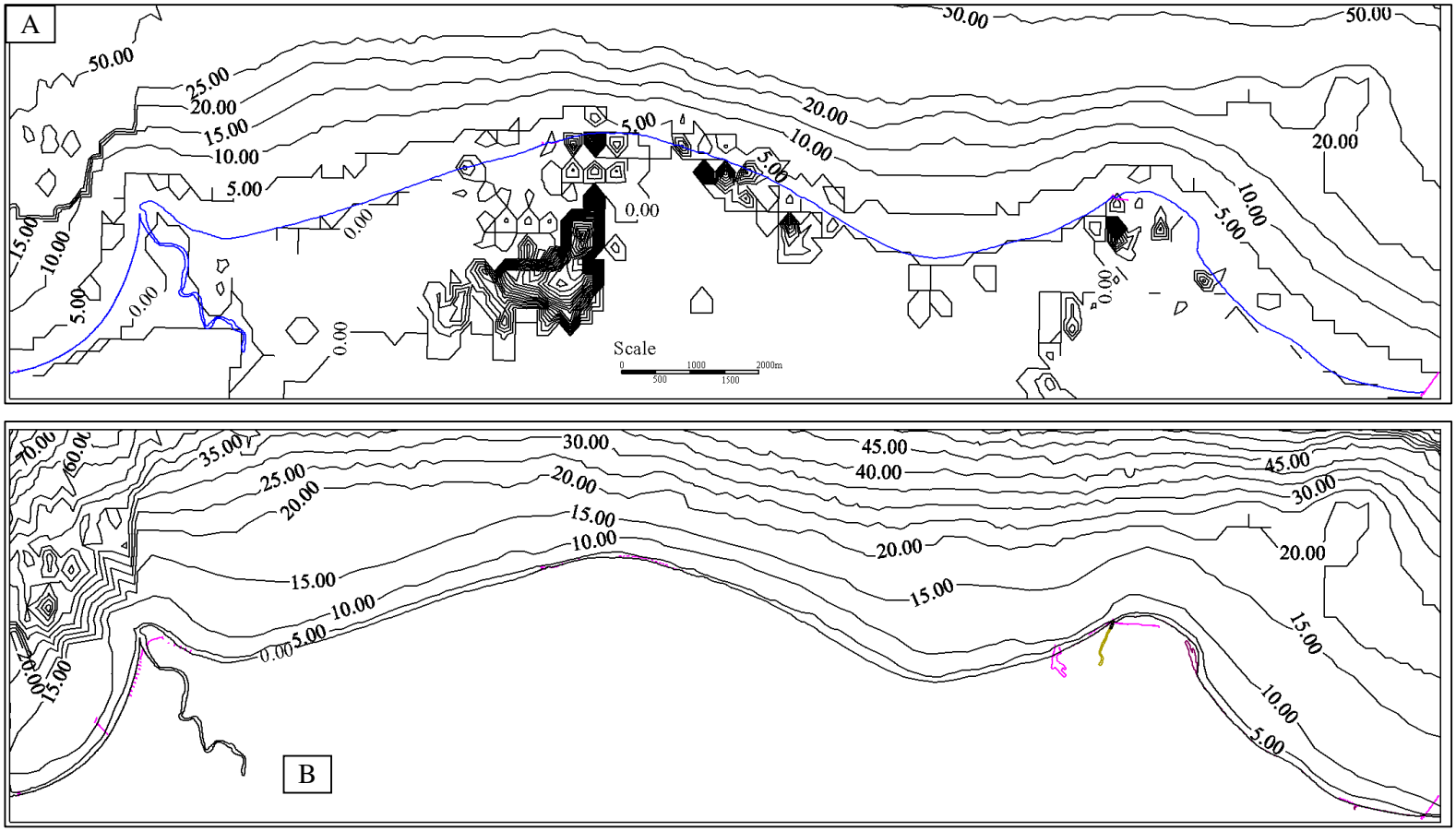

Figure 5.1. A) Bathymetry Data from ETOPO1, B) Bathymetry data after improvement for 1978.

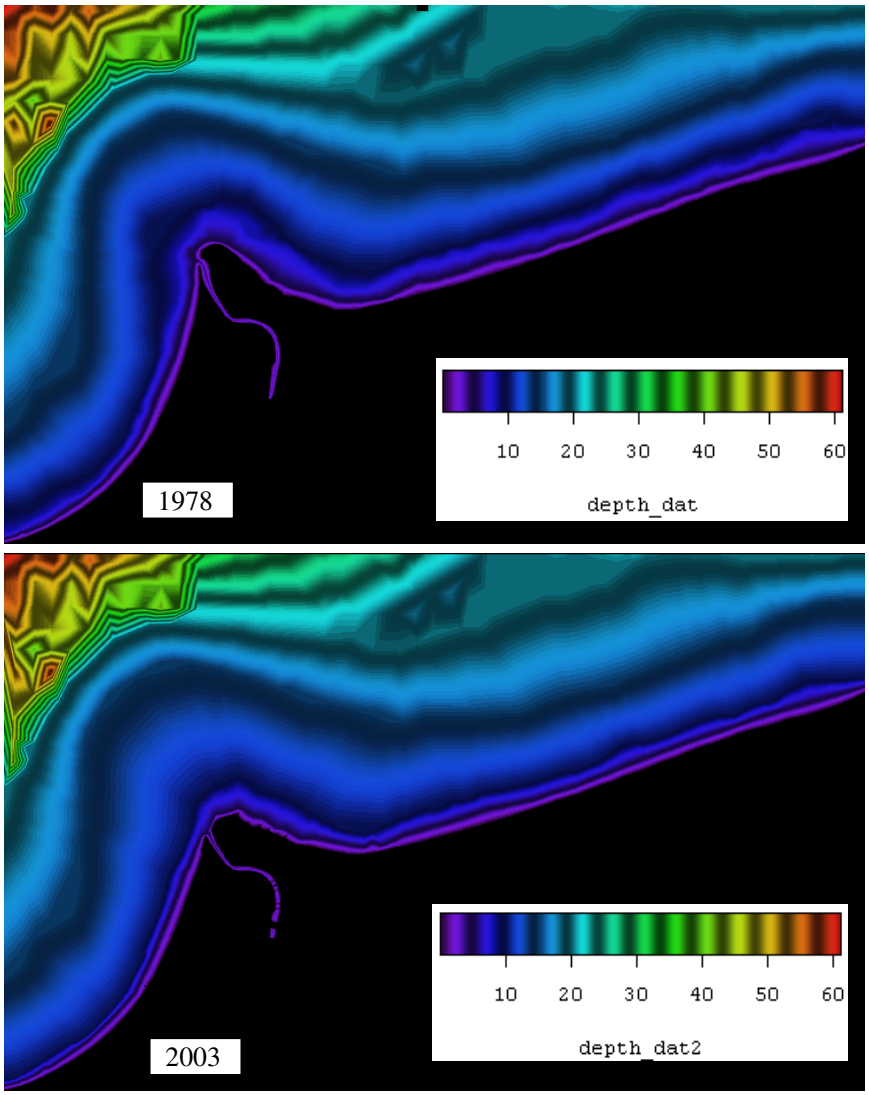

Figure 5.2. The bathymetry around Rosetta promontory (m).

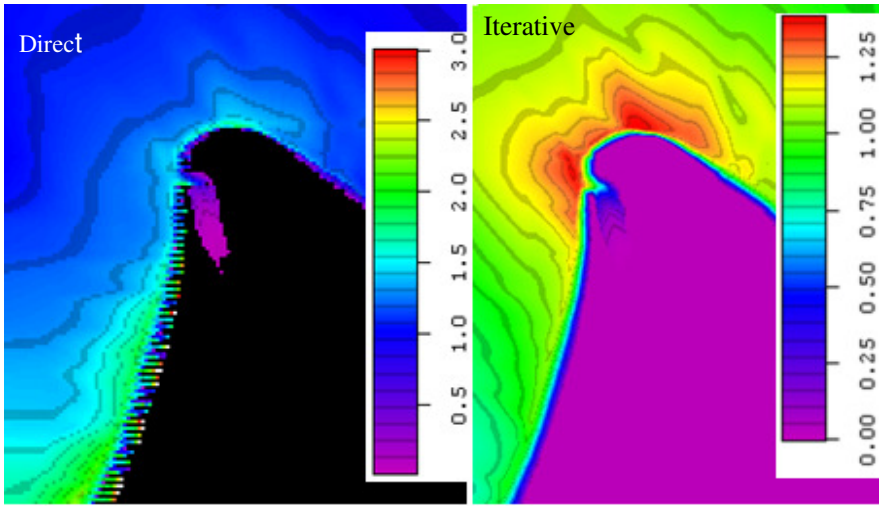

Figure 5.3. Wave transformation at Rosetta mouth for two cases, energy dissipation is included directly and iteratively.

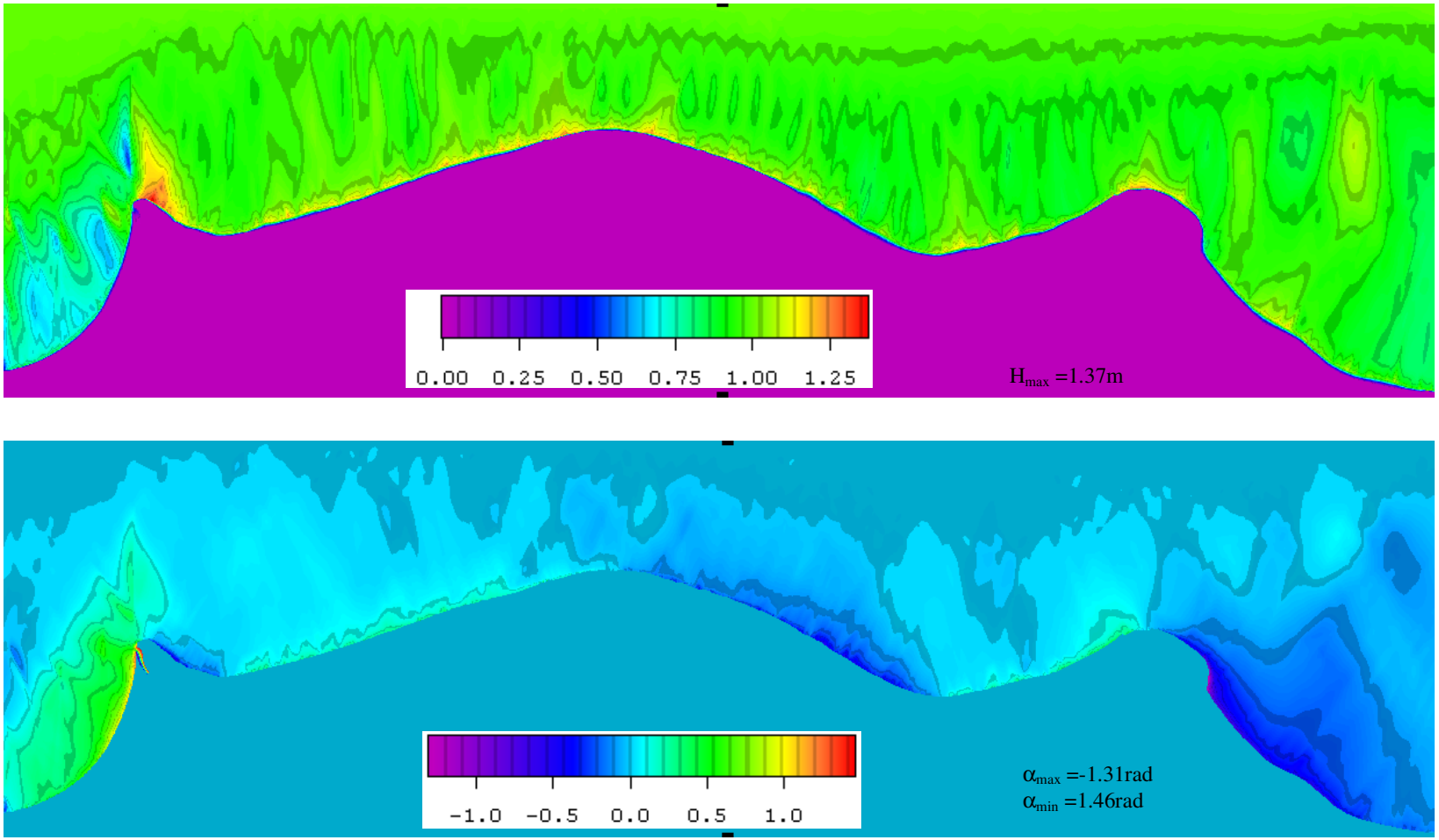

Figure 5.4. Wave height and wave direction in the study site, deep water wave height of 1 m propagating from the N direction.

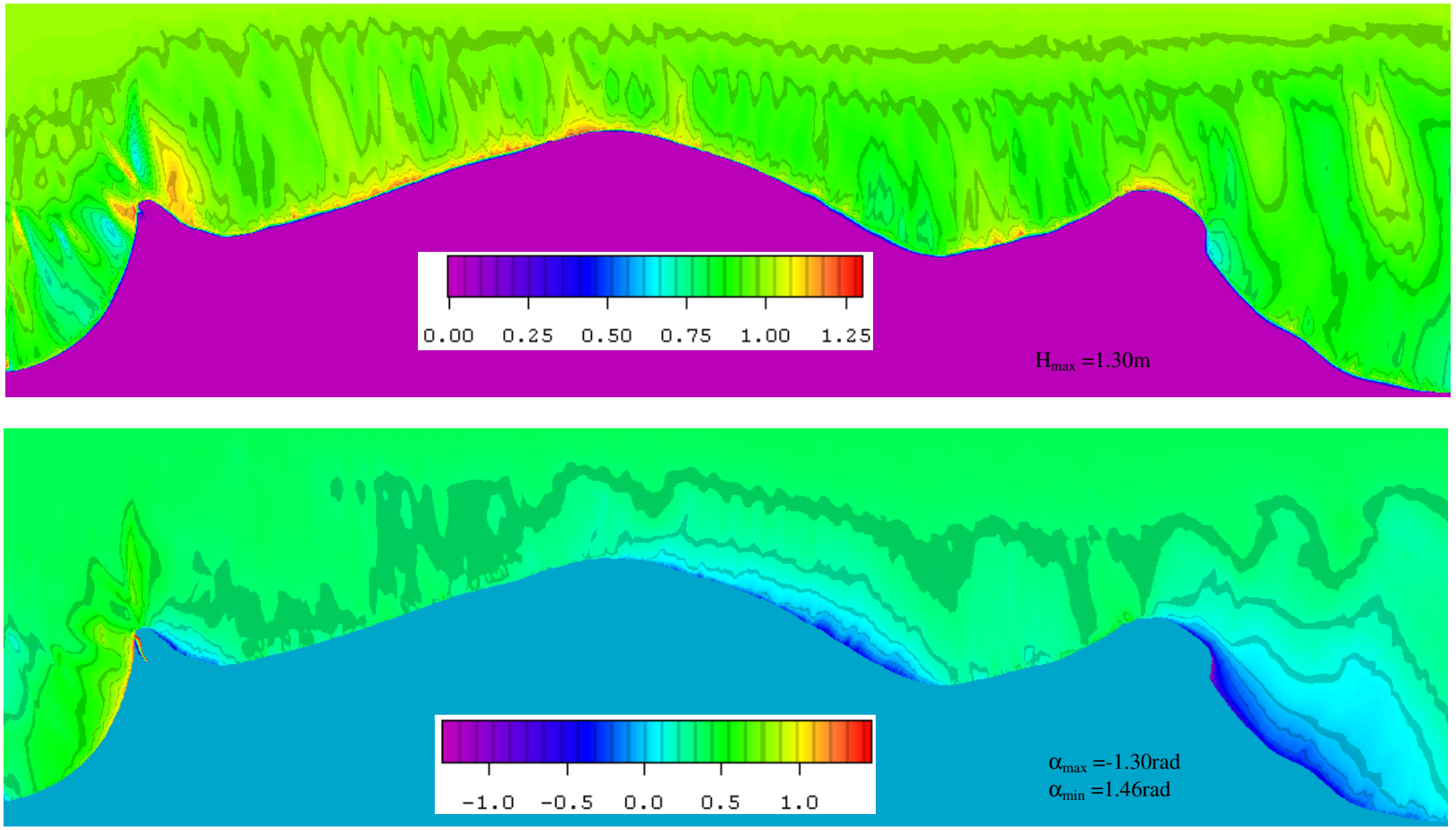

Figure 5.5. Wave height and wave direction in the study site, deep water wave height of 1 m propagating from the NNW direction.

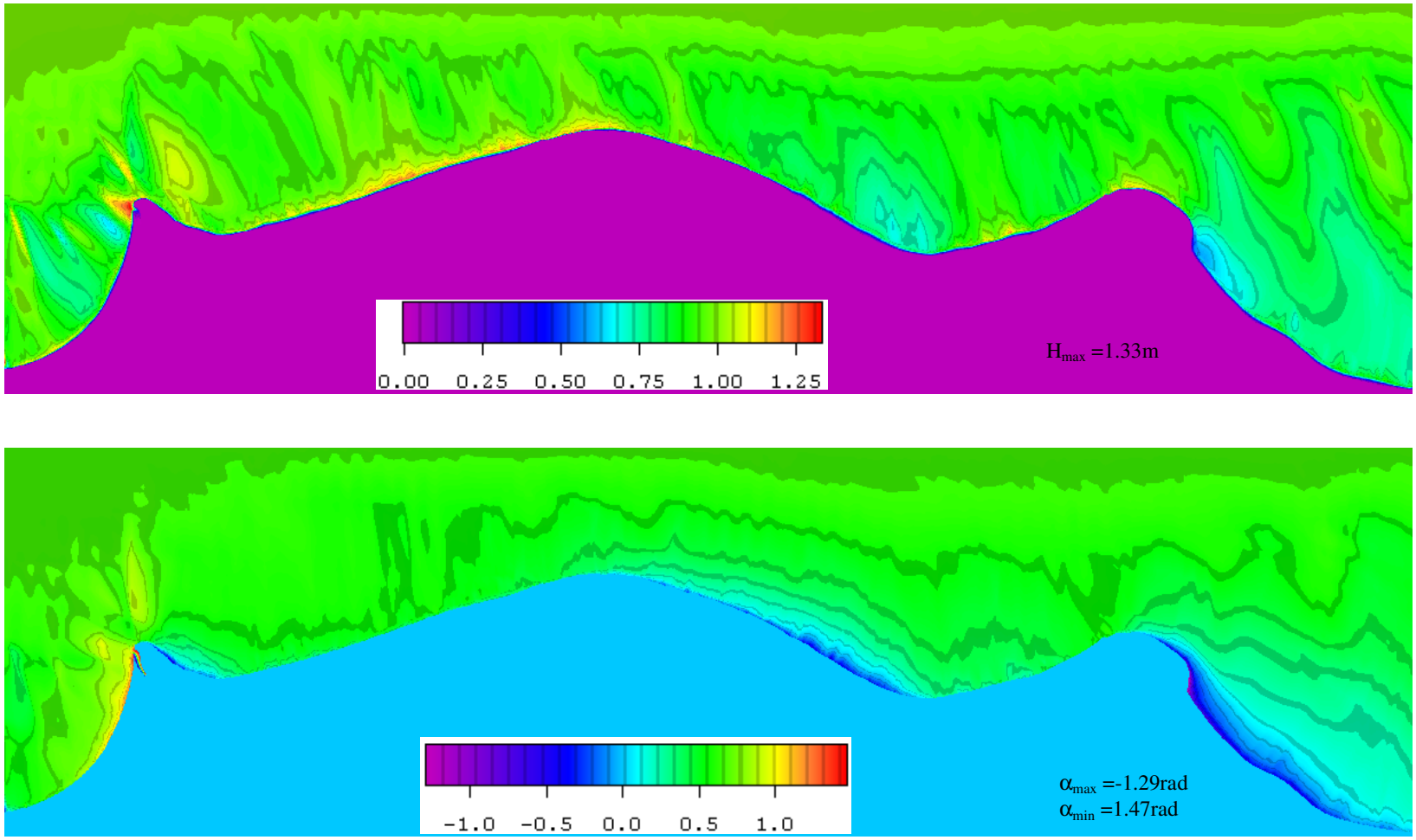

Figure 5.6. Wave height and wave direction in the study site, deep water wave height of 1 m propagating from the NW direction.

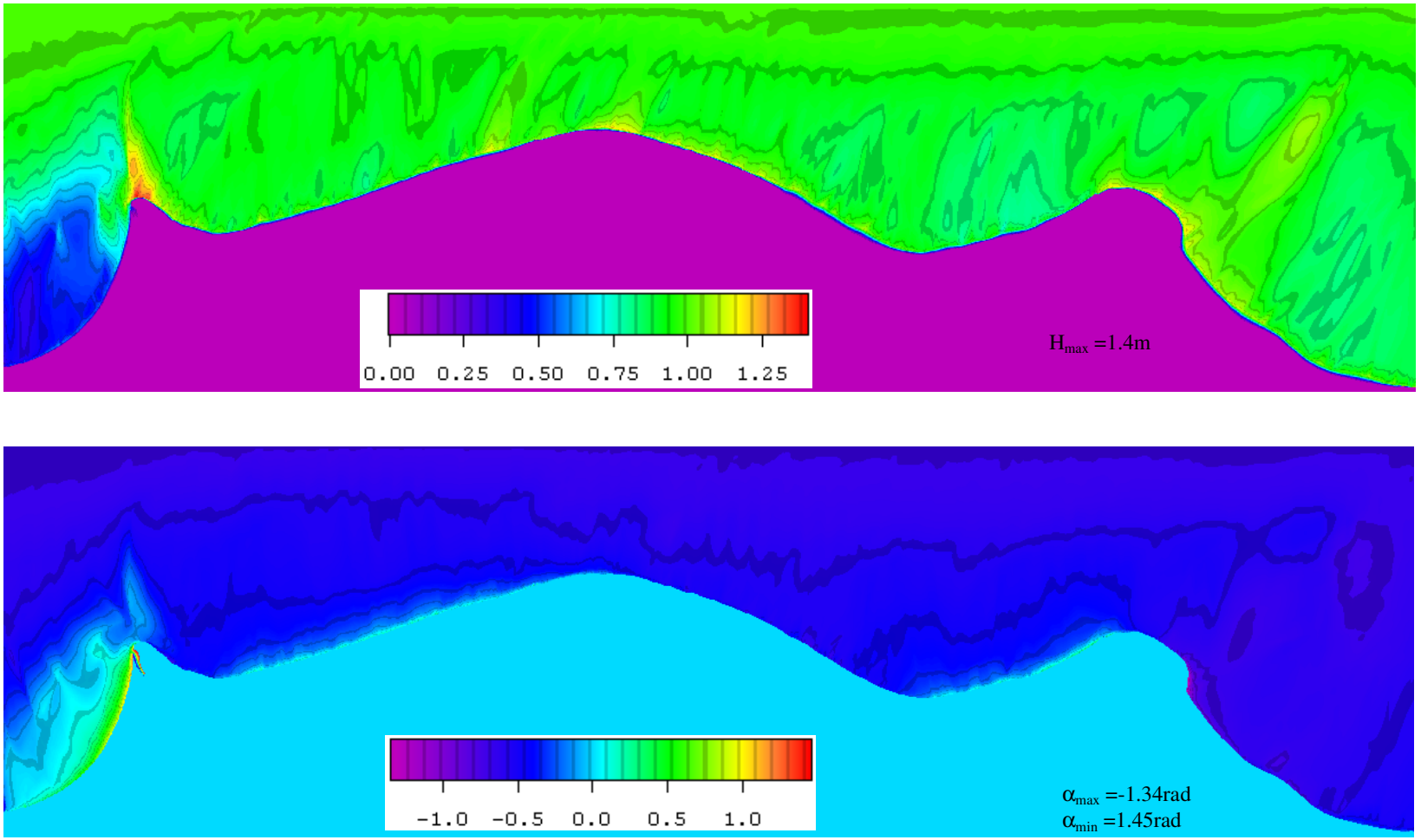

Figure 5.7. Wave height and wave direction in the study site, deep water wave height of 1 m propagating from the NE direction.

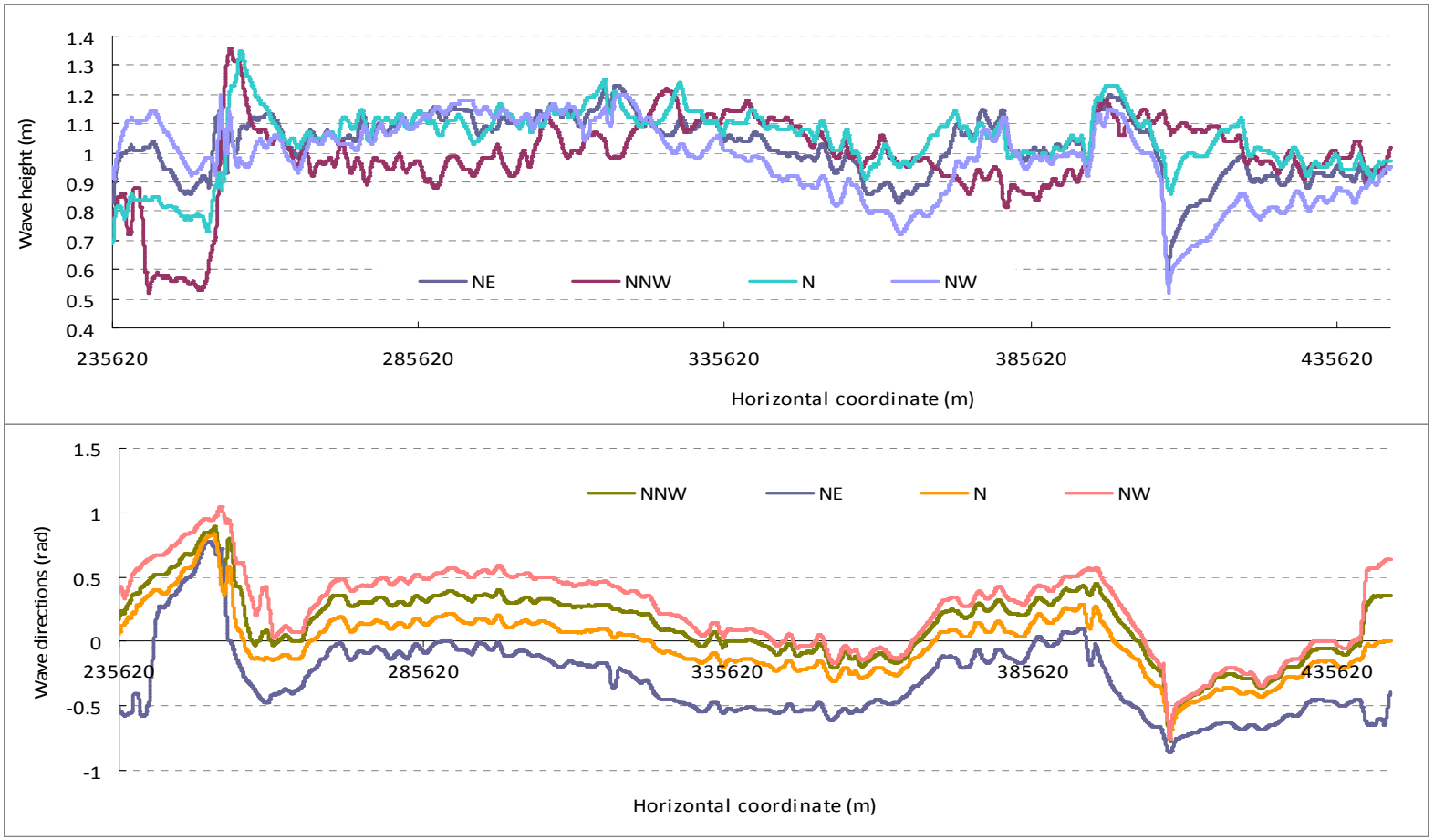

Figure 5.8. Breaking wave height and wave direction along the NDC.

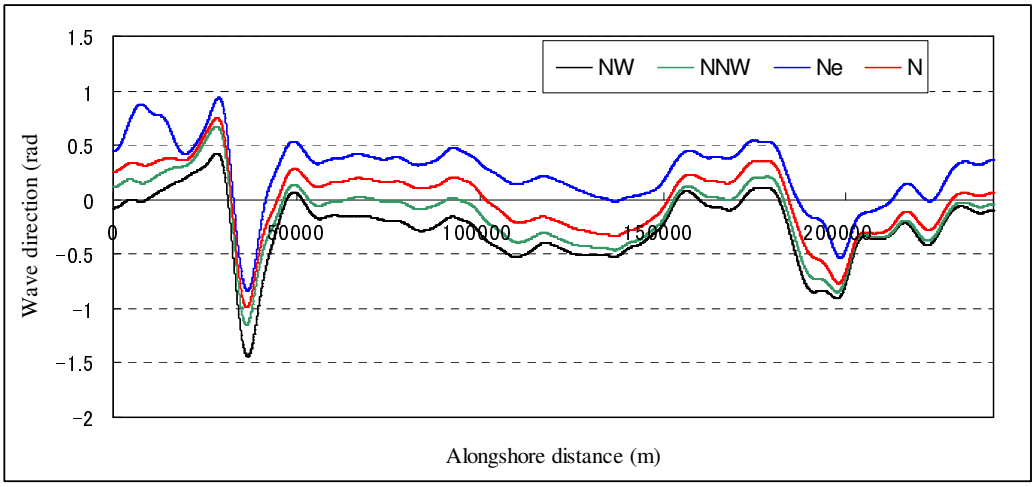

Figure 5.9. Alongshore breaking wave directions respected to the shoreline orientation.